A controlled quantum system
of individual neutral atoms

von

Stefan Kuhr

Bonn 2003

Mathematisch-Naturwissenschaftliche Fakultät
der
Rheinischen Friedrich-Wilhelms-Universität Bonn

Angefertigt mit Genehmigung der Mathematisch-Naturwissenschaftlichen Fakultät

der Rheinischen Friedrich-Wilhelms-Universität Bonn

Abstract

This thesis presents novel techniques to realize controllable quantum systems of neutral atoms. Besides the preparation of the exact number of atoms, we manipulate all physical degrees of freedom of the trapped particles.

The first part (Chapters 2, 3) reports on a deterministic source of single atoms, which overcomes the limitations imposed by statistical arrival in conventional sources. Single cold cesium atoms prepared in a magneto-optical trap are transferred into a standing wave optical dipole trap, made of two counter-propagating red-detuned Nd:YAG laser beams. Mutual detuning of the laser beam frequencies moves the standing wave pattern, allowing us to accelerate and stop an atom at preselected points along the standing wave. This "optical conveyor belt" can transport one atom over a maximum distance of 10 mm.

The second part (Chapters 4, 5) reports on the investigation of the coherence times of the Cs hyperfine ground states using microwave transitions. Using Ramsey spectroscopy techniques we measured coherence times of up to 100 ms. The limiting dephasing effects are experimentally identified and are of technical rather than fundamental nature. We present an analytical model of the reversible and irreversible dephasing mechanisms. Finally, we prove that controlled transport by the optical conveyor belt over macroscopic distances preserves the atomic coherence with slight reduction of coherence time.

————————————

Gegenstand dieser Arbeit ist die Realisierung von kontrollierten Quantensystemen aus einzelnen neutralen Atomen. Neben der exakten Kontrolle der Anzahl der Atome können wir alle physikalischen Freiheitsgrade der gespeicherten Atome gezielt manipulieren.

Der erste Teil (Kapitel 2, 3) berichtet über eine neuartige deterministische Quelle kalter Atome, die die Limitierung statistisch verteilter Ankunftszeiten bei konventionellen Atomquellen überwindet. Einzelne kalte Cäsiumatome werden von einer magneto-optischen Falle in eine optische Stehwellen-Dipolfalle, die von zwei entgegengerichteten Nd:YAG Laserstrahlen erzeugt wird, transferiert. Durch eine relative Verstimmung der beiden Laserfrequenzen kann die Stehwellenstruktur bewegt werden und auf diese Weise die Atome entlang der Strahlachse transportieren. Dieses "optische Förderband" ermöglicht den Transport eines einzelnen Atoms über eine Entfernung von 10 mm.

Im zweiten Teil (Kapitel 4, 5) werden die Kohärenzzeiten der Hyperfein-Grundzustände der gespeicherten Cäsiumatome untersucht. Mit Hilfe der Ramsey-Spektroskopie wurden Kohärenzzeiten von mehr als 100 ms gemessen. Die limitierenden Dephasierungseffekte konnten experimentell identifiziert werden und sind rein technischer Natur. Ein analytisches Modell beschreibt die reversiblen und irreversiblen Dephasierungseffekte. Schließlich wird gezeigt, dass ein Transport der Atome mit dem optischen Förderband die Kohärenzen erhält, wobei die Kohärenzzeit nur leicht reduziert wird.

Parts of this thesis have been published in the following papers:

1. S. Kuhr, W. Alt, D. Schrader, M. Müller, V. Gomer and D. Meschede, *Deterministic delivery of a single atom*, Science **293**, 278, (2001)

2. D. Schrader, S. Kuhr, W. Alt, M. Müller, V. Gomer and D. Meschede, *An optical conveyor belt for single neutral atoms*, Appl. Phys. B **73**, 819 (2001)

3. W. Alt, D. Schrader, S. Kuhr, M. Müller, V. Gomer and D. Meschede, *Properties of single atoms in an optical dipole trap*, Phys. Rev. A **67**, 033403 (2003)

4. S. Kuhr, W. Alt, D. Schrader, I. Dotsenko, Y. Miroshnychenko, W. Rosenfeld, V. Gomer, A. Rauschenbeutel and D. Meschede, *Coherence properties and quantum state transportation in an optical conveyor belt*, quant-ph/0304081 (2003)

Contents

Chapter 1

Introduction

The founders of quantum theory were convinced that manipulation of individual particles could only be accomplished in Gedanken experiments. Schrödinger claimed in 1952: *"We never experiment with just one electron or atom [...]. In thought experiments we sometimes assume that we do; this invariably entails ridiculous consequences"* [1]. Technological advances such as the invention of ion traps and laser cooling techniques, however, have allowed us to prepare and observe individual charged and neutral atoms. Nevertheless, at the beginning of this century, physicists are still striving for the full control of all physical degrees of freedom of single particles. The arising possibilities of tailoring quantum systems will provide new insights into fundamental physical phenomena at the quantum limit.

In this context, one of the most intriguing experiments is to study the interaction of single atoms with single photons. In the optical domain, this has recently been done in cavity-QED experiments in the groups of G. Rempe [2] and J. Kimble [3], involving individual atoms trapped inside a high-finesse optical cavity. Another approach uses microwave resonators, as realized in the experiment in the group of S. Haroche. There, circular Rydberg atoms from a velocity-selected atomic beam interact, one at a time, with a superconducting microwave cavity [4]. However, letting several atoms sequentially interact with the resonator field cannot be realized in the optical domain, since the lifetime of a cavity photon is typically only some tens of nanoseconds. It is extremely difficult to realize experiments where exactly two atoms are simultaneously coupled to the resonator mode. The present single-atom optical cavity-QED experiments work with atoms which randomly enter the resonator after being released from a magneto-optical trap. The disadvantage of this technique is that it relies on a Poissonian source of atoms, for which the probability of having exactly two atoms in the cavity is very small.

This thesis presents a novel deterministic source of cold atoms which should allow us to surmount these difficulties. A single cold cesium atom – or any desired small number of atoms – can be prepared in a magneto-optical trap. Using a moving standing-wave optical dipole trap, this atom can be transported at a time set by the experimentalist over millimeter-scale distances with sub-micrometer precision [5, 6]. Besides this control of the external degrees of freedom of a neutral atom, we are also capable of coherently

manipulating its internal degrees of freedom. More specifically, we couple the ground state hyperfine levels using microwave radiation. We found that the ground states exhibit long coherence times and that the coherence even persists when transporting the atom.

These results open the route to using neutral atoms for the storage and processing of quantum information. The idea of a quantum computer, which employs quantum systems to store and to process information, has created an entirely new field of research. Such a device operates in a way that it increases the probability of obtaining a desired result by constructive interference and diminishes the probability of obtaining an erroneous result by destructive interference. The most prominent examples of quantum algorithms are P. Shor's factoring algorithm [7], and L. Grover's database search [8].

Although it is unclear whether it can ever be realized, the idea of a quantum computer has strongly augmented the interest in studying quantum effects such as entanglement and decoherence. More importantly, it has brought together many different fields of research since several physical systems may meet the necessary requirements of scalability and sufficient coherence times [9]. Prominent candidates are NMR systems with molecules [10], spins in solid state systems [11], superconducting Josephson junctions [12] and polarization states of photons [13]. In the field of atomic physics, laser cooled trapped ions have successfully been entangled [14, 15] or are used to realize a CNOT quantum gate [16] in the group of D. Wineland. Most recently, the group of R. Blatt even implemented the Deutsch-Jozsa quantum algorithm [17].

Neutral atoms are more difficult to control than ions because of the weaker interaction of induced electric dipoles with electromagnetic fields. However, neutral particles might be advantageous because the weak coupling to the environment also leads to long coherence times of the internal and external states. The coupling between neutral atoms is more difficult to achieve than for ions, which interact via a common vibrational mode. To induce controlled interaction between neutral atoms different schemes were proposed: controlled cold collisions [18], induced dipole-dipole interaction [19], also with highly excited Rydberg atoms [20], magnetic spin-spin interaction [21] and the exchange of photons in a cavity [22, 23]. The controlled interaction of neutral atoms via photon exchange has already been demonstrated in the microwave regime by the creation of a phase gate [24] and by the entanglement of two atoms with the cavity mode [25]. In the optical regime, these fundamental realizations are still missing, to some extent because of the lack of control of the number of particles and their position. Our conveyor-belt should overcome these difficulties by placing a predetermined number of atoms into an optical cavity deterministically. This should pave the way to entangle neutral atoms via the exchange of photons or to realize a quantum gate.

Chapter 2

A source of single cold atoms

2.1 Introduction

The heart of our apparatus is an optical dipole trap which confines atoms in the antinodes of a far off-resonance standing wave. This type of trap relies on the dipole force, arising from inhomogeneous light fields. The first proposal of using this force to trap atoms was made by V. Letokhov already in 1968 [26], even before laser cooling was invented. Almost at the same time, A. Ashkin proposed the trapping and levitation of dielectric nanoparticles [27], which initiated the development of "optical tweezers" – a frequently used tool in biological investigations. Despite these ideas, the trapping of atoms by an off-resonance laser field could not be realized experimentally, because the trapping forces are too weak to confine atoms at room temperature. However, the first proposals to cool atomic gases with near resonant laser light in 1975 by T. Hänsch, A. Schawlow, D. Wineland and H. Dehmelt [28, 29] formed the basis for the three-dimensional cooling of atoms realized by S. Chu in 1985 [30]. These achievements permitted the first experimental observation of optically trapped atoms [31]. Shortly after, the cooling techniques were further refined by the realization of the magneto-optical trap (MOT) in 1987 [32], which became the most widely used instrument for the cooling of neutral atoms. Since then, among other applications, magneto-optical traps have served as a source of cold atoms, which can then be transferred into other traps.

In our experiments, we also use a MOT, however with a high magnetic field gradient, which allows us to trap single atoms or very small numbers of atoms [33, 34, 35]. This setup has been extensively used in our group for many years in order to study the properties of single atoms in a MOT, based on the observation of their fluorescence light [36, 37, 38, 39]. More recently, we demonstrated the transfer of a single atom from the MOT into an optical dipole trap [40, 41]. This previous experiment was realized with a dipole trap made of a single laser beam. Here, we have realized these experiments in an improved setup, using a standing wave dipole trap to achieve a better confinement of the trapped atoms compared to the travelling wave and a possibility of transportation (see Chapter 3).

2.2 Electromagnetic trapping

The two different types of atom traps employed in our experiment both use electromagnetic forces. To cool an atom down to temperatures of a few hundred µK, the MOT makes use of near-resonant light and provides dissipative forces. In contrast, atoms in the dipole trap are confined in a nearly conservative potential produced by far-off resonant light. I will only briefly introduce the magneto-optical trap, and refer to the literature for a more detailed description [42].

2.2.1 Magneto-optical trap

The MOT relies on velocity- and position-dependent momentum transfer due to the absorption of laser light. The radiation pressure forces are organized in such a way that the atoms are cooled and confined in one position. Laser cooling of free atoms is based on the Doppler effect, and its principle can best be visualized in a one dimensional picture. Consider a free atom moving in a field made of two counterpropagating laser beams whose frequencies are slightly red detuned from the atomic resonance. The beam which is counter-propagating to the motion of the atom is Doppler-shifted closer to resonance than the co-propagating beam and thus exerts a stronger radiation pressure. Therefore, the radiation pressure force is always opposed to the direction of motion. For small velocities, the force is proportional to the velocity and therefore represents a friction force. It causes a viscous damping of the atomic motion, therefore this configuration is named *optical molasses*. Cooling in three dimensions is achieved by intersecting three orthogonal pairs of laser beams.

The atom is continuously excited by the near resonant laser fields and it emits the photons in random directions, which causes heating. The balance between molasses cooling and the heating due to the spontaneously emitted photons leads to an equilibrium temperature. It is called the "Doppler temperature" or the "Doppler Limit" [43]:

$$T_{\mathrm{D}} = \frac{\hbar\Gamma}{2k_B}. \tag{2.1}$$

Here, Γ is the natural linewidth of the excited state; for cesium, $\Gamma = 2\pi \times 5.22$ MHz and $T_{\mathrm{D}} = 125$ μK. It was found experimentally that atoms can even be cooled to temperatures lower than T_{D} [44]. The reason for this are sub-Doppler cooling mechanisms that will not be discussed here [45].

The localization of the atom for a longer time requires a restoring force. For this purpose a magnetic quadrupole field is overlapped with the optical molasses. The magnetic field is zero at the trap center and increases linearly in the radial direction. The field gradient lifts the degeneracy of the Zeeman sublevels, as shown in Figure 2.1(a) for the case of a $J = 0 \rightarrow J' = 1$ transition. Additionally, the counter-propagating beams are set to opposite circular polarizations. This is done in such a way that, if the atom moves away from the trap center it is Zeeman-shifted into resonance with the laser beam opposed to
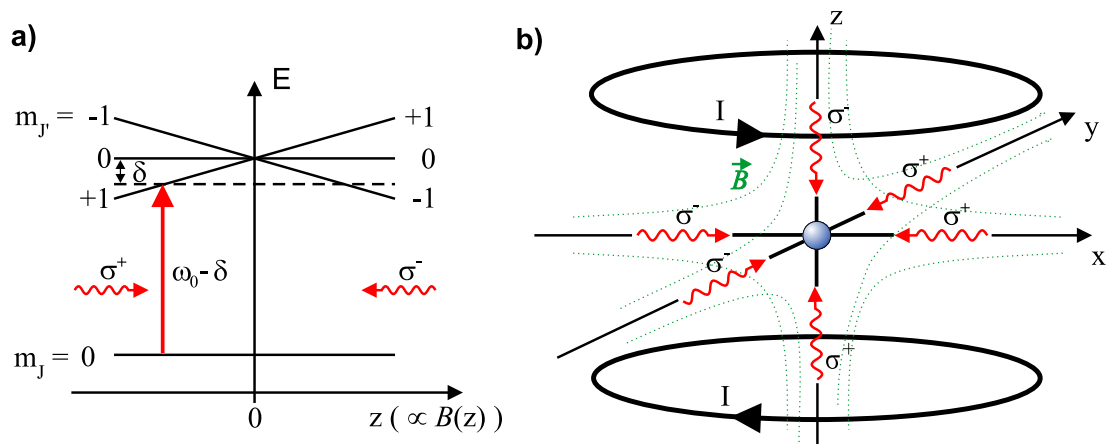
Figure 2.1: Magneto-optical trap (MOT). (a) Principle for the case of a $J = 0 \rightarrow J' = 1$ transition in the one-dimensional picture. The degeneracy of the excited state is lifted due to the Zeeman effect in the linear magnetic field gradient. When the atom moves away from the trap center it becomes resonant with the laser which pushes it back to the center. (b) For three-dimensional confinement, two coils in anti-Helmholtz configuration produce a quadrupole field.

the motion. Thus, it experiences a restoring force to the trap center. This principle can easily be generalized to the three-dimensional case (see Figure 2.1(b)). The cooling- and the restoring force cause the atoms to move in the MOT similarly to a damped harmonic oscillator.

2.2.2 Optical dipole trap

Optical dipole traps are based on an effect quite different from the radiation pressure which cools atoms in a MOT. While the radiation pressure acts in the direction of laser propagation, the dipole force acts in the direction of the gradient of the laser intensity. Another difference is that the dipole force is conservative and thus cannot be used for cooling.

Classical picture

The basic properties of a dipole trap can be inferred from the classical picture, in which the atom is considered as a charged harmonic oscillator driven by a classical radiation field. This model allows us to derive expressions for the dipole potential and the scattering rate [46].

A time-dependent electromagnetic field, $\boldsymbol{E}(t)$, oscillating at frequency ω,

$$\boldsymbol{E}(t) = \boldsymbol{E}\cos(\omega t) = \frac{\boldsymbol{E}}{2}\left(e^{i\omega t} + e^{-i\omega t}\right) \tag{2.2}$$

induces a dipole moment, $\boldsymbol{p}(t)$, in the atom which oscillates at the same frequency. The oscillation of the dipole moment is approximated by a damped harmonic oscillator, driven by an electric field. Since the dipole moment oscillates parallel to the direction of the polarization of the field, we can use a scalar approximation, $E(t) = |\boldsymbol{E}(t)|$, $p(t) = |\boldsymbol{p}(t)|$.

$$\frac{d^2 p(t)}{dt^2} + \Gamma \frac{dp(t)}{dt} + \omega_0^2 p(t) = \frac{e}{m_{\mathrm{e}}} E_0 \cos(\omega t). \tag{2.3}$$

Here, m_{e} and e are the mass and charge of the electron, ω_0 is the atomic resonance frequency and Γ is the damping rate, describing the energy loss of the radiating electric dipole. Γ can be calculated using Larmor's formula [47] as

$$\Gamma = \frac{e^2 \omega^2}{6\pi \epsilon_0 m_{\mathrm{e}} c^3} \tag{2.4}$$

Integration of Equation (2.3) in a complex representation yields the solution of an oscillating induced dipole

$$p(t) = p_0 \cos(\omega t). \tag{2.5}$$

The induced dipole moment p_0 is proportional to the E-field with the complex polarizability $\alpha(\omega)$ as the proportionality constant:

$$p_0 = \alpha(\omega) E_0, \tag{2.6}$$

which is given by

$$\alpha(\omega) = \frac{e^2}{m_{\mathrm{e}}} \frac{1}{\omega_0^2 + \omega^2 - i\omega\Gamma}. \tag{2.7}$$

The interaction energy, W, of the induced dipole moment in the driving field is

$$W = -\boldsymbol{p} \cdot \boldsymbol{E} \tag{2.8}$$

The electromagnetic field oscillates at optical frequencies, which are too fast for the atomic motion to follow. As a consequence, the motion of the atom is only influenced by a time average of W, which cancels the rapidly oscillating terms:

$$U_{\mathrm{dip}}(\boldsymbol{r}) = \langle W \rangle_{\mathrm{T}} = -\frac{1}{2\epsilon_0 c} Re(\alpha) I(\boldsymbol{r}). \tag{2.9}$$

Here, $\langle ... \rangle_{\mathrm{T}}$ denotes the time average over one oscillation period. Thus, the potential energy of the atom in the field is proportional to the intensity $I = c\varepsilon_0 |E|^2 / 2$. The expression of the dipole force is given by the gradient of the interaction potential

$$\mathbf{F}_{\mathrm{dip}}(\boldsymbol{r}) = -\nabla U_{\mathrm{dip}}(\boldsymbol{r}) = \frac{1}{2\epsilon_0 c} Re(\alpha) \nabla I(\mathbf{r}). \tag{2.10}$$

The interaction energy and the dipole force are proportional to the real part of the polarizability, which is *dispersive*, see Figure 2.2. The fact that $Re(\alpha)$ changes sign when crossing the resonance visualizes the two regimes of the dipole force. If the frequency
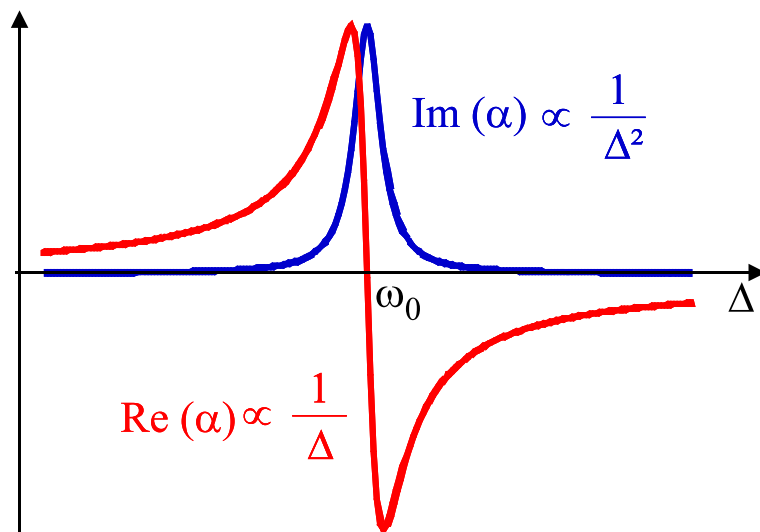
Figure 2.2: Real and imaginary part of the atomic polarizability α. The dipole force is proportional to $\mathrm{Re}(\alpha)$, which has a dispersive shape and thus changes sign when crossing the resonance. The scattering rate is proportional to $\mathrm{Im}(\alpha)$, showing a Lorentzian lineshape.

of the external field is smaller than the atomic resonance frequency ($\Delta = \omega - \omega_0 < 0$), the induced dipole oscillates in phase with the driving field and the atom is pulled into regions of high light intensities. If instead the driving frequency is tuned above the atomic resonance ($\Delta > 0$), the dipole moment is in phase opposition to the electric field. As a consequence, atoms are repelled from regions of highest intensity.

The driven oscillator also absorbs power from the driving field and emits it as dipole radiation. The absorbed power, $P_{\mathrm{abs}}(\mathbf{r})$, is given by

$$P_{\mathrm{abs}}(\mathbf{r}) = \langle \dot{\mathbf{p}} \cdot \mathbf{E} \rangle_{\mathrm{T}} = \frac{\omega}{\epsilon_0 c} \mathrm{Im}(\alpha) I(\mathbf{r}). \tag{2.11}$$

The emission can be regarded as a stream of photons with energy $\hbar\omega$, which leads to the scattering rate

$$\Gamma_{\mathrm{sc}}(\mathbf{r}) = \frac{P_{\mathrm{abs}}(\mathbf{r})}{\hbar\omega} = \frac{1}{\hbar\epsilon_0 c} \mathrm{Im}(\alpha) I(\mathbf{r}). \tag{2.12}$$

Thus, the classical picture already yields the correct dependences of the force and the scattering rate on the detuning, $F_{\mathrm{dip}} \propto 1/\Delta$ and $\Gamma_{\mathrm{sc}} \propto 1/\Delta^2$ (see Figure 2.2).

Semiclassical picture

In a semiclassical picture, the atom is considered as a two-level quantum system interacting with a classical radiation field. When saturation effects can be neglected, we obtain exactly the same result as the classical calculation. In the semiclassical picture the damping rate Γ

can no longer be calculated from Larmor's formula. Instead it represents the spontaneous emission rate from the excited level, and is thus determined by the dipole matrix element [46]:

$$\Gamma = \frac{\omega_0^3}{3\pi\epsilon_0\hbar c^3}\left|\langle e\,|\,\hat{d}\,|\,g\rangle\right|^2,\tag{2.13}$$

where $\hat{d}$ is the dipole operator and $|\,g\,\rangle$ and $|\,e\,\rangle$ are ground and excited state of the two-level atom. For the D lines of the alkali atoms the classical result (2.4) approximates the true decay rate (2.13) with an error of a few percent.

Simple expressions for the dipole potential and the scattering rate can be derived from Equations (2.9) and (2.12):

$$U_{\text{dip}} = \frac{\hbar\Gamma}{8}\frac{\Gamma}{\Delta'}\frac{I(\mathbf{r})}{I_0},\tag{2.14}$$

$$\Gamma_{\text{sc}} = \frac{\Gamma}{8}\left(\frac{\Gamma}{\Delta'}\right)^2\frac{I(\mathbf{r})}{I_0}.\tag{2.15}$$

Here the saturation intensity I_0 is defined as

$$I_0 = \frac{\omega_0^6}{36\pi^2\epsilon_0 c^5}\left|\langle e\,|\,\hat{d}\,|\,g\rangle\right|^2\tag{2.16}$$

and

$$\frac{1}{\Delta'} = \frac{1}{\omega-\omega_0} + \frac{1}{\omega+\omega_0}.\tag{2.17}$$

In the case of small detuning $\Delta \ll \omega_0$, we can apply the rotating wave approximation and neglect the second term on the r.h.s. of Equation (2.17) so that Δ' is replaced by the detuning Δ.

Quantum mechanical picture

In the quantum mechanical picture, the dipole potential is caused by the "ac Stark shift" ("light shift"), which can be calculated by second order perturbation theory. We apply a "dressed state" view [48] considering the combined system of atom plus quantized field. As shown in Figure 2.3, the two relevant states in the dressed state picture, $|\,g,n\,\rangle$ and $|\,e,n-1\,\rangle$ include the atomic energy levels and the number of photons, n, in the laser field. The unperturbed states are separated by the detuning, $\hbar\Delta$. When the coupling

$$\frac{\hbar\Omega}{2} = \langle e,n-1|\hat{\boldsymbol{d}}\cdot\hat{\boldsymbol{E}}|g,n\rangle\tag{2.18}$$

is switched on, these states are split by $\hbar\Omega_{\text{g}}$, where $\Omega_{\text{g}}^2 = \Omega^2 + \Delta^2$ denotes the generalized Rabi frequency. The shift of the ground-state corresponds to the dipole potential, which, for the case of large detuning ($\Delta \gg \Omega$), reads

$$U_0 = \frac{\hbar\Omega^2}{4\Delta}.\tag{2.19}$$
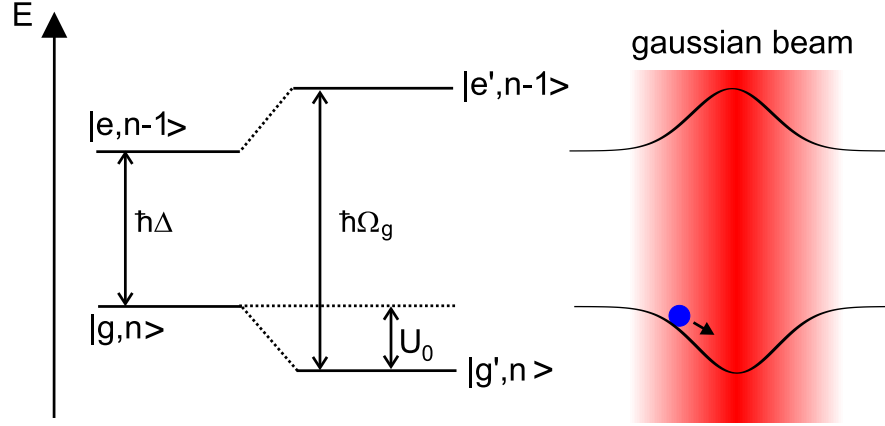
Figure 2.3: Schematic view of the light shift of a two-level atom in the dressed state picture. Right: The shift is proportional to the local laser intensity. For the case of red detuning the atom is pulled into the focus of the laser beam.

The excited state shows the opposite shift. In the case of low saturation, the atom remains in the ground state most of the time. This light-shifted ground state is therefore the relevant potential for the motion of the atom, as illustrated in Figure 2.3.

Semiclassical treatment for multi-level atoms

The complete semiclassical treatment for a multi-level atom includes the contributions of all coupled excited states. Let the time-dependent electric field of Equation (2.2) interact with an atom. Time-dependent perturbation theory yields an expression for the shift of the atomic levels, $\Delta E(E_i)$, characterized by their eigenenergies E_i [49]:

$$\Delta E(E_i) = -\frac{1}{4} \sum_{n',J',F',m'} \frac{1}{\hbar\Delta'_{\text{if}}} \left| \left\langle nJIFm | \hat{\boldsymbol{d}} \cdot \boldsymbol{E} | n'J'IF'm' \right\rangle \right|^2, \qquad (2.20)$$

where the sum covers all atomic states E_f except for the initial state E_i. The quantum numbers are n, J, F, m for the ground and n', J', F', m' for the excited states. For simplicity we have introduced the effective detuning Δ'_{if}:

$$\frac{1}{\hbar\Delta'_{\text{if}}} := \frac{1}{\hbar(\omega_{\text{if}} - \omega)} + \frac{1}{\hbar(\omega_{\text{if}} + \omega)}, \qquad (2.21)$$

where ω_{if} denotes the transition frequency $E_{\text{f}} - E_{\text{i}}$ and ω is the frequency of the electric field.

In order to calculate the energy shift of Equation (2.20), the Hamiltonian $\hat{\boldsymbol{d}} \cdot \boldsymbol{E}$ has to be expanded into spherical tensors [50]. Then, the standard procedure is to eliminate the m-dependence using the Wigner-Eckard theorem [49], which yields

$$\Delta E = -\frac{1}{4} \sum_{n',J',F',m'} \frac{1}{\hbar\Delta'_{if}} |E|^2 \begin{pmatrix} F & 1 & F' \\ -m & -\mu & m' \end{pmatrix} |\langle nJIF ||d|| n'J'IF' \rangle|^2. \qquad (2.22)$$

Here, the brackets denote the 3-J-symbols, μ is the polarization of the laser field, $\pm 1 \leftrightarrow \sigma^\pm, 0 \leftrightarrow \pi$ and $\langle nJIF||d||n'J'IF'\rangle$ is the reduced matrix element. By formally introducing 6-J-Symbols, the hyperfine coupling can be extracted from the atomic wavefunctions [51]:

$$\langle nJIF||d||n'J'IF'\rangle = (2F+1)(2F'+1)(-1)^{J+I+F'+1} \left\{ \begin{array}{ccc} J & F & I \\ F' & J' & 1 \end{array} \right\} \langle nJ||d||n'J'\rangle . \tag{2.23}$$

The remaining reduced matrix element $\langle nJ||d||n'J'\rangle$ is expressed using the oscillator strength f_{if} for the transition $nJ \to n'J'$:

$$f_{\text{if}} = \frac{2m_{\text{e}}}{3\hbar e^2} \frac{\omega_{\text{if}}}{2J+1} |\langle nJ||d||n'J'\rangle|^2 . \tag{2.24}$$

Using Equations (2.24) and (2.23) we obtain from Equation (2.22) an expression which only depends on the transition frequencies and the corresponding oscillator strengths:

$$\begin{aligned} \Delta E(n, J, F, m, \mu) \;=\; & -\frac{3e^2 I}{8\pi c^2 m\epsilon_0}(2J+1)(2F+1) \tag{2.25} \\ & \sum_{n',J',F',m'} (2F'+1)\frac{2\pi c}{\omega_{\text{if}}}\frac{f_{\text{if}}}{\Delta'_{\text{if}}} \left(\begin{array}{ccc} F & 1 & F' \\ -m & -\mu & m' \end{array} \right)^2 \left\{ \begin{array}{ccc} J & F & I \\ F' & J' & 1 \end{array} \right\}^2 \end{aligned}$$

.

Light shift of the D-Line of alkalis

Equation (2.25) is a general expression for calculating the light shift of an arbitrary atomic level with quantum numbers n, J, F, m in a light field with pure polarization μ. The oscillator strengths, f_{if}, and the transition frequencies, ω_{if}, are tabulated for many elements.

For the case of cesium in a far red detuned trap, the dominant contribution to the light shift originates from the D-lines, $J = 1/2 \to J' = 1/2, J' = 3/2$ (see Figure 2.4). The $F = 3$ and $F = 4$ hyperfine levels are nearly equally shifted, and the same holds for the m_F-sublevels for π-polarized light. We carry out the summation over all excited states F' and we obtain for the light shift of the ground states

$$\Delta E_\pi(\boldsymbol{r}) = -\frac{1}{3}\frac{\pi c^2 \Gamma}{2\omega_0^3} \left(\frac{2}{\Delta_{3/2}} + \frac{1}{\Delta_{1/2}} \right) I(\boldsymbol{r}). \tag{2.26}$$

Here, $\Delta_{\text{J}'} = \omega_{\text{L}} - \omega_{\text{J}'}$ is the detuning of the dipole trap laser from the $^6P_{\text{J}'}$-state. The same result could also be obtained by directly using perturbation theory in the fine structure basis [52].

For circularly polarized light, however, the degeneracy of the m_F-ground states is lifted

$$\Delta E_{\sigma^\pm}(\boldsymbol{r}) = -\frac{1}{3}\frac{\pi c^2 \Gamma}{2\omega_0^3} \left[\frac{2 \pm g_F m_F}{\Delta_{3/2}} + \frac{1 \mp g_F m_F}{\Delta_{1/2}} \right] I(\boldsymbol{r}), \tag{2.27}$$
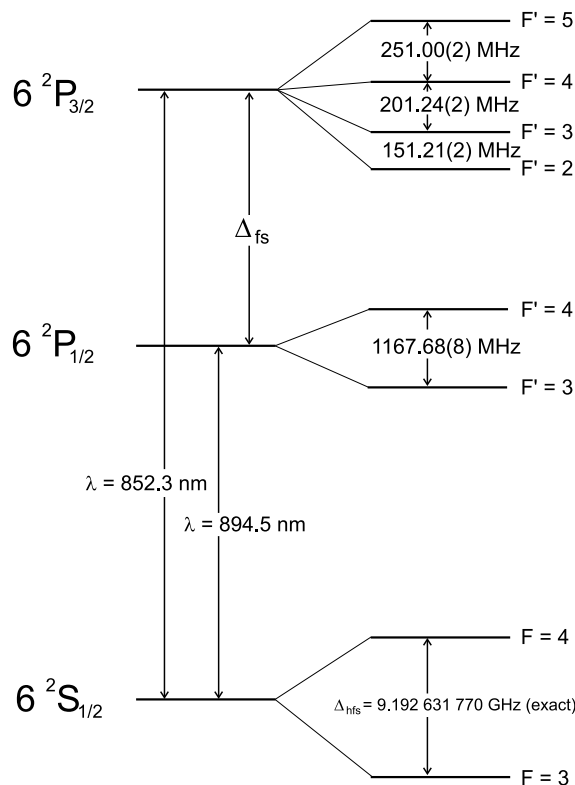
Figure 2.4: Level scheme of the D-line of ^{133}Cs.

with the Landé factors $g_3 = -1/4$ and $g_4 = 1/4$. The additional linear shift of the m_F-levels (vector light shift) is similar to the linear Zeeman effect in a weak magnetic field. In this sense, the σ-polarized light acts like a *fictitious magnetic field*. For a perfectly circularly polarized trap, the vector light shift in $|F = 4, m_F = 4\rangle$ amounts to 10% of the scalar light shift ΔE_π.

A full calculation of the light shifts according to Equation (2.25) would take into account all higher levels with their corresponding oscillator strengths [53]. Due to the coupling of the excited $6P_{J'}$-states to even higher states, their energy shifts may have the same sign as the ground state energy shift. Thus, the dipole forces can be attractive even for an atom in an excited state, in contrast to the simplified two-level picture of Figure 2.3. It is worth mentioning that there exists a "magic" wavelength for the dipole trap laser, for which the excited states and the ground state are equally shifted. For the case of the $6P_{3/2}$ and $6S_{1/2}$ manifolds of cesium, this wavelength amounts to $\lambda = 935$ nm, enabling state-insensitive optical trapping [54].

2.2.3 Standing wave dipole trap

In our experiments we use a standing wave optical dipole trap, consisting of two counter-propagating Gaussian laser beams with parallel linear polarization. The resulting inter-

ference pattern produces a series of potential wells, in which the atoms can be trapped. Neglecting wavefront curvature and Gouy phase shift, the spatial intensity distribution $I(\boldsymbol{r}) \equiv I(z, \rho)$ in a standing wave reads

$$I(z, \rho) = I_{\max} \frac{w_0^2}{w^2(z)} e^{-\frac{2\rho^2}{w^2(z)}} \cos^2(kz), \qquad (2.28)$$

where

$$w^2(z) = w_0^2 \left(1 + \frac{z^2}{z_{\mathrm{R}}^2}\right) \qquad (2.29)$$

is the beam radius with waist w_0, and the Rayleigh length

$$z_{\mathrm{R}} = \frac{\pi w_0^2}{\lambda}. \qquad (2.30)$$

The peak intensity, $I_{\max}$, in a Gaussian standing wave can be expressed using the total power of the two beams, P, and the waist w_0,

$$I_{\max} = \frac{4P}{\pi w_0^2}. \qquad (2.31)$$

This results in the following expression for the potential of a standing wave:

$$U(\rho, z) = U_0 \frac{w_0^2}{w^2(z)} e^{-\frac{2\rho^2}{w^2(z)}} \cos^2(kz), \qquad (2.32)$$

where the maximum trap depth, U_0, is defined as

$$U_0 = \frac{\hbar\Gamma}{2} \frac{I_{\max}}{I_0} \frac{\Gamma}{\Delta_{\mathrm{eff}}}. \qquad (2.33)$$

For the maximum scattering rate we obtain

$$\Gamma_{\mathrm{sc}} = \frac{U_0}{\hbar} \frac{\Gamma}{\Delta_{\mathrm{eff}}}. \qquad (2.34)$$

In Equations (2.33) and (2.34), we have introduced the effective laser detuning, Δ_{eff}, taking into account the contributions of the D_1- and D_2-lines [46]:

$$\frac{1}{\Delta_{\mathrm{eff}}} = \frac{1}{3} \left(\frac{2}{\Delta_{3/2}} + \frac{1}{\Delta_{1/2}}\right). \qquad (2.35)$$

For cesium atoms ($\lambda_{\mathrm{D1}} = 894$ nm, $\lambda_{\mathrm{D2}} = 852$ nm) in a dipole trap created with a Nd:YAG laser ($\lambda_{\mathrm{Nd:YAG}} = 1064$ nm) the effective detuning is $\Delta_{\mathrm{eff}} = 1.2 \times 10^7 \Gamma$. Typical potential depths are $U_0 = 1$ mK, yielding a corresponding scattering rate of $\Gamma_{\mathrm{sc}} = 11$ s^{-1}.

Oscillation frequencies

Trapped atoms oscillate in the standing wave potential, which is harmonic in the first order approximation both in the radial and axial directions:

$$U(\eta) = \kappa\eta^2 + O(\eta^4), \tag{2.36}$$

where κ is the expansion coefficient, and η stands for ρ or z, respectively. A Taylor expansion of Equation (2.32) yields the coefficients

$$\kappa_z = k^2 U_0, \tag{2.37}$$

$$\kappa_{\mathrm{rad}} = \frac{2U_0}{w_0^2}. \tag{2.38}$$

From the comparison with the harmonic oscillator,

$$\kappa = \frac{1}{2}m\Omega^2 \quad \Rightarrow \quad \Omega = \sqrt{\frac{2\kappa}{m}}, \tag{2.39}$$

one obtains the expressions for the axial and radial oscillation frequencies, Ω_z and Ω_{rad}:

$$\Omega_z = \sqrt{\frac{2k^2 U_0}{m}} \tag{2.40a}$$

$$\Omega_{\mathrm{rad}} = \sqrt{\frac{4U_0}{mw_0^2}}. \tag{2.40b}$$

For a trap of $U_0 = 1.0$ mK, the oscillation frequencies are $\Omega_z/2\pi = 235$ kHz and $\Omega_{\mathrm{rad}}/2\pi = 2.7$ kHz assuming a waist of $w_0 = 30$ µm.

2.3 Experimental setup

Compared to the previous experiments realized with a single beam dipole trap inside a steel chamber [40, 41], we have realized an improved setup permitting more flexibility in the observation and manipulation of the atoms [55]. We now use a standing wave dipole trap, which is shined in perpendicular to the imaging optics, in order to reduce stray light. The use of a glass cell provides better optical access for laser beams and detectors. Moreover, we replaced the permanent magnetic disks by magnetic coils to enable us to switch off the magnetic field. Additionally, we developed new imaging optics [56] which improved the fluorescence yield by more than a factor of two. Finally, a sophisticated computer control system allows us to create arbitrary pulse sequences for the realization of complex experiments.
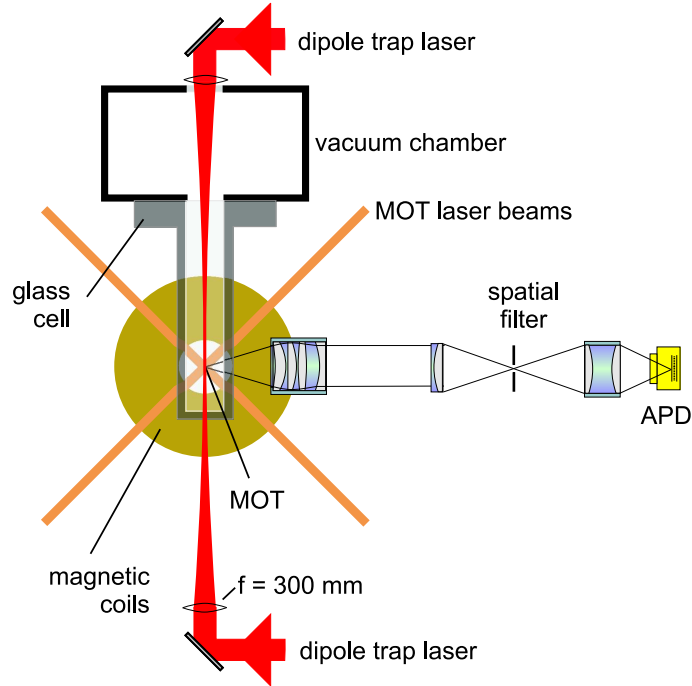
Figure 2.5: Experimental setup. MOT and dipole trap are overlapped in the center of a vacuum cell. Fluorescence light is collected by imaging optics with spatial filtering apertures and is detected with an avalanche photodiode (APD).

2.3.1 Vacuum system

Any experiment with cold atoms must be performed in an ultra high vacuum environment to guarantee long storage times. At the same time it is desirable to have free access to the experimental region for laser beams and detection optics. A glass cells fulfills these requirements better than a steel chamber with vacuum windows, and its compact size avoids the placement of any (optical) element inside the vacuum chamber. Our cell consists of glass of 5 mm thickness with outer dimensions of $30 \times 30 \times 120$ mm^3 (Hellma), see Figure 2.5. The outer surfaces are anti-reflection coated, whereas for technical reasons the inner surfaces remain uncoated. Its end consists of a glass cylinder attached to a CF63 flange with a special sealing (Helicoflex). The flange is connected to a steel cube to which the pumps and the cesium reservoir are attached. Our cesium reservoir is separated from the main chamber by a valve. This valve remains closed most of the time and is opened only for several minutes when a high number of atoms is desired. The use of a titanium sublimation pump (Varian, 916-0017) together with an ion pump (Varian, StarCell VacIon Plus, 120 l/s) yields a background gas pressure of better than 10^{-10} mbar.

2.3.2 Magnetic coils

The high field gradient of the MOT is produced by water cooled magnetic coils, placed at a distance of 2 cm away from the trap center. They can generate field gradients of

up to $\partial B/\partial z = 500$ G/cm at a maximum current of 20 A. In all experiments described in this thesis we operate the coils with a current of 15.4 A, yielding a gradient of $\partial B/\partial z = 300$ G/cm. A special electronic circuit allows us to switch the current to zero within 3 ms and to switch it back on within 30 ms. However, eddy currents in the conducting materials surrounding the vacuum chamber persist for about 25 ms.

2.3.3 Lasers

Diode lasers and stabilization

The application of light forces requires the lasers to be stabilized onto or near the atomic resonance frequency. Except for the dipole trap, only a moderate laser power is required, and therefore diode lasers are sufficient. The three diode lasers employed in this experiment are set up in a Littrow configuration with home-built current and temperature controllers. All lasers are locked by polarization spectroscopy [57, 58].

MOT cooling laser. The MOT cooling laser must be red-detuned by approximately one natural linewidth from the cycling transition $F = 4 \rightarrow F' = 5$. Since in this frequency range, no feature exists in the polarization spectrum that can be used as an error signal, we lock the laser to the crossover transition $F = 4 \rightarrow F' = 3/5$,
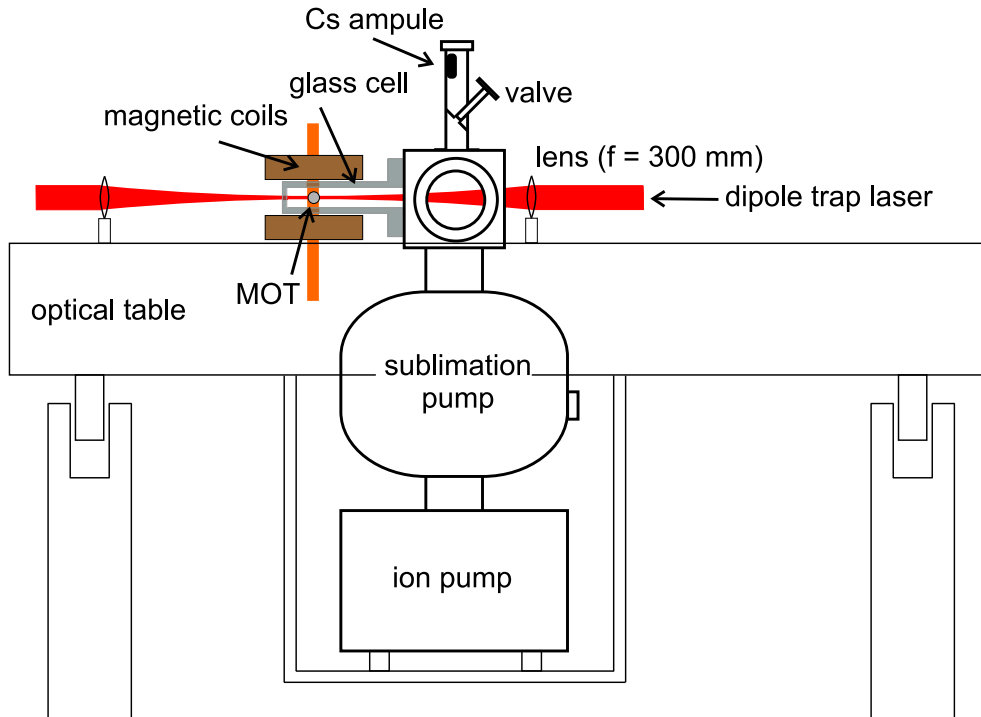
Figure 2.6: Schematic of the experimental apparatus.

which is red-detuned by -225 MHz from the cycling transition. An acousto-optical modulator (AOM) in double pass configuration shifts the laser frequency by 2×110 MHz towards the atomic resonance. The AOM is also useful to alter the MOT laser power during the experiment, e. g. to optimize the transfer of atoms from the MOT into the dipole trap.

Repumping laser. Although the $F = 4 \to F' = 4$ transition is detuned from the cooling transition by 50 Γ, there is a finite probability of excitation to the $F' = 4$ level, from where a spontaneous decay to the $F = 3$ ground state can occur. The large ground state hyperfine splitting of 9.2 GHz requires a separate repumping laser to transfer the atom back into the $F = 4$ level. For this purpose, this laser is locked to the $F = 3 \to F' = 4$ transition.

Probe laser. A third diode laser, the so-called probe laser, is locked to the $F = 4 \to F' = 5$ transition. It is used for the resonant illumination of the atoms within the dipole trap (see Section 3.3.1) as well as a laser which state selectively removes the atoms from the dipole trap (see Section 4.3.3).

The lasers, together with the stabilization setups, are installed on a separate optical table. Single mode polarization maintaining fibers are used to transfer the light to the main table. All lasers can independently be switched on and off by means of mechanical shutters (Vincent Assicociates, LT02). The switching time depends on the laser beam size and is less than 50 µs while the minimum opening time of the shutters is 1 ms.

Nd:YAG laser

Most experiments described in this work require cold atoms held in an environment which does not perturb the internal atomic states. Since the lifetimes of the internal states is of such great importance, it is desirable to avoid resonant excitation by using a very far detuned laser to form the dipole trap. Nd:YAG lasers are ideal tools for this purpose because they provide a high output power and operate at a wavelength of 1064 nm, which is more than $10^7 \, \Gamma$ detuned from the D_1 line of cesium at 894 nm.

We use a commercial laser (Quantronix/Excel Technologies, Model 112) consisting of a single Nd:YAG crystal inside a two-mirror resonator. The crystal is placed in one focus of an elliptic mirror and is pumped by a krypton arclamp located in the other focus. The maximum output power of the laser is 11 W. Inside the resonator, two pinholes suppress the modes other than the TEM_{00} and two brewster windows ensure a linear polarization of the beam. In addition, we placed a Fabry Perot etalon inside the resonator to narrow the spectral bandwidth by decreasing the number of lasing longitudinal modes. The number of longitudinal modes can easily be inferred by shining the laser onto a fast

photodiode connected to a spectrum analyzer. The signal we obtain shows that the laser operates on 4 - 5 longitudinal modes with a spacing of 220 MHz. This corresponds to a spectral bandwidth of $\Delta\nu \sim 1$ GHz yielding a coherence length of $c/\Delta\nu = 30$ cm, which is sufficient for our purposes.

A prerequisite for efficient transfer of atoms between MOT and dipole trap is a thorough alignment. The focus of the dipole trap laser must be perfectly overlapped with the center of the MOT. As a sensitive alignment criterion, we use the fact that the Nd:YAG laser shifts the atomic transition out of resonance, which lowers the fluorescence rate of the MOT. We thus superpose the dipole trap with the MOT by minimizing the fluorescence rate of the trapped atoms. This is done for both dipole trap laser beams separately.

2.3.4 Detection optics

The detection of extremely low levels of fluorescence light from a single trapped atom requires special detection optics. We use a home-built diffraction-limited objective [56], consisting of four lenses, with a working distance of 36 mm and a numerical aperture of NA = 0.29. The working distance is determined by our laser setup because laser beams reflected off the glass cell must not enter the objective. An $f = 80$ mm doublet lens focusses the collimated fluorescence light through a pinhole of 150 µm diameter for spatial filtering. The transmitted light is imaged onto an avalanche photodiode (APD, model SPCM-200 by EG&G) operated in single photon counting mode with a quantum efficiency of $\eta_{\mathrm{APD}} = 50\%$ at $\lambda = 852$ nm. We use interference filters (Dr. Anders) with a transmission of $\eta_{\mathrm{IF}} = 80\%$ at 852 nm and 10^{-6} at 1064 nm to attenuate the Nd:YAG laser stray light to 30 photons/s, comparable to the dark count rates of the APDs. Given the numerical aperture of NA = 0.29, the objective covers $\Omega/4\pi = 2\%$ of the total solid angle. Hence, the theoretical upper limit for the count rate of a strongly saturated two level atom is

$$R = \eta\frac{\Gamma}{2} = 17 \times 10^4 s^{-1}, \quad \text{with} \quad \eta = \eta_{\mathrm{APD}}\,\eta_{\mathrm{IF}}\,\frac{\Omega}{4\pi}, \tag{2.41}$$

where $\eta = 8 \times 10^{-3}$ using the above parameters. Experimentally, we obtain a maximum count rate of $8 \times 10^4\,s^{-1}$ per atom.

2.3.5 Data processing

The APD signal resulting from the detection of a photon is converted into a TTL pulse and sent to a custom built timer card (Silicon Solutions, TimerCard V3). Its logical functions are implemented on an FPGA (field programmable gate array) and it records the time intervals between subsequent photon counts with a resolution of 50 ns. The card is equipped with four independent input channels, which would permit the connection of up to four APDs. For each detection event, the time interval together with the channel number is queued as a 32 bit number into a FIFO buffer whose contents are transferred to a computer. Bus transfer rates limit the maximum counting rates to 1 MHz. The dead

time of the APDs (200 ns) and the resulting nonlinear response restrict the count rates to the same limit [59].

Finally, the timer card only registers photon counts if an external gate is set to "high" and stores the time at which it is switched on. The method of recording the arrival times of all fluorescence photons allows us to gather information of the atomic dynamics on different timescales. However, during an entire day one easily records several gigabytes of photon counts. The raw data is a huge file containing only time intervals between photon counts and time stamps of the gate signal. Extracting the relevant information is performed with another computer program. After the experiment has been performed, the program bins the photon counts in suitable time intervals (usually 1 ms), before it automatically counts atom numbers, detects fluorescence peaks, filters datasets, calculates survival probabilities, or even plots entire spectra.

Parallel to the timer card, the APD pulses are sent to a Multi-Channel-Scaler (EG&G Ortec, TurboMCS), which integrates the number of detected photons in time intervals of 100 ms. This signal serves as a real time monitor of the MOT and its dynamics (see Figure 2.7) and is continuously displayed on a computer screen. It is essential for the alignment of the dipole trap laser and numerous pump and probe laser beams onto the MOT.

2.3.6 Computer control system

The experiment requires rather complex sequences of laser- and microwave pulses, together with the altering of magnetic fields, detunings or intensities. This task is accomplished by a computer control system, whose development is a part of this thesis. A detailed description of its features is given in Appendix B. The hardware consists of three PC boards, one digital board (National Instruments, PCI-DIO32-HS) with 32 outputs for TTL signals and two D/A boards (National Instruments, PCI 6713) together providing 16 channels with analog output voltages in the range of -10 V to +10 V with a maximum time resolution of 2 µs. The software has a graphical user interface which permits the rapid design of complex sequences.

2.4   Single atoms in a MOT

2.4.1   Experimental techniques

While conventional MOTs collect large samples of $10^3 - 10^{12}$ atoms, we use a variant which permits trapping of single atoms with long storage times [33, 34, 35]. Neglecting collisions between stored atoms, the number of atoms in the MOT is given by the rate equation

$$\dot{N} = R_{\mathrm{L}} - \frac{N}{\tau}. \tag{2.42}$$

Here, R_{L} is the loading rate and τ is the storage time, limited by collisions with background gas atoms. Trapping a single atom requires the minimization of the average number of
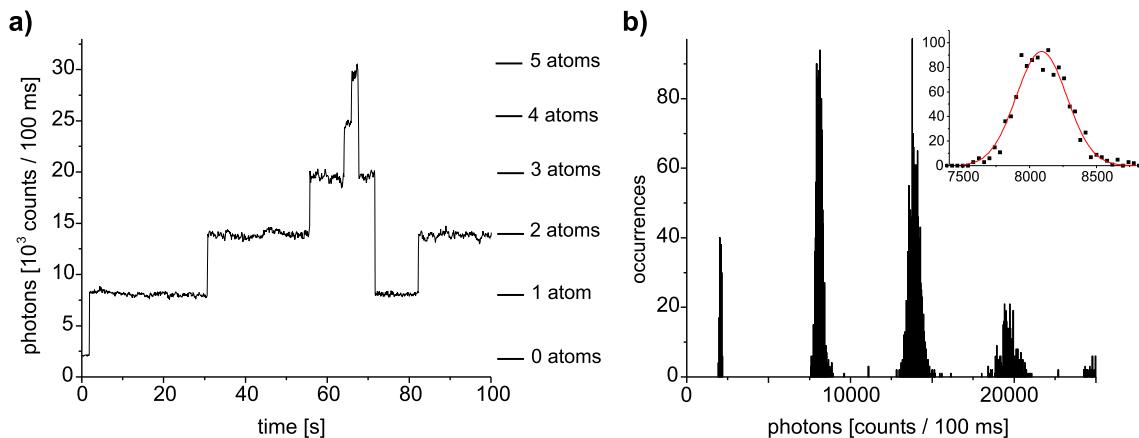
Figure 2.7: (a) Fluorescence signal of the MOT, integrated in time intervals of 100 ms. Each trapped atom increases the signal by the same amount, allowing us to determine their exact number. (b) Histogram of fluorescence counts.

atoms, $\overline{N} = R_{\mathrm{L}} \cdot \tau$, resulting from Equation (2.42). It is desirable to obtain a long storage time τ, which is governed by the background gas pressure. Several strategies exist to reduce R_{L}. In the first place, this can be achieved by reducing the cesium partial pressure in the vacuum chamber. Secondly, the capture cross section of the MOT, σ, and thus R_{L}, drastically decrease with increasing magnetic field gradient [60]:

$$\sigma \propto \left(\frac{\partial B}{\partial z} \right)^{-14/3} \tag{2.43}$$

In this experiment, gradients in the order of $\partial B / \partial z = 300$ G/cm reduce the capture cross section by more than 6 orders of magnitude compared to a standard MOT with e. g. 20 G/cm. Alternatively, the use of small laser beam diameters [33] or deliberate misalignment of the beams [61] can also result in a very small mean atom number. However, we found it to be advantageous to use a strong magnetic field gradient, because it enables a more reproducible alignment of the trap lasers. More importantly, the strong field reduces the diameter of the MOT to about 30 μm in our case, providing good localization of the trapped atom. This is, as we will see later, essential for a perfect spatial overlap with the dipole trap which guarantees a high transfer efficiency between the two traps.

2.4.2 Observation of single atoms in a MOT

The number of trapped atoms can be determined in real time from the fluorescence signal of the MOT (see Figure 2.7). The number of detected photons is integrated in time intervals of 100 ms and plotted as a function of time. The signal has a step-like shape, because each trapped atom contributes to the total fluorescence signal by the same amount. This allows us to infer the exact number of atoms as long as the statistical fluctuations of the signal are smaller than the fluorescence of one atom. The fluorescence rate detected from one atom amounts to 6×10^4 s^{-1} in this case. The background signal

of 2×10^4 s^{-1} results essentially from stray light of the MOT laser beams which are reflected at the glass cell.

Figure 2.7(a) shows an average time between two loading events in the order of 20 s. This loading rate strongly depends on the cesium background pressure and on the detuning and intensity of the MOT beams. By varying only the background pressure we can alter the spontaneous loading rate from $R_L = 1$ atom/10 min to $R_L = 1$ atom/100 ms. It is interesting to note that for the dataset shown, the atoms leave the trap in pairs as a result of cold collisions. This phenomenon was extensively studied in previous works [62, 38, 39] in our group.

The fluctuations of the photon count rate originates in the poissonian counting statistics and in the intensity fluctuations of the MOT lasers [63]. A histogram of the photon counts is shown in Figure 2.7(b). The inset shows the enlarged peak for 1 atom which is fitted with a Gaussian, yielding a mean $N_1 = (8090 \pm 7)$ photon counts per 100 ms and an rms width of $\sigma = (94 \pm 2)$ counts/100 ms. Since Poissonian statistics predicts an rms width of $\sqrt{N_1} = (89.94 \pm 0.04)$ counts/100 ms, we conclude that the statistical fluctuations clearly dominate and intensity fluctuations play a minor role here.

We can determine the minimum time interval which is needed to distinguish e.g. 1 atom from 2 atoms. As a criterion we demand that the difference of the count rates of one and two atoms, $\Delta N = 58000$ s^{-1}, is 4 times larger than the statistical fluctuations.

$$4\sigma = 4\sqrt{(N_1 + \Delta N)t} = \Delta N\, t \qquad \Rightarrow \qquad t = \frac{16(N_1 + \Delta N)}{\Delta N^2} \qquad (2.44)$$

which yields $t = 300$ µs.

2.4.3 Forced loading - "magnetic umbrella"

Many experiments, especially those presented in Chapter 3, require the loading of only one atom into the MOT, which is then transferred into the dipole trap. Additionally, to obtain good statistics, it is necessary to repeat the same experiment with identical parameters many hundreds of times. The simplest way to do this would be to wait until one atom is accidentally loaded from the background gas vapor and then start the experiment. One would thus spend a significant amount of time waiting for an atom to be loaded into the trap. Higher loading rates could be achieved by increasing the cesium vapor pressure, at the expense of an increased probability of loading events during the measurement procedure.

The "magnetic umbrella" represents a simple way to solve this dilemma. To speed up the loading process, we temporarily lower the magnetic field gradient to $\partial B/\partial z = 40$ G/cm during a time t_{low}. As discussed above, this results in a larger capture cross section which significantly increases the loading rate. Then, the field gradient is returned to its initial value, confining the trapped atoms at the center of the MOT. Varying the time during
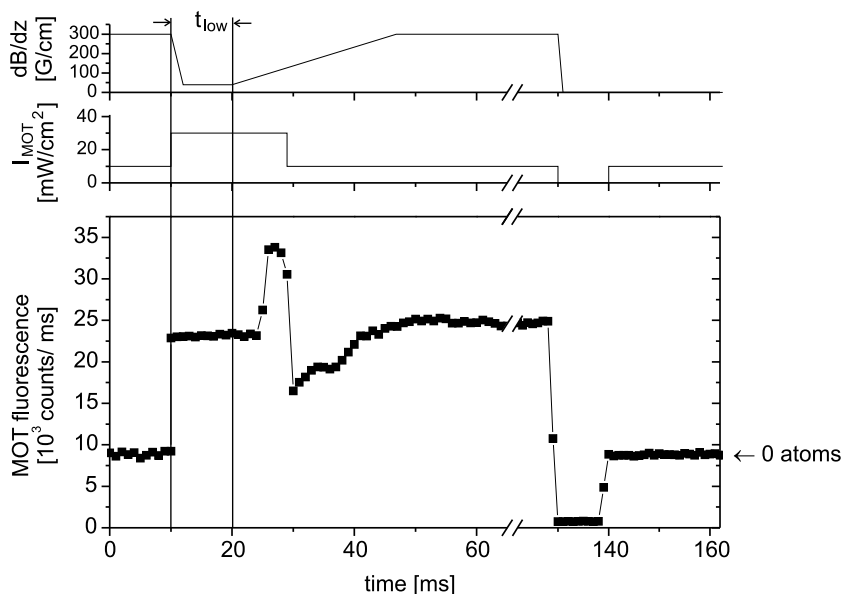
**Figure 2.8**: "Magnetic umbrella". During the loading time t_{low} the magnetic field gradient is reduced and the intensity of the MOT lasers is increased. The trapped atoms fully appear in the observation region at $t = 50$ ms, since the magnetic field needs 30 ms to increase to its full value. The graph shows the added fluorescence counts from 600 shots with a mean atom number $\overline{N} = 2$.

which the field gradient is low enables us to select a specific *mean* atom number. The time to load e.g. one atom is typically 10 ms. Note that this number strongly depends on the cesium background pressure and may thus vary by more than an order of magnitude. To further speed up the loading process, we increase the power of the MOT cooling laser by a factor of 3 while the field gradient is reduced.

The fluorescence signal of the MOT during the application of this loading technique is shown in Figure 2.8, averaged over 600 shots with $t_{low} = 7$ ms. Initially, no atoms are trapped and the detector only observes stray light from the MOT lasers. The increase of the MOT cooling laser intensity from $I_{MOT} = 10$ mW/cm^2 to $I_{MOT} = 30$ mW/cm^2 at $t = 10$ ms leads to the corresponding increase of the stray light. Simultaneously, the magnetic field is reduced to 40 G/cm within 3 ms. Note that no fluorescence from the low field gradient MOT is detected, since the position of the MOT is shifted out of the observation volume. When the field gradient is increased back to 300 G/cm with a technically limited rise time of 30 ms, the atoms appear in the observation volume.

Atom number statistics

Experimentally, it is possible to adjust the time of low field gradient to load one atom on average. The theoretical maximum efficiency of this process is dictated by Poissonian
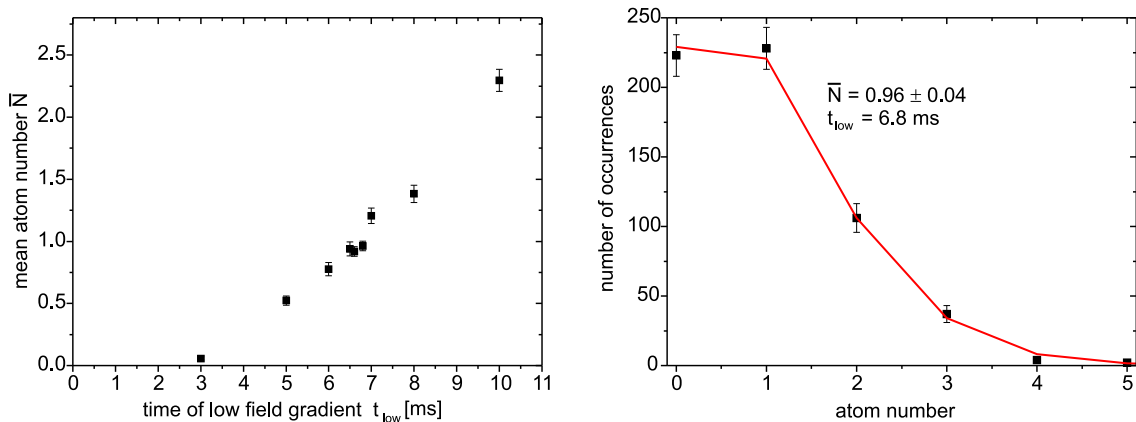
Figure 2.9: Statistics of the loaded atom number. (a) By increasing the time of low field gradient, t_{low}, we also increase the mean atom number $\overline{N}$. (b) Atom number statistics for $t_{\text{low}} = 6.8$ ms (600 shots), resulting in a mean atom number $\overline{N} = 0.96 \pm 0.04$ in this particular measurement. The line is the Poissonian distribution of Equation (2.45).

statistics, which describes the probability of loading n atoms with a mean atom number $\overline{N}$:

$$P_{\overline{N}}(n) = \frac{\overline{N}^n e^{-\overline{N}}}{n!}. \tag{2.45}$$

Since $P_{\overline{N}}(1)$ has its maximum for $\overline{N} = 1$, the highest probability of capturing one atom is $P_1(1) = e^{-1} = 36.79\%$.

Experimentally, one can easily approach this limit up to a few percent. The mean atom number $\overline{N}$ scales linearly with t_{low}, as shown in Figure 2.9.(a). The choice of e.g. $t_{\text{low}} = 6.8$ ms results in a mean atom number $\overline{N} = 0.96 \pm 0.04$ (see Figure 2.9(b)). The measured probability of obtaining one atom, $P_{0.96}^{\text{exp}}(1) = 38.0 \pm 2.5$ % is in perfect agreement with the Poissonian distribution, which predicts $P_{0.96}^{\text{th}}(1) = 36.76\%$.

2.5 Single atoms in an optical dipole trap

The next step is the transfer of the atoms from the MOT into the dipole trap. It is essential for the following experiments that this transfer be accomplished with high efficiency, especially for the case of a single atom. In view of the experiments in Chapter 4 and Chapter 5 we also briefly investigate the dependence of the transfer efficiency on the number of atoms.

2.5.1 Transfer of atoms between MOT and dipole trap

In order to transfer cold atoms from the MOT into the dipole trap, both traps are simultaneously operated for some tens of milliseconds before we switch off the MOT. After
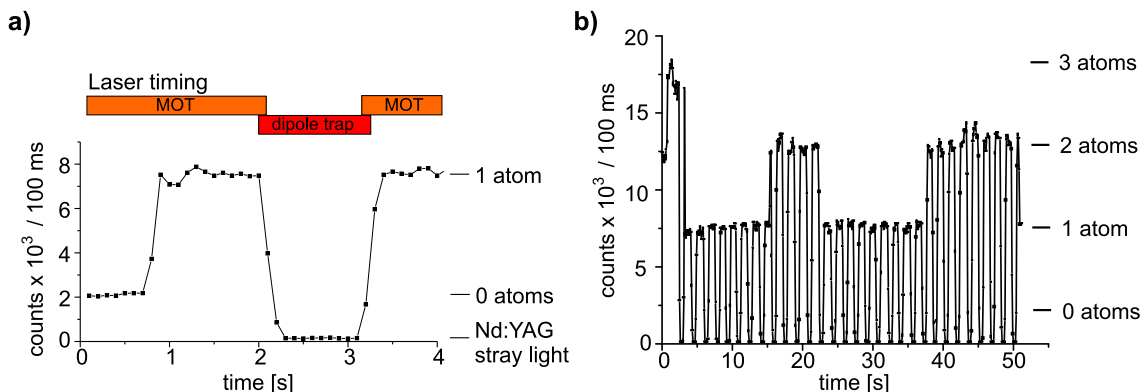
Figure 2.10: Transfer of atoms between MOT and dipole trap. (a) Storage of a single atom in the dipole trap for 1 s. The fluorescence signal (integration time = 100 ms) of the atom demonstrates the trapping in the dipole trap and recapturing by the MOT. (b) Atoms can be transferred many times between both traps without losses. The storage time is 500 ms in this case.

storage in the dipole trap the atoms are transferred back into the MOT by the reverse procedure. Figure 2.10(a) shows the corresponding fluorescence signal. A single atom is transferred from the MOT into the dipole trap ($U_0 = 1.4$ mK), in which it is kept for 1 s. The atom is then recaptured into the MOT showing the same fluorescence level as before. During the storage in the dipole trap the photon count rate decreases to typically 200 counts / 100 ms, dominated by stray light sources in the laboratory. Transfer of the same atom between the traps can be done repeatedly (see Figure 2.10(b)). For a storage time of 500 ms we obtain a transfer efficiency of $97.2 \pm 0.8\%$ (see Figure 2.11).

Trap lifetime

The efficient transfer of atoms between the two traps provides a simple procedure for measuring their lifetime in the dipole trap. In our case, we obtained a lifetime of $\tau = 25 \pm 3$ s (see Figure 2.11), which is limited by background gas collisions. This was inferred from an independent measurement, in which trapping atoms in the magnetic trap yields the same lifetime [40]. Heating mechanisms such as photon scattering, intensity fluctuations and beam pointing instabilities of the trapping laser beams are not observable in our experiment [64].

For the realization of the moving standing wave (see Chapter 3), both laser beams are sent through acousto-optical modulators to mutually detune them. In this case, we observed a reduced lifetime of the trapped atoms of about 3 s. This reduction is due to fluctuations of the relative phase $\Delta\phi$ between the two RF-outputs of the dual frequency synthesizer which are directly translated into position fluctuations of the dipole trap potential along the standing wave axis. The phase fluctuations amount to $\sqrt{\langle\Delta\phi^2\rangle} \approx 10^{-3}$ rad in the frequency band of $0 - 1$ MHz and cause heating of the trapped atoms. This effect has been studied in detail in [55, 64] and will not be discussed here further. However, the
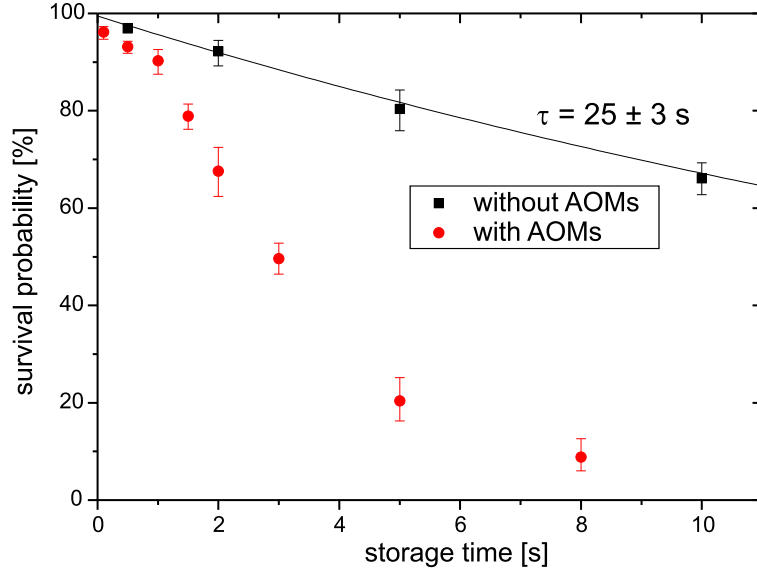
Figure 2.11: Storage time in the dipole trap with (circles) and without phase noise (squares) at otherwise identical conditions. In the latter case the decay is due to background gas collisions and purely exponential with a decay time of $\tau = 25 \pm 3$ s.

observed lifetime is still longer than all experimentally relevant time scales.

2.5.2 Binomial distribution and confidence limits

The initial and final number of atoms is inferred by observing their fluorescence in the MOT before and after any experiment in the dipole trap. Depending on the required precision, the experiment is repeated many times, yielding the total atom numbers, $N \equiv N_{\text{initial}}$ and $m \equiv N_{\text{final}}$. They are used for calculating the survival probabilities or trapping efficiencies, $p = m/N$.

The underlying statistics is the Binomial distribution, which describes processes with a given number of identical trials, with two possible outcomes, 'success' or 'failure'. The probability of m successes out of N trials, each of which has a probability p of success, is

$$P(N, m, p) = p^m (1 - p)^{N-m} \frac{N!}{m!(N - m)!}. \tag{2.46}$$

Confidence intervals are used to infer the error of the measured probability $p = m/N$. The upper and lower errors are calculated from the 'Clopper-Pearson confidence limits',

p_+ and p_-, which are given by [65]

$$\sum_{r=m+1}^{N} P(N,r,p_+) = \frac{1+C}{2} \tag{2.47a}$$

$$\sum_{r=0}^{m-1} P(N,r,p_-) = \frac{1+C}{2}, \tag{2.47b}$$

where $C = 68.3\%$ is the 1σ confidence level. Equation (2.47a) defines p_+ such that the probability to obtain more than m successes out of N trials equals $(1+C)/2$. Likewise the p_- is determined such that the probability to obtain less than m successes equals the same limit. p_+ and p_- must be computed numerically, because of their implicit definition. We finally obtain the positive and negative errors, Δp_+ and Δp_-, of the measured probability p:

$$\Delta p_+ = p_+ - p \qquad \text{and} \qquad \Delta p_- = p - p_-. \tag{2.48}$$

Δp_+ and Δp_- indicate the error bars in all graphs throughout this thesis which show survival probabilities and efficiencies.

2.6 Conclusion and discussion

In this chapter, I have presented techniques permitting the control of the number of trapped atoms in either the magneto-optical trap or the dipole trap. Our high field gradient MOT captures atoms from the background gas, and we exactly determine their number by observing the fluorescence light. This allows us to select any specific number of atoms and transfer them into our standing wave dipole trap.

Compared to previous experiments carried out with single atoms in our group, we have built an entirely new apparatus which provides more flexibility in the manipulation of the atoms. A major improvement of the new setup is the possibility of loading individual atoms on demand using the "magnetic umbrella" technique. This is possible because coils instead of permanent magnets produce the field gradient of the MOT. Thus, we can temporarily increase the loading rate of the MOT by lowering the magnetic field gradient.

The number of loaded atoms per time interval obeys Poissonian statistics. The mean atom number can be altered by varying the time of the low field gradient, such that we load exactly one atom at a time in 38% of the cases, which equals the theoretical maximum given by Poissonian statistics. This is a perfect starting position for all following experiments requiring an exactly known number of atoms. Of course, due to the statistical nature of the atom number in our trap, we have to post-select the events in which the desired number of atoms was present. This post-selection is done automatically with a computer program.

However, the most important experimental achievement presented in this chapter is the transfer of atoms from the MOT into the dipole trap and back with a very high transfer

efficiency of 97%. This high transfer rate is obtained for atom numbers $N < 10$; for higher numbers, up to 20% of the atoms are lost by inelastic collisions. Thus, we exactly know the number of atoms within the dipole trap, at least for small atom numbers. In this case, their lifetime is only limited by background gas collisions.

If desired, one could easily implement a feedback mechanism that keeps the number of atoms in the MOT at $N = 1$ for most of the time, as demonstrated by J. McClelland (NIST, Gaithersburg) [66]. The feedback mechanism shuts off the loading from an atomic beam, when one atom is present. If more than one atom is detected, they are expelled from the trap and the loading from the atomic beam is switched on again. Another method of controlling the atom number in a sub-Poissonian way is the use of microscopic dipole traps as is done in the group of P. Grangier (Orsay, France). A laser beam focussed to $w_0 = 0.7$ µm [67] creates a trap volume which is small enough to cause a "collisional blockade" mechanism such that the average number of atoms is locked to 0.5 over a large range of loading rates [68]. Note, that the tight focussing requires a huge objective, which has to be placed very near to the trap center. Our setup, however, permits more flexibility, especially for the aimed deterministic transport of atoms into a resonator.

Chapter 3

Deterministic delivery of a single atom

3.1 Introduction

For many experiments it is desirable to transport cold atoms from the region of cooling and trapping to other locations. To accomplish this, numerous groups have successfully guided atoms using electromagnetic forces, but in most of the experiments, atoms either freely expand [69] or move under the action of gravity along the guiding potential [70]. Controlled transport, however, which includes the placement of the atoms at a desired location, has only been achieved in a few experiments. One approach is to use time varying magnetic fields, created e. g. by a series of quadrupole coils [71]. With "atom-chips", i. e. nanofabricated structures for trapping and manipulating cold atoms, a magnetic conveyor-belt was realized [72]. Optical forces have recently been employed to translate a Bose-Einstein condensate [73].

However, all experiments quoted above are designed to transport large numbers of atoms at a time. For many experiments, especially in quantum information processing, there is a great interest in a tool delivering only a single atom or a known small number of atoms at a specific time. Our approach uses a time-varying standing wave optical dipole trap made of two counterpropagating laser beams, which traps atoms in separate potential wells, keeping them confined in all three dimensions. Motion of the standing wave is achieved by slightly detuning one of the laser beams. This "optical conveyor-belt" allows us to displace a single atom by macroscopic distances on the order of a centimeter with sub-micrometer precision [5, 6]. The same technique of moving optical lattices has been applied for the acceleration of large ensembles of atoms [74, 75]. Apart from the fact that we use a single atom only, our setup additionally permits an electronically controlled motion of the standing wave.

3.2 The optical conveyor belt

3.2.1 Moving a standing wave

Our "optical conveyor belt" consists of a standing wave dipole trap created by two counter-propagating laser beams. Mutual detuning of the laser beams moves the interference pattern together with the trapped atom along the optical axis. The motion of the standing wave can be understood intuitively in a simple picture. Assume the two beams are detuned by $-\Delta\nu/2$ and $+\Delta\nu/2$, respectively. In a reference frame moving at the velocity

$$v = \frac{\lambda\Delta\nu}{2} \tag{3.1}$$

both beams are Doppler shifted by the same amount in opposite directions such that their frequencies coincide, which results in a stationary standing wave (see Figure 3.1). In the laboratory frame, this corresponds to a motion of the standing wave along the optical axis at the velocity v. In the experimental realization, it is more convenient to detune only one of the beams by $\Delta\nu$ while keeping the other one at constant frequency.

For a standing wave dipole trap made of two Gaussian beams of slightly different frequencies ν_1 and ν_2, we have a position- and time dependent potential:

$$U(z,\rho,t) = U_0\,\frac{w_0^2}{w^2(z)}\,\exp\left(-\frac{2\rho^2}{w^2(z)}\right)\cos^2(\pi\Delta\nu t - kz), \tag{3.2}$$

where $\Delta\nu = \nu_1 - \nu_2 \ll \nu_1,\nu_2$ is the frequency difference of the two beams. Since this mutual detuning is much smaller than the frequency of the beams, the wavenumber is approximated as $k = 2\pi/\lambda$. Here $\lambda = c/\nu_1 \approx c/\nu_2 = 1064$ nm. For the case of equal frequencies, $\Delta\nu = 0$, the time dependence vanishes and Equation (3.2) is equal to the stationary standing wave potential of Equation (2.32).
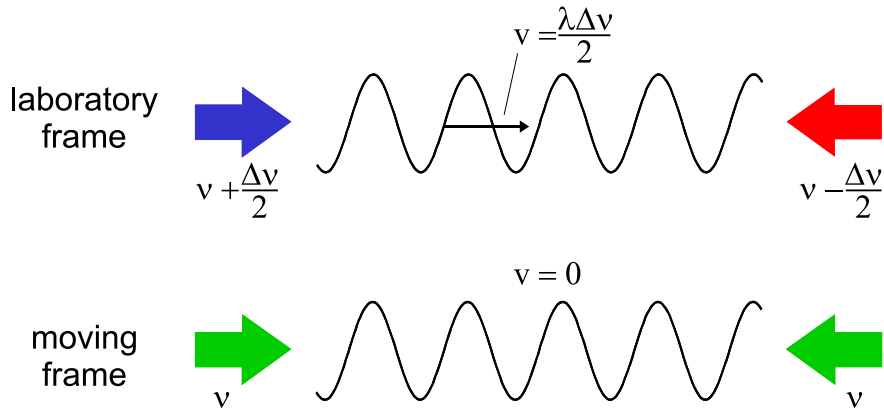
Figure 3.1: "Optical conveyor belt". Two counterpropagating laser beams of slightly different frequencies create a moving standing wave. In the moving reference frame both beams are doppler shifted by the same amount.
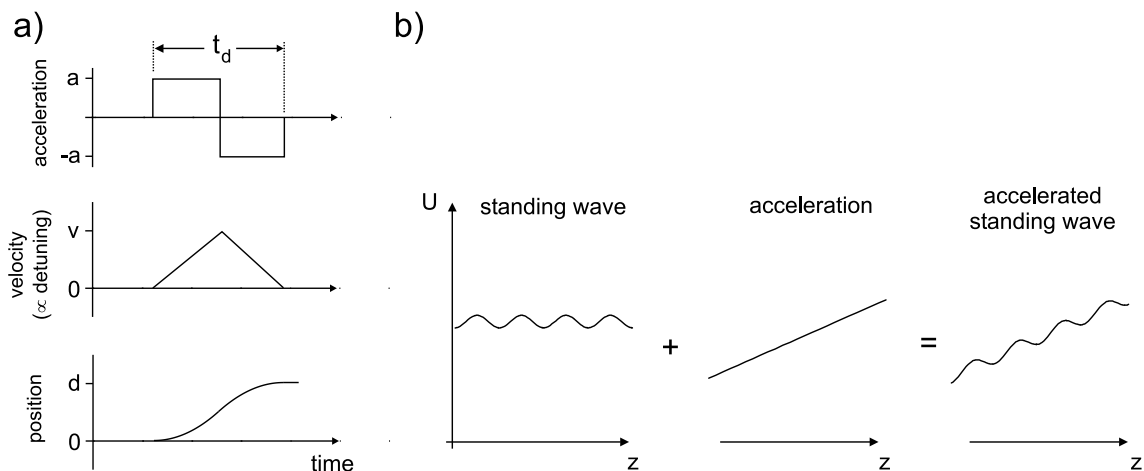
Figure 3.2: Accelerated standing wave. (a) The standing wave is uniformly accelerated and then decelerated within the transportation time t_d. (b) In the moving reference frame, the accelerated standing wave is the sum of the standing wave potential at rest and a linear ramp.

3.2.2   Acceleration of the potential

In our experiments, the standing wave is first accelerated to a maximum velocity and is subsequently decelerated in the same way to bring the atom to a stop. For this purpose, we linearly increase the frequency difference $\Delta\nu$ from zero to its maximum value, $\Delta\nu_{max}$, and then decrease it back to zero. This procedure results in a uniform acceleration and deceleration during the transport (see Figure 3.2).

Maximum acceleration

The potential on the beam axis $U(z')$ in the moving frame is the sum of the periodic standing wave and a linear contribution due to the acceleration:

$$U(z') = U_0 \cos^2(kz') + maz'. \tag{3.3}$$

Here, z' is the spatial coordinate in the accelerated reference frame. We have neglected the reduction of the potential due to the beam divergence. The result is a tilted standing wave potential (see Figure 3.2(b)) with an effective potential depth $U_\mathrm{eff} < U_0$. The atom remains trapped in this tilted potential until the accelerating force exceeds the dipole force, which is equivalent to the condition that local minima exist:

$$\frac{dU(z')}{dz'} = 0 \quad \Rightarrow \quad ma - kU_0 \cos(2kz') = 0. \tag{3.4}$$

From this we obtain the maximum acceleration, a_0, at which the potential wells vanish:

$$a_0 = \frac{kU_0}{m}. \tag{3.5}$$
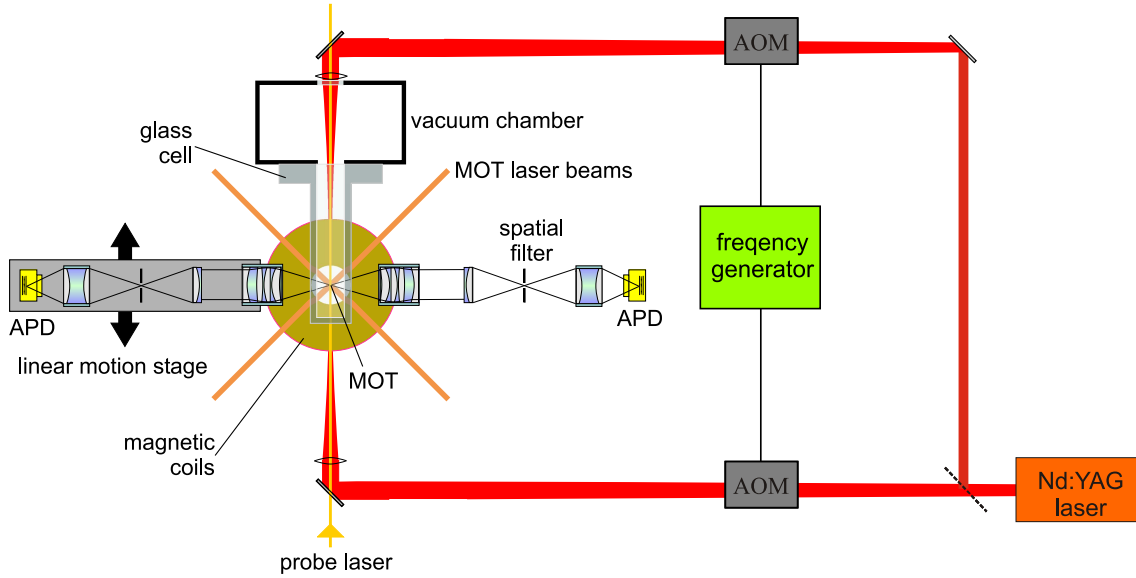
Figure 3.3: Experimental setup of the optical conveyor belt. AOMs are used to control the frequencies of the two laser beams that form the dipole trap. The fixed imaging optics on the right-hand side is used to monitor the fluorescence at the MOT position. The imaging optics mounted on the linear motion stage on the left-hand side is used for atom detection at any spot along the dipole trap.

For a typical trap depth of $U_0 = 1$ mK the maximum acceleration is $a_0 = 3.6 \times 10^5$ m/s^2. Note that the above model assumes a very cold atom trapped in the ground state of the potential wells. Since a hot atom has a higher kinetic energy and oscillates in the potential wells, it will be lost before reaching the theoretical limit. Experimentally, we realized this limit within a factor of two (see Section 3.4.1).

3.2.3 Experimental realization

To control the motion of the standing wave interference pattern, we decided to use acousto-optical modulators (AOM), which mutually detune the frequencies of the two dipole trap laser beams. Several other approaches were also considered when planning the current experiment. The first is to retro-reflect one of the trap laser beams by a mirror, whose translation would result in a travelling wave. Its disadvantage is a less stable optical setup compared to an AOM and much lower transportation velocities of typically 10 cm/s. This mechanical solution would avoid the heating effect due to the phase noise of the AOM drivers (see Section 2.5.1). A second alternative to move the standing wave is the use of an electro-optical modulator (EOM) which phase-shifts one of the laser beams. An adiabatic shift from 0 to 2π moves the interference pattern along with the trapped atom by $\lambda/2$. Then, one has to rapidly switch the phase from 2π back to 0 without the atom being able to follow. Repeating this procedure n times transports the atom over the distance of $n\lambda/2$. This approach would simplify the optical setup at the cost of placing demanding requirements on the EOM driver.

Our realization of the optical conveyor belt using AOMs is shown in Figure 3.3. Since it is impossible to drive an AOM with frequencies starting from DC, we must install a modulator in each arm of the dipole trap and change the difference of their driving frequencies. In order to avoid deviation of the beams while changing the frequency, the AOMs are set up in double pass configuration (not shown in Figure 3.3, for details see [55]). The modulators (Crystal Technology, 3110-125) operate at a center frequency of $f_0 = 100$ MHz yielding a maximum double pass deflection efficiency of 70%.

Transportation parameters

It is essential to change the frequency difference of the two modulators in a phase-continuous way because the relative phase is directly transferred to the spatial phase of the standing wave. Any motion of the potential wells that is not adiabatic with respect to the axial oscillation of the atom might lead to heating or even to the loss of the trapped atom. We use a digital frequency synthesizer with two synchronized outputs for this purpose. Its features are described in detail in the next section. It linearly sweeps one of the output frequencies in a phase-continuous way from f_0 to $f_0 + \Delta f_{\max}$ and back to f_0, while the other modulator remains at f_0. Since the AOMs are set up in double pass configuration, the maximum relative detuning of the AOM frequencies, $\Delta f_{\max}$, is translated into an optical detuning of $\Delta \nu_{\max} = 2\Delta f_{\max}$. These frequency sweeps accelerate and decelerate the standing wave structure achieving a maximum velocity of $v = \lambda \Delta f_{\max}$. The duration of the overall displacement procedure, t_{d} (see Figure 3.2), determines the acceleration

$$a = \pm \frac{2\lambda \Delta f_{\max}}{t_{\mathrm{d}}}. \tag{3.6}$$

The moving potential wells of the dipole trap thus displace the atom by the distance

$$d = a \frac{t_{\mathrm{d}}^2}{4}. \tag{3.7}$$

This distance can be controlled with sub-micrometer precision by heterodyning both frequencies of the AOM drivers. A counter monitors the number of cycles of the resulting beat signal during a frequency sweep, which directly measures the transportation distance in multiples of λ.

Frequency generator

For the generation of the phase-continuous sweeps with frequencies around 100 MHz we use a custom built dual frequency synthesizer (APE Berlin, DFD 100). It consists of two digital synthesizer units locked to a single master oscillator. Its heart is a chip (Analog Devices, AD9852) which digitally synthesizes the required waveform. The essential parameters such as the center frequency f_0, the maximum frequency detuning $\Delta f_{\max}$ and the sweep time

t_{sweep}, are transmitted to the device via an RS232 interface. Up to eight different parameter sets for $(\Delta f_{\text{max}}, t_{\text{sweep}})$ can be stored, permitting complex transportation sequences with different velocities and displacements. During the experiment, it is convenient to chose the total transportation time t_{d} and distance d. From these values the parameters of the frequency synthesizer are calculated:

$$\Delta f_{\text{max}} = \frac{2d}{t_{\text{d}}\lambda} \qquad \text{and} \qquad t_{\text{sweep}} = \frac{t_{\text{d}}}{2}. \tag{3.8}$$

The operation of the synthesizer is triggered by the computer control system. A signal on one of the three TTL input channels initiates the programmed sweep. The logic level of another input determines whether the first or the second generator performs the sweep, which is used to reverse the motion of the conveyor belt. The third TTL input is used to switch to the next programmed parameter set. Finally, two analog inputs $(0 - 5$ V$)$ are used to control the RF output power. We found that the relative phase fluctuations of the two RF outputs cause heating of the trapped atoms. We observed that the lifetime in a trap of $U_0 = 1.3$ mK depth was reduced to 3 s, compared to 25 s for the identical trap without AOMs (see Section 2.5.1).

3.3   Demonstration of the transport

To demonstrate the working of the conveyor belt, it is necessary to detect the transported atom at its new position with high spatial resolution. For this purpose, we use position-sensitive fluorescence detection inside the dipole trap and the fluorescence signal from the MOT.

3.3.1   Detection scheme - resonant illumination

To detect the transported atom, we use a second optical system together with an APD which is identical to the system used for detecting fluorescence from the MOT (Figure 3.3). Detector and imaging optics are mounted on a linear motion stage, which can be moved parallel to the standing wave to the aimed destination of the transported atom with a precision of 5 µm. Spatial filters in the imaging system limit the field of view to a radius of 40 μm, which is much smaller than the typical displacements. The fixed imaging optics permanently monitors the MOT region, both to verify the initial presence of a single atom in the MOT and to confirm its absence after displacement.

We illuminate the atom in the dipole trap with a probe laser, resonant to the free transition $(F = 4 \rightarrow F' = 5)$, which is overlapped with a repumping laser $(F = 3 \rightarrow F' = 4)$ in order to provide cyclic optical excitation. The light shifts of the atomic transition by several 10 MHz, arising from the dipole trap laser, can simply be compensated for with higher laser power. The beams are focused to $w_0 = 100$ µm by the same lens used for focussing the dipole trap laser (see Figure 3.3). Due to the small beam diameter we can increase the probe laser intensity to $10 I_0$ at the position of the atoms without obtaining a measurable contribution of stray light from reflections off the glass cell or
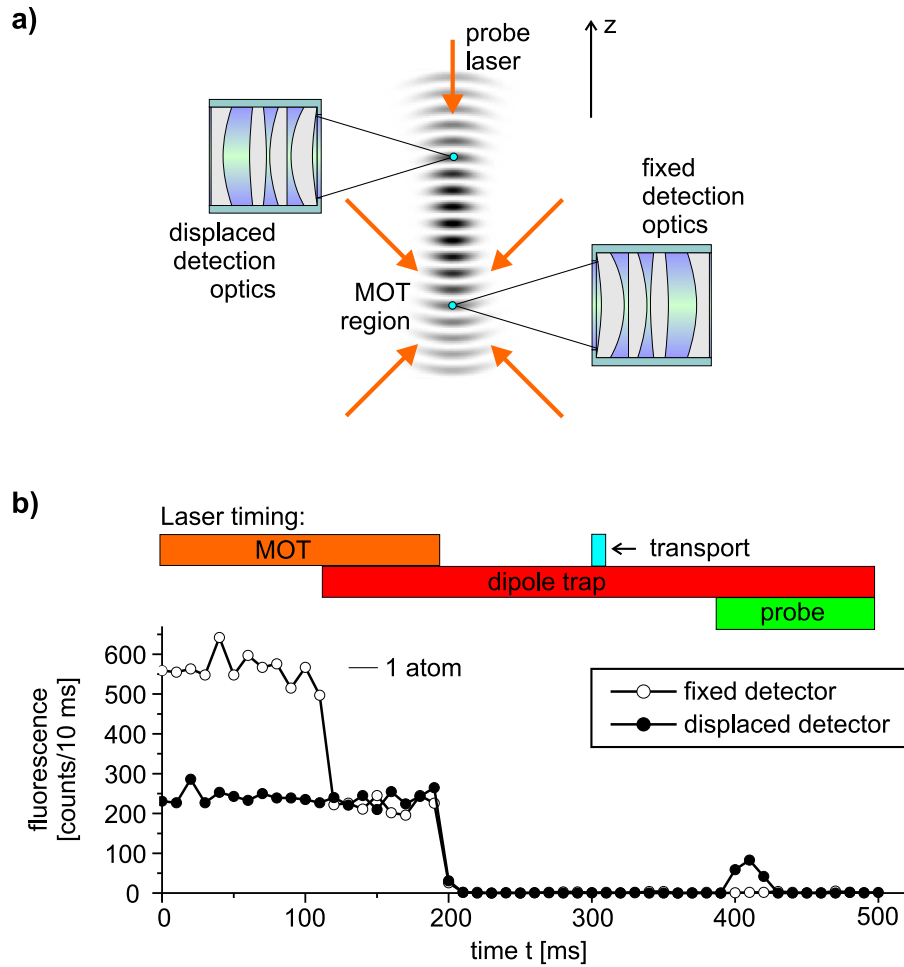
Figure 3.4: Detection of a transported atom. a) Fluorescence from the MOT and from the new position of the atom is collected by two independent detectors. b) The fixed detector (open circles) initially confirms the presence of the atom in the MOT. The burst of fluorescence at $t = 400$ ms detected with the displaced detector (full circles) originates from the same atom displaced by 0.5 mm, which is illuminated in the dipole trap with a resonant probe laser.

from fluorescence photons of background gas atoms.

Proof of the transport

To demonstrate the transport at the single atom level, we initially transfer one atom from the MOT into the dipole trap before the MOT lasers and magnetic field are switched off. Then, the atom is displaced by $d = 0.5$ mm within a time $t_d = 9.34$ μs using a maximum detuning of the AOMs of $\Delta f_{\max} = 50$ kHz. Here, the maximum dipole trap depth at the focus is $U_0 = 1.3$ mK, obtained with a total power $P = 4$ W and a beam waist $w_0 = 30$ μm.

The first detection of a single transported atom is shown in Figure 3.4. The signals show the photon counts from the fixed (open circles) and from the displaced APD (full circles), binned in time intervals of 10 ms. The bars on top of the graph show the timing sequence of MOT, dipole trap and probe laser. Initially, at $t = 0$, the fixed APD shows the presence of a single atom in the MOT, whereas the displaced detector only detects stray light of the MOT laser beams. The fluorescence yield per atom of the fixed detector has been calibrated independently. The stray light seen by the displaced detector is higher than for the fixed one, since at its initial position, more reflections from the glass cell hit the objective lens. At $t = 100$ ms, the atom is transferred from the MOT into the dipole trap. When both traps are simultaneously operated, the fluorescence of the atom in the MOT decreases, because the dipole trap laser shifts the atomic transition out of resonance. By coincidence, the resulting fluorescence level is the same as the stray light level of the displaced detector. After the MOT has been switched off, the atom is displaced by 0.5 mm by applying a frequency ramp with the above mentioned parameters to one of the AOMs starting at $t = 300$ ms. Finally, at $t = 400$ ms, we illuminate the atom with the resonant probe laser. Now the signal of the displaced detector shows a burst of photons, whereas the fixed detector does not register any photons. This clearly demonstrates that the atom has disappeared from the place of the MOT and has been successfully transported to its new location.

Figure 3.5(a) shows an enlarged view of the photon bursts of single transported atoms recorded by the displaced detector. For comparison, a reference signal without transportation is shown in Figure 3.5(b). The signals are obtained from an experiment almost identical to the one presented above, with a slightly shortened sequence however, which
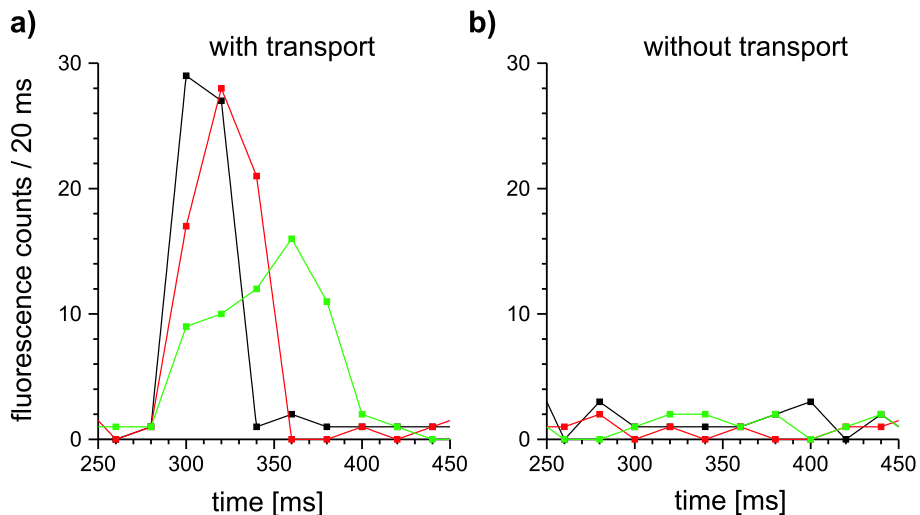
Figure 3.5: Photon bursts of single displaced atoms. (a) Three single atoms in the dipole trap after being moved by 0.5 mm. (b) Stray light background and detector noise.
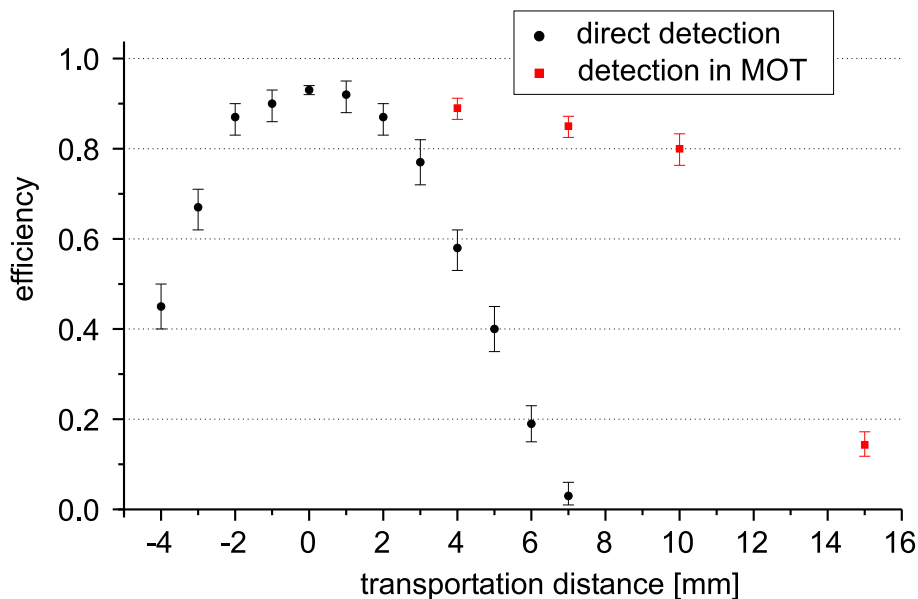
Figure 3.6: Transportation efficiency of the optical conveyor belt. Each data point results from about 100 shots performed with one atom each. Circles: The atom is detected by resonant illumination at its new position. Squares: More efficient detection by moving the atom back and recapturing it into the MOT.

explains the appearance of the bursts at $t = 280$ ms. From a single atom we can obtain more than 50 fluorescence photons within 100 ms (for a detailed discussion see the next section). The corresponding signal without atom amounts to typically 3 photons within the same interval originating mostly from dark counts of the APD (ca. 30 s^{-1}) and stray light background of the laboratory and lasers.

3.3.2 Maximum transportation distance

The measured probability of observing the transported atom as a function of the displacement z is shown in Figure 3.6 (circles). Each point results from about 100 shots performed with one atom each. We thus have to repeat the experiment about 300 times since on average we only load one atom every third shot (see Section 2.4.3). The fluorescence level of the MOT allows us to post-select the runs where only one atom was present. Detection of the transported atom is accomplished by resonant illumination, as described above. The atom is considered as detected if a fluorescence burst substantially exceeds (more than 6 photons) the background (2.6 ± 0.3 photons on average) within a time interval of 40 ms. The error of the resulting probabilities is calculated using the Clopper-Pearson confidence intervals (see Section 2.5.2).

We find that for small transportation distances, the fraction of detected atoms is above 90%, which equals the transfer efficiency between the two traps at the day of the measurement. In other measurements, we could even obtain transportation efficiencies

above 98% (see Figure 3.9). The measured efficiency drops to zero at $z = 7$ mm. In the following we will show that the position dependence of the trap depth limits this detection efficiency. For larger displacements from the laser focus some of the atoms are ejected from the trap before enough photons have been detected.

Number of detected photons

The focusing of the trapping laser beams to $w_0 = 30$ µm yields a Rayleigh length of $z_0 = 3$ mm. Due to the divergence of the Gaussian trapping beams, the local trap depth U_0 scales with the displacement z from the focus (see Equation (2.32)) as

$$U(z) = U_0 \left(1 + \frac{z^2}{z_0^2} \right)^{-1}. \tag{3.9}$$

During resonant illumination each absorption and emission process increases the atomic energy by one recoil energy $E_r = \hbar^2 k^2 / 2m = 100$ nK. The fluorescence signal lasts until the atom is evaporated out of the trap, which occurs on average after

$$N(z) = \frac{U(z)}{2E_r} \tag{3.10}$$

scattering events. Due to the beam divergence and the resulting reduction of $U(z)$, the fluorescence signal decreases for larger distances. An atom trapped in the focus of the dipole trap ($U(0) = 1.3$ mK) scatters $N(0) = 6500$ photons before it is lost. Multiplication with the theoretical detection efficiency $\eta = 8 \times 10^{-3}$ defined in Equation (2.41) yields $N'(0) = \eta N(0) = 52$ detected photons.

For comparison with the observed values, we counted the number of photons detected in the fluorescence bursts as a function of transportation distance (see Figure 3.7). The data is fitted with a Lorentzian curve (amplitude N_0 and offset N_{offs}) accounting for the divergence of the Gaussian beam with Rayleigh length z_0 along its axis:

$$N_{\text{fit}}(z) = N_0 \left(1 + \frac{z^2}{z_0^2} \right)^{-1} + N_{\text{offs}}. \tag{3.11}$$

The fitted maximum number of detected photons $N_0 = 32.4 \pm 1.2$ remains below the calculated number $N'(0) = 52$. There are several reasons for this difference. First, Equation (3.10) is valid for atoms trapped in the ground state of the potential well. From independent measurements [64] we inferred a temperature of about 100 µK, for comparable trap parameters, which corresponds to 10% of the trap depth. As a result, the fluorescence yield is reduced by the same amount, since we need less photons to heat the atom out of the trap. Second, the real trap depth will be below the calculated trap depth, because of non-perfect spatial overlap of the dipole trap lasers. This uncertainty in the trap depth is estimated to be in the order of 10% as well. The third and dominant reason is that η is not exactly known, since additional losses of fluorescence photons occur at
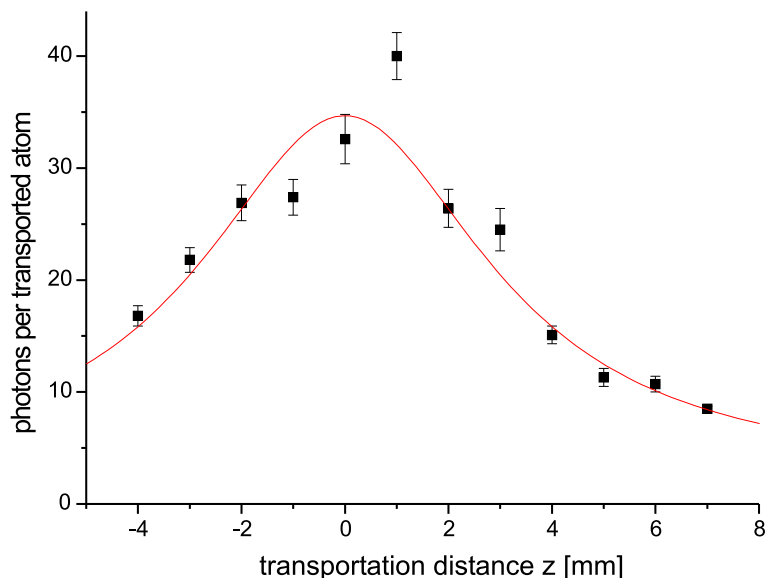
Figure 3.7: Number of fluorescence photons as a function of transportation distance z. The line is a fit with a Lorentzian according to Equation (3.11), yielding $N_0 = 32.4 \pm 1.2$, $N_{\mathrm{offs}} = 2.2 \pm 0.8$, and $z_0 = 3.4 \pm 0.2$.

the surfaces of the lenses and the glass cell or due to imperfect alignment of the imaging optics. The fitted offset $N_{\mathrm{offs}} = 2.2 \pm 0.8$ is in good agreement with the average number of dark counts of $N_{\mathrm{dark}} = 2.6 \pm 0.3$, which is inferred from the datasets where initially no atom was present in the MOT. Finally, the Rayleigh length of $z_0 = 3.4 \pm 0.2$ mm obtained from the fit reasonably agrees with the expected value of $z_0 = 3$ mm.

Detection by transporting back into the MOT

The above analysis reveals that for large displacements transported atoms cannot be efficiently detected by resonant illumination. In order to show that the real transportation efficiency is much higher, we have used the MOT to detect the atom with near to 100% efficiency. Without resonant illumination, the displaced atom is transported back to $z = 0$ before we switch on the MOT lasers to reveal the presence or absence of the atom. The results of this measurement are shown in Figure 3.6 (squares). Even for distances as large as $z = 10$ mm the two-way transportation efficiency remains 80%. At $z = 15$ mm, however, the efficiency drops to 16%. The atom is lost at this distance, because the dipole trap is too weak to compensate the gravitational force acting on the atom.

3.3.3 Influence of gravity

In our setup, the beam axis of the dipole trap is oriented horizontally such that gravity acts in the radial direction of the trap (see Figure 2.6). Thus, the potential in the vertical direction (y-axis) is the sum of the radial dipole trapping potential and the gravitational
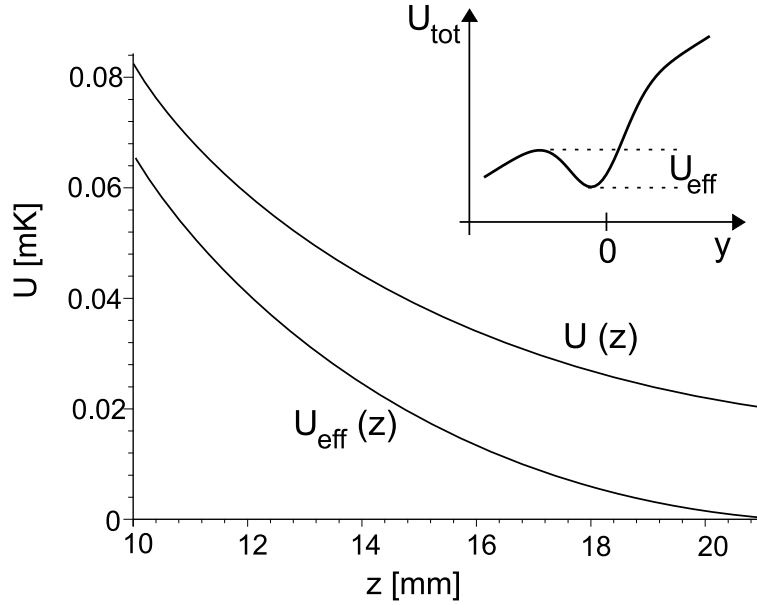
Figure 3.8: Reduction of the trap depth due to gravity. The inset shows the sum U_{tot} of the dipole potential and the gravitational potential versus the radial coordinate y for an arbitrary potential well along the optical $z-$axis. Below, the resulting effective potential depth $U_{\text{eff}}(z)$ is compared to the pure dipole potential $U(z)$ for $z = 10 - 21$ mm.

potential $U_{\text{grav}}(y) = mgy$

$$U_{\text{tot}}(x, y, z) = U(z)e^{-2(x^2+y^2)/w(z)^2} + mgy. \tag{3.12}$$

The effect of an additional accelerating potential has been discussed in the case of the accelerated standing wave (see Section 3.2.2). In the same way the acceleration due to gravity tilts the Gaussian potential wells in the y-direction, which reduces the trap depth to $U_{\text{eff}}(z)$, shown in the inset of Figure 3.8. $U_{\text{eff}}(z)$ is calculated numerically from the difference of the local extrema. Figure 3.8 shows a comparison of $U_{\text{eff}}(z)$ with the original dipole potential $U(z)$ in the range of $z = 10 - 21$ mm assuming a maximum depth of $U_0 = 1.3$ mK. Unlike $U(z)$, which falls off as $1/z^2$, the reduced potential $U_{\text{eff}}(z)$ completely disappears $z = 21$ mm. This represents the fundamental upper bound for the transportation distance in our dipole trap.

However, due to its initial energy, we lose the atom at even smaller distances. This interpretation is supported by a previous independent measurement in a stationary standing wave. We measured the survival probability of the atom after an adiabatic lowering of the trap [64]. We observed that 80% of the atoms survive if the trap depth is reduced from U_0 to $0.03\,U_0$, which equals the effective potential depth $U_{\text{eff}}(z)$ at $z = 13$ mm. However, a reduction to $0.01\,U_0$, which corresponds to a displacement of $z = 17$ mm, yielded a survival probability of only 10%. This is in good agreement with the measured transportation efficiency of 16% at $z = 15$ mm.
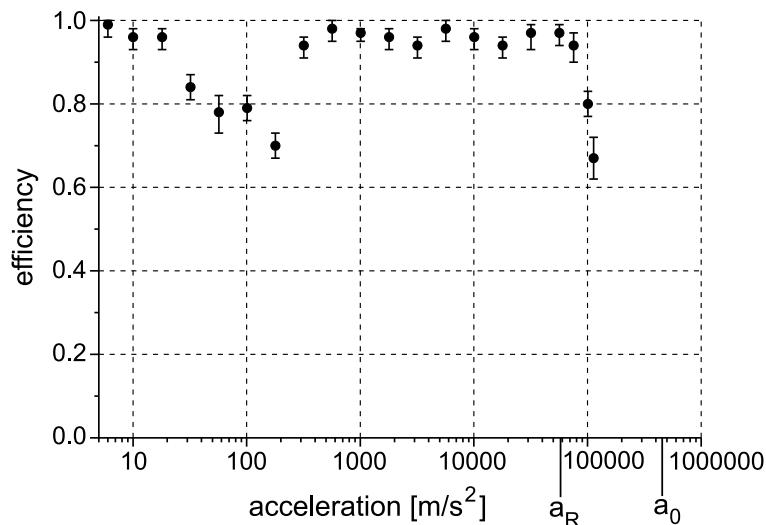
Figure 3.9: Transportation efficiency for a displacement of 1 mm as a function of the acceleration. The transportation efficiency for a displacement of 1 mm remains well above 90% when the acceleration is varied over several orders of magnitude. The decrease of the transportation efficiency around $a = 100 \, \text{m/s}^2$ is attributed to a partial reflection of one of the laser beams on the glass cell which interferes with the standing wave and may cause either resonant or parametric heating of the atom [76].

3.4 Characterization of the conveyor belt

3.4.1 Variation of acceleration

We have investigated the transportation efficiency as a function of the acceleration for a constant displacement of 1 mm using resonant illumination detection. Although the acceleration a was varied over 4 orders of magnitude (Figure 3.9), we found a nearly constant transportation efficiency of more than 90% for $a < 7 \times 10^4 \, \text{m/s}^2$. For larger accelerations, the efficiency rapidly decreases. Note that the accelerations realized here even exceed that of the maximum resonant light pressure force, $a_\text{R} = \hbar k_\text{D2} \Gamma / (2m) = 6 \times 10^4 \, \text{m/s}^2$.

As discussed in Section 3.2.2, the potential in the accelerated frame is the sum of the periodic potential of the standing wave and the contribution of the accelerating force,

$$U(z', a) = U_0 \cos^2(kz') + maz'. \tag{3.13}$$

In the ideal case of an initially motionless atom, the acceleration could adiabatically be increased until the local minima of the standing wave disappear. The acceleration is thus fundamentally limited by the potential depth, $a_0 = U_0 k/m = 4.8 \times 10^5 \, \text{m/s}^2$. However, we observed a decrease of the transportation efficiency to 66% already at $a = 1.13 \times 10^5 \, \text{m/s}^2 = 0.24 \, a_0$. There are two effects that experimentally limit the maximum acceleration to this lower value, which will be discussed in the following. The first is a heating effect due to abrupt changes of the acceleration and the second is the
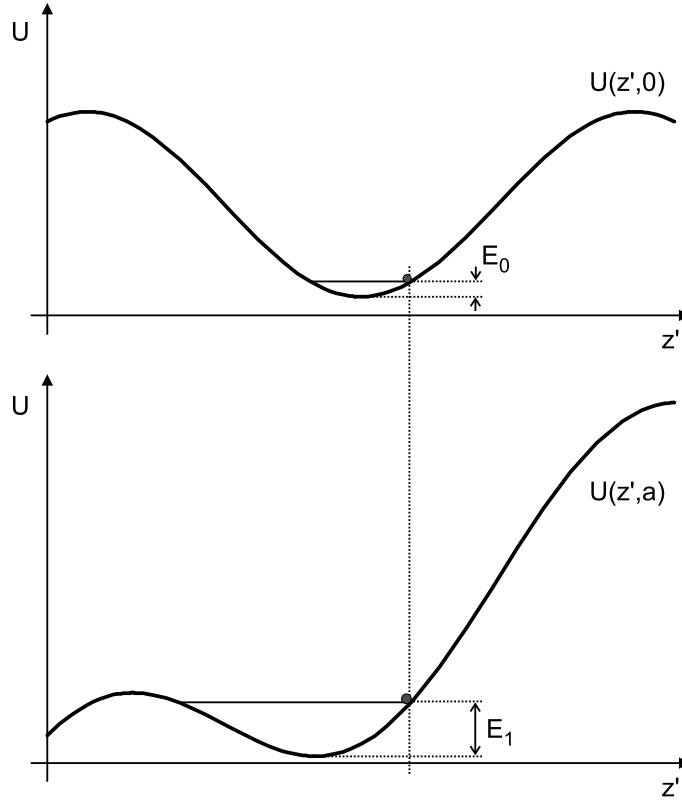
Figure 3.10: Heating due to abrupt acceleration, shown for a change of the acceleration from 0 to $a = 0.5\,a_0$. An atom with energy E_0 trapped in the potential at rest, $U(z',0)$, can obtain a higher energy $E_1 > E_0$ in the accelerated potential $U(z',a)$.

finite bandwidth of the AOMs.

Heating due to abrupt acceleration

At the beginning of the transportation process the acceleration is instantly switched from 0 to a, from a to $-a$ after half the transportation distance, and finally back to 0 (see Figure 3.2(a), p. 29). These three sudden changes of the potential either increase or decrease the kinetic energy of the atom depending on the phase of its oscillation.

In the following calculation we give an estimate of the maximum possible energy gains due to abrupt acceleration. The process is illustrated in Figure 3.10 for the case of a change of the acceleration from 0 to $a = 0.5\,a_0$. We start with an atom with energy E_0 trapped in the potential at rest, $U(z',0)$. In the worst case, as shown, an abrupt change of the potential occurs at the time when the atom has reached the turning point of its oscillatory motion. As a consequence, the atom has a higher energy $E_1 > E_0$ in the accelerated potential $U(z',a)$.

a)

b)
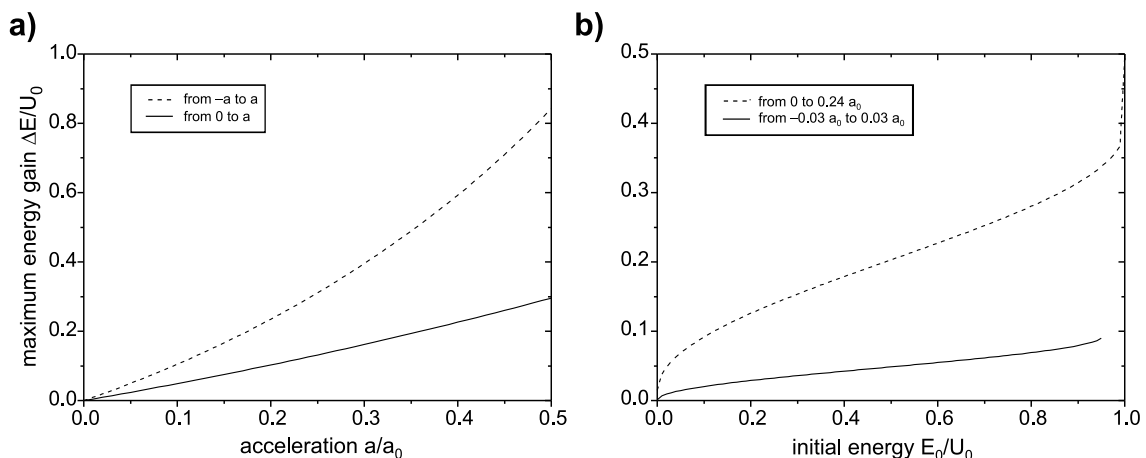
Figure 3.11: Energy gain due to abrupt acceleration. (a) Maximum energy gain ΔE due to an abrupt change of the acceleration from 0 to a (straight line) and from $-a$ to a (dotted line) assuming an initial energy $E_0 = 0.2\,U_0$. (b) Maximum energy gain vs. initial energy E_0 for a change from 0 to $0.24\,a_0$ (dotted line) and from $-0.03\,a_0$ to $0.03\,a_0$ (straight line). The value $a = 0.03\,a_0$ is used in Chapter 5 for the "quantum state transportation".

The maximum energy gains $\Delta E = E_1 - E_0$ as a function of the initial energy E_0 and the initial and final accelerations, can easily be calculated numerically. Figure 3.11(a) shows ΔE due to an abrupt change of the acceleration from 0 to a (straight line) and from $-a$ to a (dotted line) assuming an initial energy $E_0 = 0.2\,U_0$. Figure 3.11(b) shows the energy gain ΔE vs. the initial energy E_0 for a change from 0 to $0.24\,a_0$ (dotted line). From the numerical calculations, we can easily infer the energy gains after several changes of a by successively calculating the maximum energy gains ΔE. The calculations yield that an atom at $E_0 = 0.2\,U_0$ can obtain an energy gain of $\Delta E = 0.5\,U_0$ after the first two changes of the acceleration from 0 to $0.24\,a_0$ and from $0.24\,a_0$ to $-0.24\,a_0$, which are the parameters for the last datapoint (Figure 3.9). Note that an atom cannot be lost during the third change of the potential from $-0.24\,a_0$ to 0. However, the energy gain during the first two changes is sufficiently hight to result in a loss of the atoms out of the accelerated potential $U(z', 0.24\,a_0)$ which has an effective depth of $U_{\text{eff}} = 0.65\,U_0$.

Reduction of trap depth due to finite bandwidth of AOMs

The second factor that experimentally limits the maximum acceleration is the bandwidth of the AOMs, which mutually detune the two dipole trap laser beams. For the last datapoint in Figure 3.9 at $a = 1.13 \times 10^5\,\text{m/s}^2$, we have set the detuning of the frequency generator to its maximum value, $\Delta f_{\text{max}} = 10$ MHz ($t_{\text{d}} = 190\,\mu\text{s}$). For this detuning, the double pass AOM deflection efficiency decreases to 50% of its maximum value, which results in a decrease of the trap depth by 70%. As a consequence, the maximum acceleration also
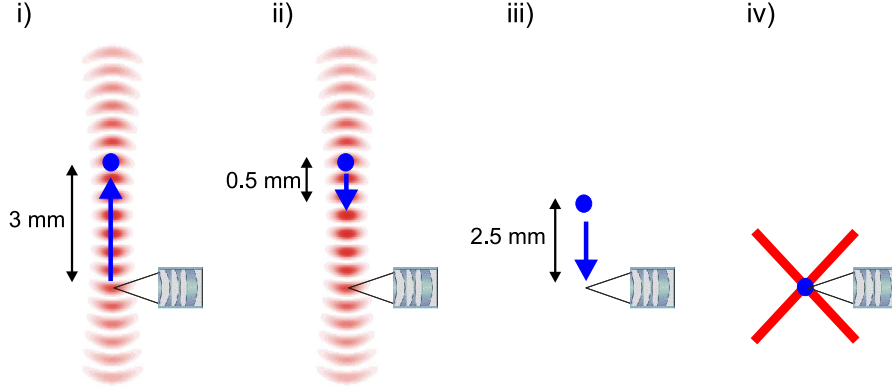
Figure 3.12: Ejection of a single atom into ballistic flight. (i) The atom is displaced from its initial position by 3 mm. (ii) Acceleration over a distance of 0.5 mm. (iii) Free flight over a distance of 2.5 mm. (iv) Recapture in the MOT.

decreases by the same factor to 3.4×10^5 m/s^2. Note that this value holds for atoms trapped in the ground state of the potential. An initial kinetic energy of $E_0 = 0.2 \, U_0$ further lowers the maximum achievable acceleration to 1.9×10^5 m/s$^2 = 0.39 \, a_0$.

Conclusion

In the above analysis, I have presented two mechanisms which are responsible for the observed loss of the atom at high accelerations. First, I calculated that the atom can gain enough kinetic energy due to the abrupt acceleration to be lost. Second, the trap depth is reduced during the transportation procedure because of the finite bandwidths of the AOMs. With our present measurement techniques, however, it is impossible to determine which effect prevails. In order to distinguish between the two loss mechanisms one would have to use a more sophisticated frequency synthesizer which permits an adiabatic increase of the acceleration in order to avoid heating of the trapped atom.

The decrease of the transportation efficiency around $a = 100 \, \text{m/s}^2$ is attributed to a modulation of the dipole trap potential caused by partial reflection of one of the laser beams on the glass cell. The reflected beam interferes with the standing wave which is thus phase and amplitude modulated. For certain detunings this effect causes either resonant or parametric heating of the atom [76]. This mechanism was used to measure the oscillation frequency of the atom in the trap [64] and will not be further discussed here. If required, the effect could be avoided by slightly changing the geometry of the setup or by selecting proper detunings of the two beams.

3.4.2 Ejection of a single atom into ballistic flight

In all manipulations described above, the dipole trap is never switched off. Here we demonstrate the ejection of a single atom into ballistic flight and its subsequent recapture. Using the conveyor belt as a "catapult" and the MOT as a target, we realized a rudimentary linear accelerator for a single atom (see Figure 3.12). Initially, a single atom is displaced by 3 mm, which is substantially larger than the capture region (about 300 µm) of our high-field gradient MOT. We now move the standing wave in the opposite direction, accelerating the atom back over 0.5 mm. It is then released 2.5 mm away from the MOT by switching off the standing wave within 0.1 µs. Now the atom is in ballistic flight at a velocity of 2 m/s towards the position of the MOT. Note that the initial temperature of the trapped atom limits the precision of this velocity (to about 5% in this case). However, the time of flight to the MOT position is still determined sufficiently accurately to turn on the MOT lasers in this time to recapture the atom. We measured that $83 \pm 4\%$ of the atoms initially present in the MOT were recaptured. Taking into account the transportation efficiency to 3 mm of $90 \pm 3\%$, we lost only 8% of the atoms during the catapulting.

However, we found that the recapture efficiency is reduced to 20% if we direct the atom into the operating MOT. This could indicate that the MOT is not a perfectly defined target, since slight misalignment of the MOT laser beams causes unbalanced resonant light forces to deflect the atom from its path before dissipative forces capture it in the center of the trap.

3.5 Conclusion and discussion

Our optical conveyor belt permits the controlled transport of individual atoms over centimeter distances with micrometer precision. We have systematically investigated the transportation efficiencies as a function of the displacement and the acceleration using different detection methods. For our parameters, we obtained an efficiency of 80% for a displacement of 10 mm. For higher displacements the efficiency drastically drops since from a certain point on, the dipole force is too weak to hold the atom against gravity. We also found that the realized accelerations approach the theoretical limit within less than a factor of two allowing us to change the atomic velocity from zero to a maximum velocity of 10 m/s within only 100 μs.

By heterodyning the two AOM driving frequencies, the transportation distance is controlled with a precision of λ. However, the absolute accuracy of the position of the atom is limited by its localization in the MOT to about ± 20 µm. A tighter control of the position of the trapped atom could be achieved by temporarily increasing the field gradient immediately before we transfer the atom into the dipole trap.

Larger displacements could be achieved by using higher laser power or different beam geometries. A standing wave oriented vertically would permit much larger transportation

distances with the same power, since the dipole force in the axial direction is about two orders of magnitude larger than in the radial direction. Additional cooling of the atoms would also improve the performance of the conveyor belt with respect to both transportation efficiency and atomic localization.

Chapter 4

Microwave spectroscopy

4.1 Introduction

It is the aim of this chapter to demonstrate the coherent manipulation of the hyperfine ground states of cesium atoms trapped in our optical dipole trap. This is accomplished by means of microwave radiation – a technique which has proven extremely useful in the realization of atomic clocks for many decades. In 1967, the 13th General Conference of Weights and Measures formally redefined the second as "9,192,631,770 periods of the radiation corresponding to the transition between the two hyperfine levels of the ground state of the cesium-133 atom". The precision of atomic clocks relies on the fact that this hyperfine transition is extremely narrow, rather limited by technical reasons than by the natural linewidth.

In our case of individual atoms, special experimental techniques had to be developed allowing us to prepare and to detect the hyperfine ground states at the single atom level. To describe the interaction of the atom with the microwave radiation field and its dynamical evolution, the Bloch vector model is known to be adequate, because of the semiclassical treatment of the system. In this model, a classical radiation field interacts with a quantum mechanical two-level atom.

The Bloch equations were first introduced by F. Bloch in 1946 in the context of nuclear magnetic resonance (NMR) phenomena [77]. Three differential equations govern the dynamics of the Bloch vector, a macroscopic magnetization vector, under the influence of magnetic fields. We will use a variant, the so-called *optical Bloch equations*. The formalism is identical to the description of the dynamics of a spin-1/2-particle in a magnetic field. However, instead of a real spin, we deal with the temporal evolution of a pseudo-spin vector, whose components describe the atomic polarization and the population difference. In our application of the Bloch vector model, experimental procedures such as the action of a resonant microwave pulse of specific duration or the free evolution of the system are expressed as geometrical rotations of the Bloch vector.

4.2   Theoretical framework

An isolated atom can possess a permanent magnetic dipole moment, which is directly connected to the total angular momentum of the atom. In our case we deal with time varying or precessing magnetic dipole moments, which arise if the atom is in a superposition of two angular momentum eigenstates.

More specifically, we drive the transition between the $F = 3$ and $F = 4$ hyperfine levels of the $6^2S_{1/2}$ ground state of cesium. Due to its insensitivity to magnetic stray fields, we will mostly use the $|F = 3, m_F = 0\rangle \rightarrow |F = 4, m_F = 0\rangle$ clock transition in a Zeeman split spectrum. This justifies the treatment of our system as a two-level atom interacting with the magnetic field part of a monochromatic electromagnetic wave.

4.2.1   Optical Bloch equations

I will only briefly sketch the derivation of the optical Bloch equations here; a more detailed treatment can be found in the book of Allen and Eberly [78]. The most essential steps are the semiclassical treatment, replacing the expectation values of the field operators by the classical fields, and the transition to the rotating frame, where we can apply the rotating wave approximation.

We start with the Hamiltonian $\hat{H}$ of the system, given by

$$\hat{H} = \hat{H}_A + \hat{\boldsymbol{\mu}} \cdot \hat{\boldsymbol{B}}, \tag{4.1}$$

where $\hat{H}_A$ is the unperturbed atomic Hamiltonian, $\hat{\boldsymbol{\mu}}$ is the magnetic dipole operator and $\hat{\boldsymbol{B}}$ the magnetic field operator. The matrix representation of the operators $\hat{H}$ and $\hat{\boldsymbol{\mu}}$ in the basis of the two energy eigenstates of the system, $\{|+\rangle, |-\rangle\}$, reads

$$\hat{H}_A = \begin{pmatrix} \frac{\hbar\omega_0}{2} & 0 \\ 0 & -\frac{\hbar\omega_0}{2} \end{pmatrix}, \qquad \hat{\boldsymbol{\mu}} = \begin{pmatrix} 0 & \boldsymbol{\mu}_r + i\boldsymbol{\mu}_i \\ \boldsymbol{\mu}_r - i\boldsymbol{\mu}_i & 0 \end{pmatrix}. \tag{4.2}$$

Here, ω_0 is the transition frequency between $|+\rangle$ and $|-\rangle$. Note that in the case of a $\Delta m = 0$ transition $\boldsymbol{\mu}_i$ vanishes. For $\Delta m = \pm 1$ transitions, i.e. for transitions induced by circularly polarized magnetic fields, $\boldsymbol{\mu} = \boldsymbol{\mu}_r + i\boldsymbol{\mu}_i$ is always a complex vector.

The magnetic dipole operator can be rewritten as $\hat{\boldsymbol{\mu}} = \boldsymbol{\mu}_r \hat{\sigma}_1 - \boldsymbol{\mu}_i \hat{\sigma}_2$ by using the Pauli matrices. Likewise, the atomic Hamiltonian $\hat{H}_A$ is expressed in this representation,

$$\hat{H}_A = \frac{\hbar\omega_0}{2}\hat{\sigma}_3. \tag{4.3}$$

The time dependence of the system is calculated in the Heisenberg picture, which uses time dependent operators. We obtain the time evolution of the three Pauli operators using the Heisenberg equation of motion:

$$i\hbar\, \dot{\hat{\sigma}}_j = [\hat{\sigma}_j, \hat{H}], \quad j = 1, 2, 3. \tag{4.4}$$

Insertion of Equation (4.1) into (4.4) leads to the following equations of motion for the three Pauli matrix operators

$$\dot{\hat{\sigma}}_1 = -\omega_0 \hat{\sigma}_2 + \frac{2}{\hbar}(\boldsymbol{\mu}_\mathrm{i} \cdot \hat{\boldsymbol{B}})\hat{\sigma}_3 \tag{4.5a}$$

$$\dot{\hat{\sigma}}_2 = \omega_0 \hat{\sigma}_1 + \frac{2}{\hbar}(\boldsymbol{\mu}_\mathrm{r} \cdot \hat{\boldsymbol{B}})\hat{\sigma}_3 \tag{4.5b}$$

$$\dot{\hat{\sigma}}_3 = -\frac{2}{\hbar}(\boldsymbol{\mu}_\mathrm{r} \cdot \hat{\boldsymbol{B}})\hat{\sigma}_2 - \frac{2}{\hbar}(\boldsymbol{\mu}_\mathrm{i} \cdot \hat{\boldsymbol{B}})\hat{\sigma}_1 \tag{4.5c}$$

These equations resemble the evolution of a real spin system, as for example in nuclear magnetic resonance. Here however, the Pauli matrix operators describe a pseudo-spin system. As we will see later, the expectation values of $\hat{\sigma}_1$ and $\hat{\sigma}_2$ are interpreted as the components of the magnetic polarization, whereas $\hat{\sigma}_3$ denotes the population difference.

Semiclassical treatment

It is well known that in the regime of high microwave power, a semiclassical treatment is applicable, in which a quantization of the electromagnetic field is not required. Neglecting correlations between atom and field, we can factor the operator products as $\langle \hat{\boldsymbol{B}}(t)\hat{\sigma}_\mathrm{i}(t) \rangle = \langle \hat{\boldsymbol{B}}(t) \rangle \langle \hat{\sigma}_\mathrm{i}(t) \rangle$. In this semiclassical treatment, the expectation value of the magnetic field operator is the classical field, $\langle \hat{\boldsymbol{B}}(t) \rangle = \boldsymbol{B_0} \cos \omega t$. We introduce the notation

$$s_\mathrm{i}(t) \equiv \langle \hat{\sigma}_\mathrm{i}(t) \rangle, \qquad i = 1, 2, 3 \tag{4.6}$$

and we will restrict ourselves to a $\Delta m = 0$ transition, such that $\boldsymbol{\mu}_\mathrm{i}$ vanishes.

Rotating wave approximation

The complicated dynamics of the Bloch vector are more clearly visible in a reference frame rotating at the microwave frequency ω. Using the transformation

$$\begin{pmatrix} u \\ v \\ w \end{pmatrix} = \begin{pmatrix} \cos \omega t & \sin \omega t & 0 \\ -\sin \omega t & \cos \omega t & 0 \\ 0 & 0 & 1 \end{pmatrix} \begin{pmatrix} s_1 \\ s_2 \\ s_3 \end{pmatrix} \tag{4.7}$$

we obtain

$$\dot{u} = \delta v + \Omega_\mathrm{R} \sin 2\omega t\, w \tag{4.8a}$$

$$\dot{v} = -\delta u + \Omega_\mathrm{R}(1 + \cos 2\omega t)w \tag{4.8b}$$

$$\dot{w} = -\Omega_\mathrm{R} \sin 2\omega t\, u - \Omega_\mathrm{R}(1 + \cos 2\omega t)v \tag{4.8c}$$

Here, we introduced the detuning $\delta = \omega - \omega_0$ and the Rabi frequency $\Omega_\mathrm{R} = \mu B_0 / \hbar > 0$.

Within the rotating wave approximation we neglect the quickly varying terms of frequency 2ω. Then, Equations (4.8a)-(4.8c) simplify to the well-known Bloch equations

$$\dot{u} = \delta v \tag{4.9a}$$

$$\dot{v} = -\delta u + \Omega_{\mathrm{R}} w \tag{4.9b}$$

$$\dot{w} = -\Omega_{\mathrm{R}} v \tag{4.9c}$$

which are equivalent to the single vector equation

$$\dot{\boldsymbol{u}} = -\boldsymbol{\Omega} \times \boldsymbol{u} \tag{4.10}$$

with the torque vector $\boldsymbol{\Omega} \equiv (\Omega_{\mathrm{R}}, 0, \delta)$ and the Bloch vector $\boldsymbol{u} \equiv (u, v, w)$. In the absence of damping, which will be introduced later, the Bloch vector has unit length, its evolution takes therefore place on a unit sphere.

The Bloch equations describe in excellent approximation the dynamics of an atom undergoing a magnetic dipole transition. The components of the Bloch vector can be interpreted as follows: The first two components, u and v, are the two components of the induced magnetic dipole moment, which are in phase and in quadrature with the driving field, $B_0 \cos \omega t$, respectively. The third component, w, describes the population difference of the two atomic levels. For $w = \pm 1$, only one of the levels is populated. Equation (4.9c) shows that v is the *absorptive* component of the dipole moment, which couples to the field and produces population changes in w, whereas u is the *dispersive* component.

4.2.2   State vector and density matrix representations

The Bloch vector formalism is equivalent to other representations of the two-level atom. We will point out how the coordinates of the Bloch vector transform into the corresponding state vector or the density matrix elements.

An arbitrary state vector, $|\psi\rangle$, is represented in the basis $\{|+\rangle, |-\rangle\}$ as

$$|\psi\rangle = a\,|+\rangle + b\,|-\rangle, \tag{4.11}$$

with complex probability amplitudes a and b satisfying the normalization condition $|a|^2 + |b|^2 = 1$. Remember that the components of the Bloch vector are the expectation values of the Pauli matrix operators, which can be expressed using the above state representation:

$$u = \langle \psi | \hat{\sigma}_1 | \psi \rangle = a^* b + a b^* \tag{4.12a}$$

$$v = \langle \psi | \hat{\sigma}_2 | \psi \rangle = -\mathrm{i}\,(a^* b - a b^*) \tag{4.12b}$$

$$w = \langle \psi | \hat{\sigma}_3 | \psi \rangle = |a|^2 - |b|^2 \tag{4.12c}$$

Note that we have transformed the $\hat{\sigma}_i$ to the rotating frame here.

Using a state representation of the form

$$|\psi\rangle = e^{-i\phi/2}\cos\frac{\theta}{2}\,|+\rangle + e^{i\phi/2}\sin\frac{\theta}{2}\,|-\rangle \tag{4.13}$$

we obtain the Bloch vector in spherical coordinates

$$u = \sin\theta\cos\phi \tag{4.14a}$$
$$v = \sin\theta\sin\phi \tag{4.14b}$$
$$w = \cos\theta. \tag{4.14c}$$

Its position on the unit sphere is determined by two angles, θ and ϕ. Here, θ is the angle of the Bloch vector with the w-axis, whereas ϕ describes the position in the uv-plane. Note that it is impossible to unambiguously calculate a and b from the Bloch vector coordinates, since any global phase factor $e^{i\varphi}$ in front of $|\psi\rangle$ drops out in the expectation values $\langle\psi|\hat{\sigma}_i|\psi\rangle$. The correct phases can only be inferred by directly solving the Schrödinger equation.

Density matrix

Another description of the system uses the density operator, which in the case of a pure state $|\psi\rangle$ is defined as $\hat{\rho} := |\psi\rangle\langle\psi|$. The matrix representation of the density operator in the basis $\{|+\rangle, |-\rangle\}$ is

$$\hat{\rho} = \begin{pmatrix} \rho_{++} & \rho_{+-} \\ \rho_{+-}^* & \rho_{--} \end{pmatrix} = \begin{pmatrix} |a|^2 & a^*b \\ ab^* & |b|^2 \end{pmatrix} = \frac{1}{2}\begin{pmatrix} 1+w & u+iv \\ u-iv & 1-w \end{pmatrix}. \tag{4.15}$$

This leads to the following dependence of the Bloch vector components on the density matrix elements:

$$u = 2\,\mathrm{Re}(\rho_{+-}) \tag{4.16a}$$
$$v = 2\,\mathrm{Im}(\rho_{+-}) \tag{4.16b}$$
$$w = \rho_{++} - \rho_{--}. \tag{4.16c}$$

The diagonal elements of the density matrix, ρ_{++} and ρ_{--}, are denoted as *populations*. They are functions of the w-component of the Bloch vector, which is the population difference. The off-diagonal elements, ρ_{+-} and ρ_{+-}^*, the so-called *coherences*, are functions of the polarization components u and v. Alternatively, these coherences can be written as a function of the probability amplitudes a and b. The resulting product term, a^*b, expresses the interference between $|+\rangle$ and $|-\rangle$ when the system is in a coherent superposition of these states [79].

The density matrix formalism is suitable to distinguish pure states from statistical mixtures. This distinction will be important in the next chapter, where we investigate the effect of decoherence, i.e. the mechanism how pure states evolve into a statistical mixture.

Decoherence manifests itself in a decay of polarization, thus in a decay of the off-diagonal elements of the density matrix. From the above representation it is easy to derive that

$$\rho^2 = \rho \tag{4.17}$$

if and only if the system is in a pure state.

Application to the cesium hyperfine transition

In most of our experiments, we prepare the atoms in the $|F = 4, m_F = 0\rangle$ state and measure the population transfer to $|F = 3, m_F = 0\rangle$ induced by the microwave radiation. The application of the Bloch vector formalism to this experimental situation is straightforward. We use the following correspondences of the cesium hyperfine states with the w-component of the Bloch vector and the states $|+\rangle$ and $|-\rangle$:

$$
\begin{array}{ccccc}
|F = 3, m_F = 0\rangle & & w = +1 & & |+\rangle \\
|F = 4, m_F = 0\rangle & \longleftrightarrow & w = -1 & \longleftrightarrow & |-\rangle
\end{array} \tag{4.18}
$$

After the application of one or a sequence of microwave pulses, the atom is in general in a superposition of both hyperfine states,

$$|\psi\rangle = c_3 |F = 3\rangle + c_4 |F = 4\rangle, \tag{4.19}$$

with complex probability amplitudes c_3 and c_4. However, our detection scheme (see Section 4.3.3) only allows us to measure the population, P_3, of the hyperfine state $F = 3$. P_3 is calculated from the w component of the Bloch vector:

$$P_3 = |c_3|^2 = \frac{w + 1}{2}. \tag{4.20}$$

4.2.3   Coherent dynamics

Although the Bloch equations cannot be solved analytically in general, special solutions exist for certain limiting cases. For resonant pulses ($\delta = 0$) or free precession without driving ($\Omega_\mathrm{R} = 0$) the solutions can be expressed as simple rotation matrices acting on the Bloch vector. This formalism will extensively be used in the next chapter to model the action of complex pulse sequences, as in the case of Ramsey spectroscopy and spin echo experiments.

Rabi oscillations

When the atom is exposed to monochromatic microwave radiation of constant amplitude, the population oscillates between the two levels and we observe the well known Rabi oscillations. If the Bloch vector is initially in the state $\boldsymbol{u}_0 = (0, 0, -1)$, we obtain the time evolution of the population:

$$w(t, \delta) = -1 + \frac{2\Omega_\mathrm{R}^2}{\delta^2 + \Omega_\mathrm{R}^2} \sin^2\left(\frac{1}{2}\sqrt{\delta^2 + \Omega_\mathrm{R}^2}\, t\right), \tag{4.21}$$
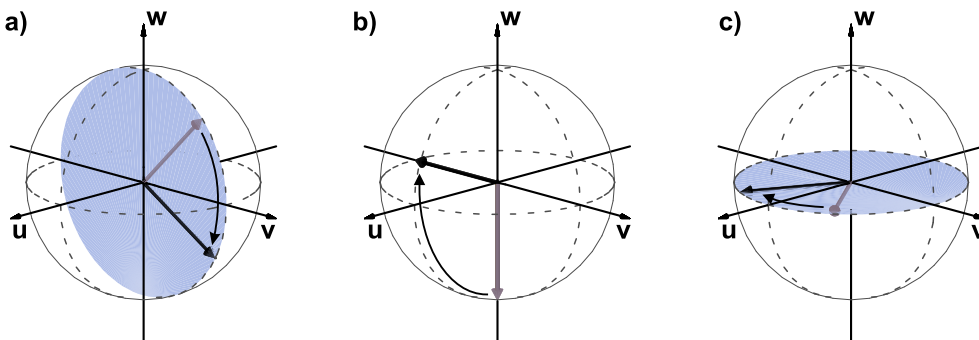
Figure 4.1: Bloch vector dynamics. (a) Resonant driving corresponds to a rotation around the u-axis. (b) A $\pi/2$-pulse transforms $(0, 0, -1)$ into $(0, -1, 0)$. (c) Free precession in the uv-plane.

which can be rewritten using the *generalized Rabi frequency* $\Omega = \sqrt{\delta^2 + \Omega_{\mathrm{R}}^2}$ as

$$w(t, \delta) = -1 + \frac{2\Omega_{\mathrm{R}}^2}{\Omega^2} \sin^2\left(\frac{\Omega t}{2}\right). \tag{4.22}$$

The denominator of Equation (4.21) shows the typical resonance behavior with a lorentzian lineshape of FWHM $2\Omega_{\mathrm{R}}$; this effect is denoted as *power broadening*. We also infer that complete population transfer is achievable only for the resonant case ($\delta = 0$):

$$w(t, 0) = -\cos\Omega_{\mathrm{R}}t. \tag{4.23}$$

Resonant pulses

It is straightforward to describe the effect of a resonant pulse ($\delta = 0$) on the Bloch vector with arbitrary initial coordinates $\boldsymbol{u}_0 = (u_0, v_0, w_0)$. In this case the Bloch equations have a simple solution of the form:

$$\boldsymbol{u}(t) = \Theta(t) \cdot \boldsymbol{u}_0, \tag{4.24}$$

where $\Theta(t)$ is a matrix which describes a rotation with angle $\theta(t)$ around the u-axis (see Figure 4.1(a)):

$$\Theta(t) = \begin{pmatrix} 1 & 0 & 0 \\ 0 & \cos\theta(t) & \sin\theta(t) \\ 0 & -\sin\theta(t) & \cos\theta(t) \end{pmatrix}. \tag{4.25}$$

The rotation angle $\theta(t)$ is the time integral of the Rabi frequency

$$\theta(t) = \int_0^t \Omega_{\mathrm{R}}(t')dt'. \tag{4.26}$$

For the experiments described in the next chapter, such as Ramsey spectroscopy and spin echoes, $\theta(t) = \pi/2$ and $\theta(t) = \pi$ are the two most important cases.

In the state vector representation, a resonant pulse of duration t is expressed by the application of a unitary operator $U(t)$ to the state vector:

$$| \psi(t) \rangle = U(t) | \psi(0) \rangle \tag{4.27}$$

A derivation of $U(t)$ is presented in [80], which yields:

$$U(t) = \begin{pmatrix} \cos \dfrac{\theta(t)}{2} & -i \sin \dfrac{\theta(t)}{2} \\ -i \sin \dfrac{\theta(t)}{2} & \cos \dfrac{\theta(t)}{2} \end{pmatrix}. \tag{4.28}$$

$\pi/2$-pulse

In the case of a pulse with area $\theta(t_{\pi/2}) = \pi/2$ the rotation matrix reduces to

$$\Theta_{\pi/2} := \Theta(t_{\pi/2}) = \begin{pmatrix} 1 & 0 & 0 \\ 0 & 0 & 1 \\ 0 & -1 & 0 \end{pmatrix}. \tag{4.29}$$

Thus, a $\pi/2$-pulse flips the v and w components of the Bloch vector.

If the atom is initially prepared in one of the basis states $| + \rangle$ or $| - \rangle$, a $\pi/2$ pulse transforms it into a superposition state:

$$| + \rangle \quad \rightarrow \quad \frac{1}{\sqrt{2}} \left(| + \rangle - i | - \rangle \right) \tag{4.30}$$

$$| - \rangle \quad \rightarrow \quad \frac{1}{\sqrt{2}} \left(| - \rangle - i | + \rangle \right). \tag{4.31}$$

π-pulse

For the case of a π-pulse, $\theta(t_\pi) = \pi$, the rotation matrix reduces to

$$\Theta_\pi := \Theta(t_\pi) = \begin{pmatrix} 1 & 0 & 0 \\ 0 & -1 & 0 \\ 0 & 0 & -1 \end{pmatrix}, \tag{4.32}$$

which shows that a π-pulse transforms v into $-v$ and w into $-w$. In the quantum mechanical representation it flips the basis states according to:

$$\begin{aligned} | + \rangle &\quad \rightarrow \quad -i | - \rangle \\ | - \rangle &\quad \rightarrow \quad -i | + \rangle. \end{aligned} \tag{4.33}$$

Thus, we see that a 2π-pulse does not transform the wavefunction into itself, but multiplies it with a phase factor -1, such that $| \psi \rangle \rightarrow - | \psi \rangle$. This behavior is due to the specific quantum mechanical state representation of Equation (4.13) in which the rotation angles are divided by a factor of two. It is formally equivalent to the minus sign arising in the wavefunction of spin-1/2-system if it undergoes a full rotation in real space.

Free precession

Without driving ($\Omega_\mathrm{R} = 0$) the Bloch vector precesses around the w-axis with angular frequency δ. The rotation matrix $\Phi_\mathrm{free}(t)$ describes its evolution during a time t

$$\boldsymbol{u}(t) = \Phi_\mathrm{free}(t) \cdot \boldsymbol{u}_0, \tag{4.34}$$

with

$$\Phi_\mathrm{free}(t) = \begin{pmatrix} \cos\phi(t) & \sin\phi(t) & 0 \\ -\sin\phi(t) & \cos\phi(t) & 0 \\ 0 & 0 & 1 \end{pmatrix} \tag{4.35}$$

The total precession angle, $\phi(\delta, t)$, represents the accumulated phase during the free evolution of the Bloch vector:

$$\phi(t) = \int_0^t \delta(t')dt' \tag{4.36}$$

As we will see later, the detuning $\delta(t)$ in general varies spatially and in time, depending on the energy shifts of the atomic levels.

In the state representation, the free precession corresponds to the multiplication with a phase factor

$$\begin{array}{ccc} |+\rangle & \rightarrow & e^{i\phi(t)/2} \ |+\rangle \\ |-\rangle & \rightarrow & e^{-i\phi(t)/2} \ |-\rangle. \end{array} \tag{4.37}$$

4.3 Experimental methods

Special experimental methods had to be developed in order to prepare and to detect the atomic hyperfine state at the level of a single atom. They are the prerequisite for the observation of microwave spectra or Rabi oscillations as well as for the application of Ramsey spectroscopy techniques in our experiment.

4.3.1 Setup

The experimental setup, shown in Figure 4.2, is essentially the same as in the previous chapters. We use the magneto-optical trap as a source of cold atoms which are transferred into the dipole trap, where all experiments are performed. All our measurements rely on counting the number of atoms in the MOT before and after any intermediate experiment in the dipole trap. Here, we use the fixed APD for the counting of fluorescence photons. Except for the experiments in Section 5.5 we do not transport the trapped atoms. We only use the AOMs to change the dipole trap laser intensity. A microwave antenna (see below) is placed close to the vacuum cell. Since the following experiments are very sensitive to magnetic fields, we use three orthogonal pairs of coils to compensate the earth's magnetic field (see Section 4.4.1). The compensation coils of the z-axis also serve to produce a guiding field, which defines the quantization axis.
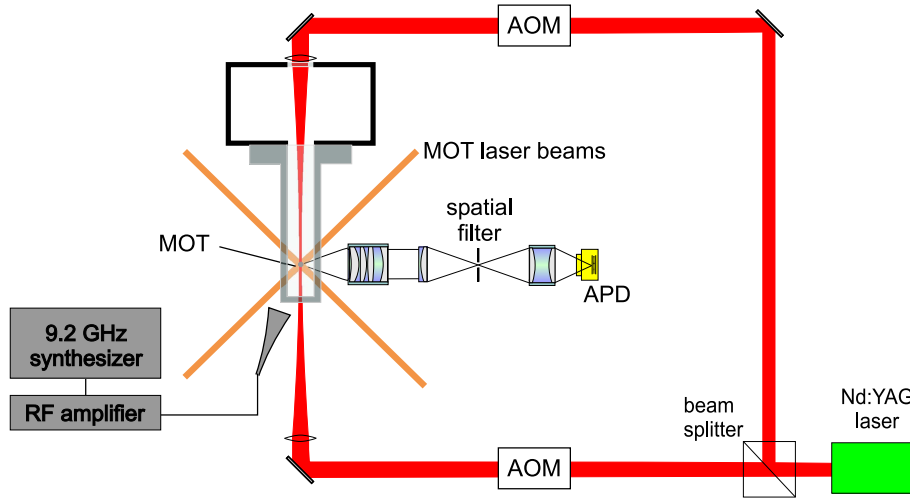
Figure 4.2: Setup for microwave spectroscopy. The atoms are exposed to microwave radiation generated by a synthesizer.

Laser beams

Apart from MOT and dipole trap lasers, we have to shine in differently polarized laser beams from different directions to perform optical pumping and state selective detection (see Figure 4.3).

MOT lasers The MOT cooling laser is the same as in the previous chapters. It is locked to the $F = 4 \rightarrow F' = 3/5$ crossover transition and shifted by an AOM to the red side of the cooling transition $F = 4 \rightarrow F' = 5$. The MOT repumping laser is locked to the $F = 3 \rightarrow F' = 4$ transition, it is π-polarized and is shined in along the dipole trap axis.

Optical pumping To optically pump the atoms (see Section 4.3.2) we simply use the unshifted MOT cooling laser on the $F = 4 \rightarrow F' = 3/5$ crossover transition (see Section 2.3.3), since it is only detuned by $+25$ MHz from the required $F = 4 \rightarrow F' = 4$ transition. This small detuning is partly compensated for by the light shift of the dipole trap ($\hbar\Omega/4\Delta = 2\pi \times 21$ MHz for $U_0 = 1.0$ mK) and by simply using higher laser power. The optical pumping laser is also shined in along the dipole trap axis with π-polarization.

Push-out laser For the state selective detection (see Section 4.3.3) we use a so-called push-out laser, resonant to the $F = 4 \rightarrow F' = 5$ transition. It is σ^+-polarized and is shined in from above.

9 GHz source

To generate microwave pulses at the frequency of 9.2 GHz we use a synthesizer (Agilent 83751A, 0.01 - 20 GHz) which is locked to an external 10 MHz rubidium frequency
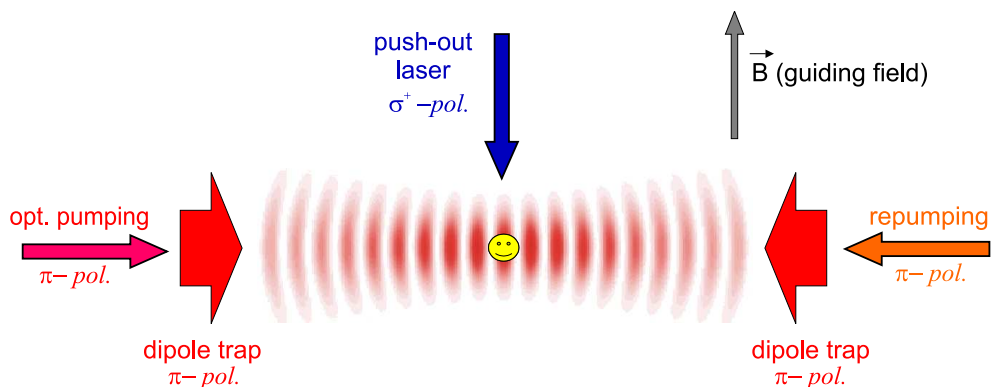
Figure 4.3: Polarization of laser beams.

standard (Stanford Research Systems, PRS10). Its specified accuracy is 10^{-11} which corresponds to 0.1 Hz at 9.2 GHz. The synthesizer is remote-controlled by the computer and has numerous features for its convenient use in spectroscopy applications. It can be operated in a stepped sweep mode such that the user can determine start and stop frequency and the number of steps. Whenever it receives a trigger pulse, the synthesizer increases the output frequency by a specific amount with a settling time of 10 ms. A pulse mode permits the generation of short square pulses (duration > 2 μs, rise/fall time < 100 ns) with a duration determined by an external trigger pulse. The device also allows amplitude and frequency modulation using two analog input channels. All sweep and modulation features can be used simultaneously.

The output of the synthesizer (max. +15 dBm) is sent to a power amplifier (Industrial Electronics, AM53-9-9.4-33-35), which amplifies the microwave signal by 36 dB up to a maximum output power of +38 dBm. The power amplifier is connected to a dipole antenna with a microwave horn (Sivers Lab, Sweden, PM 7320X) whose special shape ensures impedance matching from the antenna to free space. However, we found that we obtain higher microwave power at the location of the atoms when we remove the horn and place the dipole antenna as closely to the vacuum cell as possible. In all of the presented experiments we use the following configuration: Synthesizer (+10 dBm) → long cable (−8 dB) → amplifier (+36 dB) → short cable (−2 dB) → microwave antenna (+36 dBm, = 4.0 W).

4.3.2 State preparation

We use optical pumping to prepare the atom in a specific hyperfine state. If possible, the transitions are chosen such that the desired state is a dark state. Depending on the target state, we need differently polarized lasers from different directions. An overview of all lasers employed is shown in Figure 4.3.

Optical pumping

To pump the atom into $F = 3$ or $F = 4$ we introduce a delay between switching off the MOT repumping laser (resonant with the transition $F = 3 \rightarrow F' = 4$) and the MOT cooling laser (in close resonance with the transition $F = 4 \rightarrow F' = 5$). If we first switch off the repumping laser, the atom is pumped into the $F = 3$ state, whereas it is pumped into the $F = 4$ state if we first switch off the cooling laser. This scheme is used for the test of the state selective detection, see below.

However, pumping into a specific m_F state requires an additional optical pumping laser and a guiding field to define the quantization axis, which is applied perpendicularly to the dipole trap. According to selection, $\Delta F = 0$, $\Delta m_F = 0$ is a dipole forbidden transition, such that $|F = 4, m_F = 0\rangle$ is a dark state for a π-polarized laser on the $F = 4 \rightarrow F' = 4$ transition. We additionally shine in the π-polarized MOT repumping laser in order to depopulate the $F = 3$ ground state.

Compensation coils and guiding field

Compensation of the earth's magnetic field and the application of guiding fields is accomplished by three orthogonal pairs of coils surrounding the vacuum cell. They can sustain a continuous current of 5 A each which produces fields of about $100\,\mu\text{T}$. Two pairs of coils are driven by a standard laboratory power supply (Conrad Electronics, PS-2403D). To minimize their current noise, we installed low pass filters at the outputs. For the guiding field we use a remote controlled power supply (Elektro Automatik, EA-PS 3032-05) producing a current of $0 - 5$ A proportional to an external voltage $0 - 10$ V which is provided by the computer control system. Its rms noise is below 0.1 mA and it switches the magnetic fields within typically 2 ms. We monitor the currents of the three pairs of coils by measuring the voltage dropped across a shunt resistor ($R = 0.1\,\Omega$) with a 6-digit precision multimeter (Agilent, HP 34401A). For the method of setting the correct compensation currents, see Section 4.4.1.

Adjusting laser power and pulse duration

Power and pulse duration of the optical pumping laser are optimized experimentally, to maximize the population of the desired state and to minimize heating of the atoms. The temperature of the atoms is measured by adiabatically lowering the dipole trap such that a significant fraction of the atoms escapes [64]. To adjust the power of the optical pumping laser, a simple procedure was established. We switched on the laser for 10 ms and set its power to a value until we lose almost the same fraction of atoms during the adiabatic lowering with and without the optical pumping laser. Decreasing the optical pumping time to 1 ms now ensures that the laser does not heat the atoms significantly. Since the required power is far below the saturation limit, it strongly depends on the dipole trap laser power because the light shift of the optical pumping transition is in the order of several linewidths.

Additionally, we observed that during the lowering of the dipole trap the atoms do not remain optically pumped, instead the m_F states are completely mixed. Most experiments described in this chapter have to be performed in a lowered dipole trap of $U_0 < 0.2$ mK. However, we always transfer the atoms from the MOT into a deep dipole trap of $U_0 > 1$ mK to achieve a high transfer efficiency, before we lower the dipole trap depth prior to the application of e.g. sequences of microwave pulses. During the lowering of the trap the splitting of the Zeeman sublevels may equal the axial oscillation frequency. In that case the dipole trap laser, being not perfectly π-polarized, induces Raman transitions between the two degenerate levels $|\, m_F, n\,\rangle$ and $|\, m_F \pm 1, n \mp 1\,\rangle$, where n denotes the vibrational quantum number in the potential wells. As a consequence, the m_F states are mixed. Neglecting the different coupling strengths between the m_F sublevels an estimate of the mixing rate is given by the Rabi frequency for a Raman transition, $\Omega_{\mathrm{raman}} = \epsilon \Omega^2 / (2\Delta)$. Here, $\epsilon = 1\%$ denotes the fraction of σ polarized light of the dipole trap beam, whereas the Rabi frequency $\Omega^2 = 4 U_0 \Delta / \hbar$, see Equation (2.19). For $U_0 = 1$ mK, we obtain $\Omega^2 = 16\Gamma\Delta$, resulting in $\Omega_{\mathrm{raman}} = \epsilon 8\Gamma = 2\pi \times 416$ kHz. Thus, the states can be mixed on timescales of 1 µs, which is compatible to our observations. These transitions are exploited in the so-called degenerate Raman sideband cooling scheme [81, 82, 83] and it could be useful in the future to cool the atoms. At the present stage, we avoid this effect by pumping the atoms after lowering the dipole trap.

4.3.3 State selective detection

To detect whether a microwave transition has taken place, it is necessary to determine the atomic hyperfine state. State selective detection is performed by a laser which is resonant to the $F = 4 \rightarrow F' = 5$ transition and thus pushes the atom out of the dipole trap only if it is in $F = 4$. An atom in the $F = 3$ state, however, is not influenced by this laser. Thus, it can be transferred back into the MOT and be detected there. Although this method looks complicated at first sight, it is universal, since it works with many atoms as well as with a single one. Other methods, such as detecting fluorescence photons in the dipole trap by illuminating the atom with a laser resonant to the $F = 4 \rightarrow F' = 5$-transition, failed because the number of photons detected before it decays into the $F = 3$ state is not sufficient.

Push-out process

In order to achieve a high efficiency of the state selective detection process, it is essential to heat the atom out of the dipole trap before it is off-resonantly excited to $F' = 4$ and spontaneously decays into the $F = 3$ state. For this purpose, we use a σ^+-polarized push-out laser, such that the atom is optically pumped into the cycling transition $|\, F = 4, m_F = 4\,\rangle \rightarrow |\, F' = 5, m_F = 5\,\rangle$. Note that the polarization is not perfectly circular since the beam is shined in at a $2°$ angle with respect to the magnetic field axis. This entails an increased probability of exciting the $F' = 4$ level from where the atom can decay into the $F = 3$ ground state. To prevent this, we remove the atom from the trap sufficiently fast by shining in the push-out laser from the radial direction with high

a) preparation in F=4
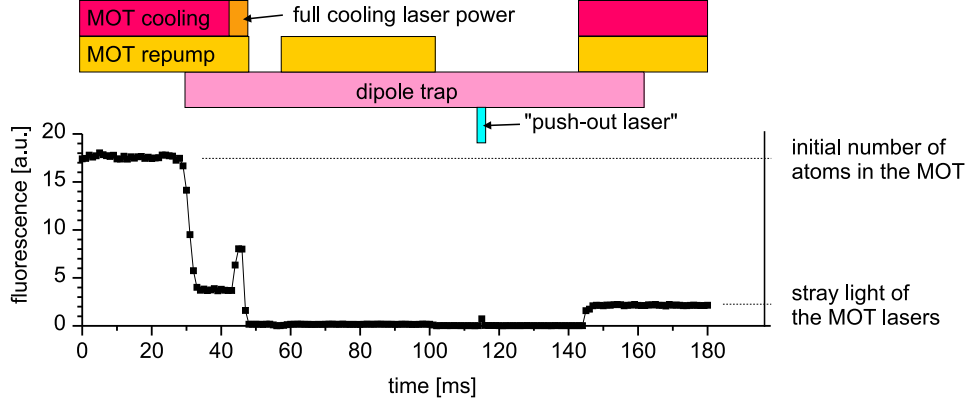
b) preparation in F=3
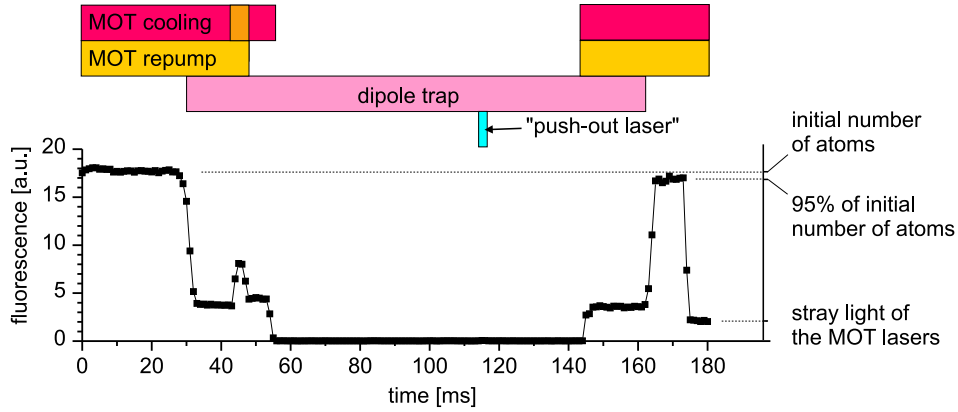
Figure 4.4: State selective detection. Shown are the integrated APD counts from the MOT region binned in time intervals of 1 ms and accumulated over 10 repetitions with 20 atoms each. The push-out laser removes all atoms in $F = 4$ from the trap (upper graph), whereas 95 % of the atoms in $F = 3$ remain trapped (lower graph).

intensity ($s_0 = I/I_0 \approx 100$, with $w_0 = 100$ µm, $P = 30$ µW). In this regime its radiation pressure force is stronger than the dipole force in the radial direction, such that we push out the atom within half the radial oscillation period ($\approx$ 1 ms). In this case, we linearly sum up all photon momenta $\hbar \boldsymbol{k}$,

$$p_{\mathrm{push}} = \left| \sum_{n=1}^{n_{\mathrm{push}}} \hbar \boldsymbol{k} \right| = n_{\mathrm{push}} \hbar k. \tag{4.38}$$

Here n_{push} is the number of photons needed to remove the atom from the trap, i.e. the total recoil energy, E_{push}, equals the trap depth U_0:

$$U_0 = E_{\mathrm{push}} = \frac{\boldsymbol{p}_{\mathrm{push}}^2}{2m} = \frac{n_{\mathrm{push}}^2 \hbar^2 k^2}{2m}. \tag{4.39}$$

Pushing is different from *heating* the atom out of the trap. Recoil heating dominates if the radiation pressure force of the push-out laser is weaker than the dipole force. The atom oscillates many times while absorbing and emitting photons such that the momentum transfer averages to zero. Each absorption and emission process increases the atomic energy by the one-photon recoil energy $E_r = \hbar^2 k^2 / 2m$. Here we need n_{heat} photons to heat the atom out of the trap:

$$U_0 = 2n_{heat}E_r = \frac{2n_{heat}\hbar^2 k^2}{2m}. \tag{4.40}$$

Comparison of equation (4.39) and (4.40) yields $n_{push} = \sqrt{2n_{heat}}$ indicating that it is more efficient to push than to heat the atom. If we adiabatically lower the trap to typically 0.12 mK prior to the application of the push-out laser, we need on average only $n_{push} = 35$ photons to push the atom out of the trap. This number is small enough to prevent off-resonant excitation and spontaneous decay to $F = 3$.

Results

A typical experimental sequence to test the state selective detection is shown in Figure 4.4. Less than 1% of the atoms prepared in $F = 4$ survive the application of the push-out laser. This number is limited by the efficiency of the state preparation rather than by the effectiveness of the push-out process. Still more than 95% of the atoms remain trapped if they are prepared in the $F = 3$ state. Here, most of the losses occur during the adiabatic lowering of the dipole trap.

We found that the state selective detection process also works if the push-out laser is π-polarized, however with a slightly worse efficiency. To obtain the same efficiencies in this case, we have to lower the trap depth by at least an additional factor of 2 compared to the parameters for the circular case. The additional lowering reduces the number of photons needed until the atom is pushed out, but at the same time it increases the probability of losing a hot atom.

4.3.4   Recording of spectra

The efficient state selective detection method allows us to systematically use microwave transitions. All experiments using microwave transitions are performed in the same way. Initially we prepare all atoms in $F = 4$, then we apply the microwave puls(es), and finally measure the population transfer to $F = 3$.

Timing sequence

The experiments presented in this chapter are more complex than the ones used for transportation of the atoms. Numerous pulses have to be synchronized, and experimental parameters have to be changed automatically from run to run. Due to this increased
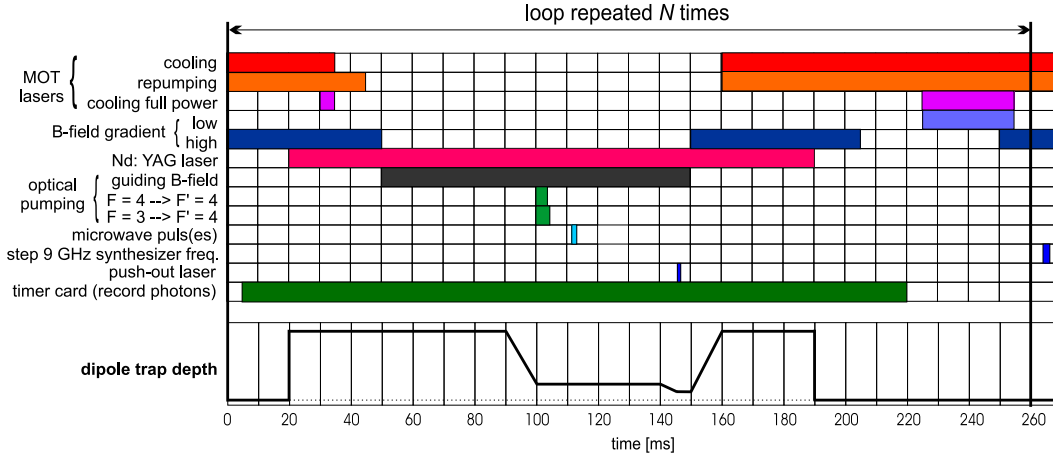
Figure 4.5: Typical timing sequence for microwave spectroscopy.

complexity, I present a (simplified) overview of a typical computer control sequence used for microwave spectroscopy and related experiments (see Figure 4.5). The bars mostly correspond to the digital channels which deliver TTL output signals, whereas analog output channels are used to change e. g. the intensity of the dipole trap lasers. The details of the setup and the employed techniques are described in Section 2.3. Here, I only present new features that have been installed additionally.

MOT lasers In order not to saturate the APD when we load about 50 atoms at a time, we decrease their fluorescence level to less than 600 counts/s. Typically MOT laser powers are 300 µW per arm. With a beam diameter of 2 mm this yields a saturation parameter $s_0 = I/I_0 = 8.5$. The detuning is typically $1.5\,\Gamma$. These parameters result in a relatively low fluorescence level of typically 6000 counts/s per atom, which is necessary not to saturate the APD when we load about 50 atoms at a time. During transfer of the atoms into the dipole trap we increase the MOT laser power for a few milliseconds to the maximum value of > 1 mW per arm to further cool the atoms (see Figure 4.4). The high power is required to compensate for the light shift of the atomic levels in the dipole trap which increases the effective MOT laser detunings.

Magnetic field During normal MOT operation we use a high magnetic field gradient of 300 G/cm, which is lowered to 20 G/cm at the end of each sequence to accelerate the loading of new atoms (see Section 2.4.3). During the experiments in the dipole trap the field gradient is switched off.

Nd:YAG laser The dipole trap laser is operated at full power when we transfer atoms between MOT and dipole trap. We then decrease its power to a lower level where we apply the microwave pulses. Eventually, the trap is lowered further for the state selective detection to facilitate the push-out process, as described above.

Optical pumping A guiding field of typically 100 µT is applied in z-direction, perpendicular to the dipole trap axis and the optical table. Details of the optical pumping

process are described in Section 4.3.2.

Microwave source Microwave pulses are applied to the optically pumped atom in the lowered dipole trap. The characteristics of the synthesizer were described in detail in Section 4.3.1. At the end of each sequence a pulse steps the frequency of the synthesizer to the next value.

Timer card The timer card registers photons only when an external gate signal is set to "high". For details on the timer card and the signal processing see Section 2.3.5.

We repeat the experiment with identical parameters 20 times, before the frequency of the 9 GHz-synthesizer is changed (see Figure 4.5). This allows us to record microwave spectra such as those shown in Figures 4.8 and 4.9. Alternatively, we can keep the microwave frequency fixed and vary other parameters like the pulse duration or other time intervals from run to run, which was done for the recording of Rabi oscillations (Section 4.4.3) or for Ramsey spectroscopy (Section 5.3).

Atom counting

To count the atoms we use their fluorescence light in the MOT, as shown in Figure 4.6. The number of atoms before and after any experimental procedure in the dipole trap, N_{initial} and N_{final}, is inferred from the measured photon count rates, C_{initial}, C_{final} and C_{backgr}:

$$N_{\text{initial}} = \frac{C_{\text{initial}} - C_{\text{backgr}}}{C_{\text{1atom}}} \quad \text{and} \quad N_{\text{final}} = \frac{C_{\text{final}} - C_{\text{backgr}}}{C_{\text{1atom}}}. \tag{4.41}$$

The fluorescence rate of a single atom, C_{1atom}, is measured independently. From the atom numbers we obtain the fraction of atoms transferred to $F = 3$,

$$P_3 = \frac{N_{\text{final}}}{N_{\text{initial}}}. \tag{4.42}$$

The error of P_3 is calculated by means of confidence limits as described in Section 2.5.2. We repeat the same measurement with identical parameters many times and add the fluorescence counts, in order to obtain good statistics. This procedure together with the atom counting is done automatically by a computer program.

4.4 Microwave spectroscopy

Unlike the possibility of coherent manipulation of the ground state hyperfine levels, microwaves are also valuable as a sensitive probe for level shifts due to magnetic fields. This allows us to compensate for the ambient magnetic field and to precisely calibrate externally applied fields.

We performed microwave spectroscopy both in the frequency and the time domain resulting in the observation of spectra or Rabi oscillations, respectively. The latter form the basis for the application of Ramsey spectroscopy in the next chapter, serving for the investigation of decoherence mechanisms.
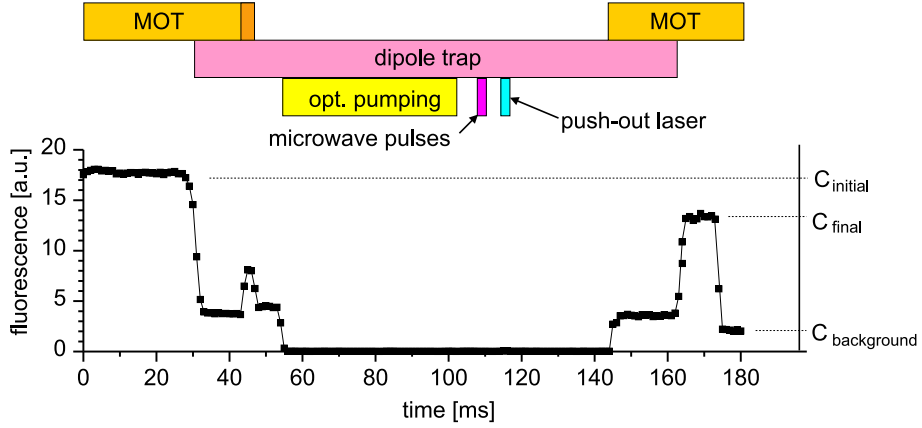
Figure 4.6: Atom counting. Initial and final number of atoms is inferred from their fluorescence in the MOT.

Zeeman splitting of hyperfine levels

For the understanding of microwave spectra it is essential to know the influence of magnetic fields on the atomic levels. The presence of a magnetic field B lifts the degeneracy of the magnetic sublevels $|F, m_F\rangle$ in each hyperfine manifold. Their shifts can be calculated analytically according to the Breit-Rabi-Formula [84]:

$$\Delta E_{F,m_F} = -\frac{\Delta E_{\mathrm{hfs}}}{2(2I+1)} - g_I \mu_{\mathrm{B}} m_F B \pm \frac{\Delta E_{\mathrm{hfs}}}{2}\sqrt{1 + \frac{4m_F}{2I+1}x + x^2}, \qquad (4.43)$$

where $x = (g_J - g_I)\mu_{\mathrm{B}}B/\Delta E_{\mathrm{hfs}}$. For Cesium the nuclear spin $I = 7/2$, the zero-field hyperfine splitting $\Delta E_{\mathrm{hfs}}/h = 9.2$ GHz, $g_J = 2.0$ and $g_I = -0.4 \times 10^{-3}$ are the electronic and nuclear Landé factors[1]. For small magnetic fields $B < 20$ T ($x \ll 1$), the energy shift is small compared to the hyperfine splitting and F is still a good quantum number. This is the regime of the linear Zeeman effect, where the Breit-Rabi-Formula yields the same results as first order perturbation theory. The transition from m_3 to m_4 is shifted due to the linear Zeeman effect by

$$\Delta \omega_{m_3 \to m_4} = 2\pi \times 3.51 \, \frac{\mathrm{kHz}}{\mathrm{\mu T}} \, (m_3 + m_4), \qquad (4.44)$$

see Figure 4.7. This corresponds to a shift of the outermost transition $m_3 = 3 \to m_4 = 4$ of 24.6 kHz/μT. In contrast, the transition $m_3 = 0 \to m_4 = 0$ experiences only a second order shift.

$$\Delta \omega_{0 \to 0} = \frac{(g_{\mathrm{J}} - g_{\mathrm{I}})^2 \mu_{\mathrm{B}}^2}{\Delta E_{\mathrm{hfs}}} = 2\pi \times 43 \frac{\mathrm{mHz}}{(\mathrm{\mu T})^2} \qquad (4.45)$$

This transition is commonly used in atomic clocks because of its insensitivity to magnetic (stray) fields. For the same reason we mostly use this transition as well.

[1] For the exact values see [85] and references therein.
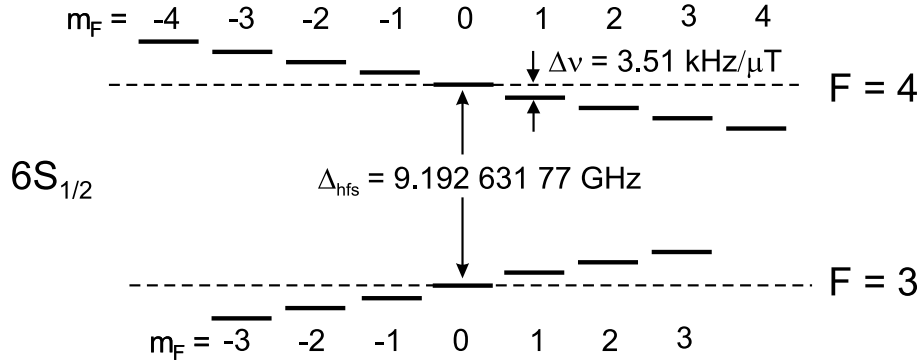
Figure 4.7: Zeeman splitting of magnetic sublevels of the $6^2S_{1/2}$ ground state of cesium. The energy of the magnetic sublevels is shifted due to the linear Zeeman effect. The shift is in opposite direction for the two sublevels $F = 3$ and $F = 4$.

4.4.1 Compensation of the earth's magnetic field

Optical pumping and a long lifetime of the populations of the m_F sublevels can only be achieved by imposing a proper quantization axis to the atoms. It is defined by the application of guiding fields with well-defined direction and strength. This necessitates a compensation of stray magnetic fields, such as the earth's magnetic field and those created by magnetized objects placed near the vacuum cell. The field compensation is achieved with three orthogonal pairs of coils placed around the vacuum cell. The coils are driven by currents of up to 5 A, yielding fields of about 100 µT. Finding the appropriate compensation currents is done in two steps. We use the influence of magnetic fields on the efficiency of optical pumping for a coarse compensation. For a fine compensation, we minimize the Zeeman splitting which is detected by microwave spectroscopy.

Coarse compensation

For the coarse compensation we observe the fluorescence from the cesium background gas in the vacuum cell, which is illuminated with a σ^+-polarized laser resonant to the $F = 3 \rightarrow F' = 2$ transition [86]. The atoms are optically pumped into the outermost states $|F = 3, m_F = 2\rangle$ and $|F = 3, m_F = 3\rangle$, which are dark states if the direction of the magnetic field coincides with the axis of the laser beam. Any magnetic field component perpendicular to this quantization axis mixes the m_F-levels since the magnetic polarization vector performs a Larmor precession around the total magnetic field axis. As a consequence, the populations of the m_F-levels are mixed. In particular, the dark states are depopulated yielding an increase of fluorescence. The fluorescence is observed with the avalanche photodiodes used for the detection of the atoms in the MOT. We adjust the currents in the two pairs of coils perpendicular to the beam such that the fluorescence is minimized. For the compensation of the third axis, we shine in the beam from another axis and repeat the same procedure.
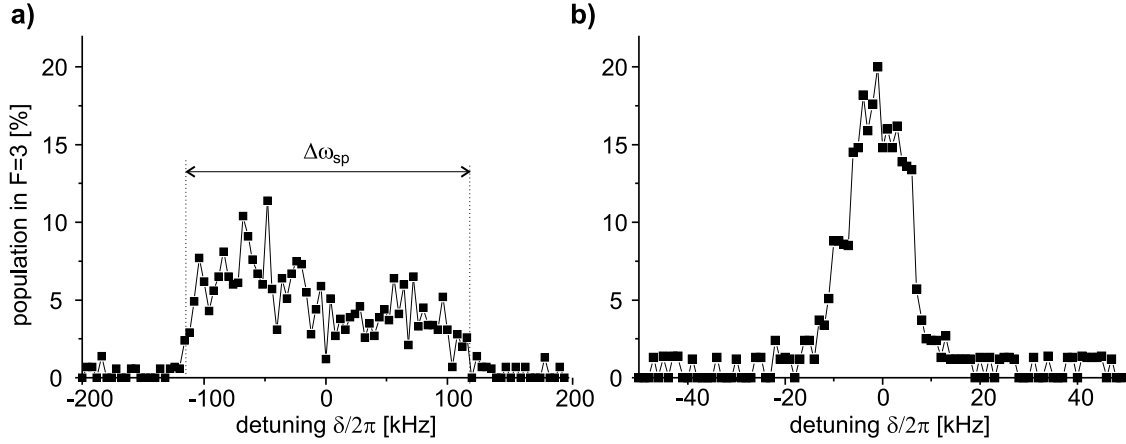
Figure 4.8: Magnetic field compensation using microwave spectroscopy. (a) Result of coarse compensation. The total width of the Zeeman spectrum is $\omega_{\mathrm{sp}}/2\pi = 240$ kHz. (b) Result of fine compensation. The total width is minimized to $\omega_{\mathrm{sp}}/2\pi = 20$ kHz by the fine compensation, corresponding to a field of $B_{\mathrm{res}} = 0.4$ µT.

Fine compensation using microwave spectroscopy

Measuring the Zeeman splitting with microwave spectroscopy is a more precise means to infer the magnitude of magnetic fields. This serves for the fine compensation, since we can minimize the width of the Zeeman spectrum by successively varying the currents of three pairs of coils. The resulting spectra before and after the fine compensation are shown in Figure 4.8. For the spectrum in Figure 4.8(a) we stepped the microwave frequency from $\omega_{\mathrm{hfs}}/2\pi - 200$ kHz to $\omega_{\mathrm{hfs}}/2\pi + 200$ kHz. We used a step size of 2 kHz, equal to the Fourier width of the pulses of $t = 500$ µs duration. A low microwave power ($P = +16$ dBm, $\Omega/2\pi = 1.1$ kHz) was employed to avoid power broadening. After the fine compensation of the magnetic field, we recorded the spectrum in Figure 4.8(b) using $P = -2$ dBm ($\Omega/2\pi = 0.3$ kHz), $t = 3$ ms, with a step size of 0.5 kHz in a frequency interval of $\omega_{\mathrm{hfs}}/2\pi \pm 50$ kHz. For each point in Figure 4.8 we used about $100 - 150$ atoms, yielding errors (not shown) of at most 2%.

From the total width of the spectra, $\Delta\omega_{\mathrm{sp}}$, and the theoretical values of Equation (4.44) one can easily derive the magnitude of the residual field

$$B_{\mathrm{res}} = \frac{\Delta\omega_{\mathrm{sp}}}{2 \times 7\Delta\omega_{m_3 \to m_4}} = \frac{\Delta\omega_{\mathrm{sp}}}{2\pi \times 49.1 \text{ kHz/µT}}. \tag{4.46}$$

After the coarse compensation, we obtain $\Delta\omega_{\mathrm{sp}}/2\pi = 240$ kHz which corresponds to a $B_{\mathrm{res}} = 4.9$ µT ($= 49$ mG). The width of the spectrum could be reduced by one order of magnitude to $\Delta\omega_{\mathrm{sp}}/2\pi = 20$ kHz. This corresponds to a residual field of $B_{\mathrm{res}} = 0.4$ µT (4 mG).
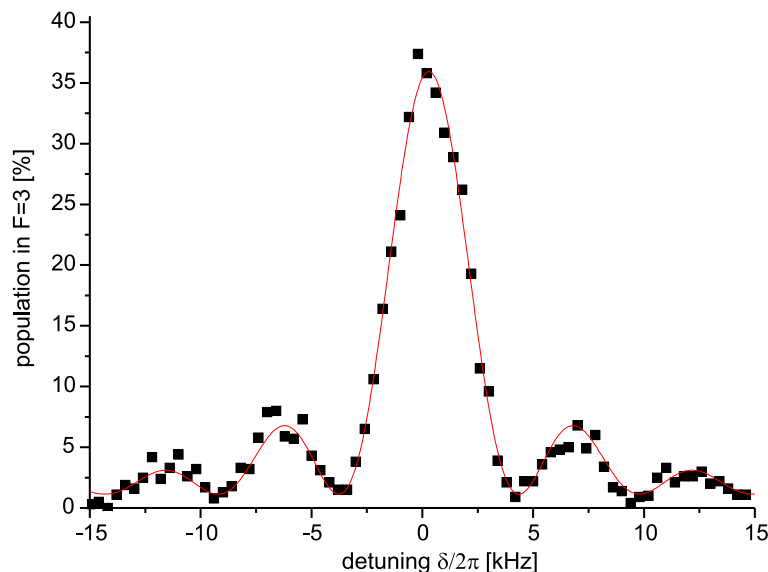
Figure 4.9: Spectrum of a Fourier limited (square) pulse of 200 µs duration. The fit is according to the Rabi formula of Equation (4.47).

Possible limitations

There are many possible reasons for the residual field, one of which for example are fluctuations of the polarization of the dipole trap beams because circular components of the light cause an effective magnetic field. Note that any time-independent circular polarization of the dipole trap laser would be cancelled by the compensation since it is equivalent to a DC magnetic field. We cannot estimate the magnitude of this effect since we have not yet measured the polarization fluctuations.

The broadening of the spectrum could also arise from current fluctuations of the power supply or the existence of time varying magnetic fields, which cannot be compensated for by this method. The measured current fluctuations of the power supplies are < 0.1 mA, yielding shifts of the outermost peaks in the Zeeman spectrum of < 100 Hz. AC magnetic fields at 50 Hz, which arise from transformer coils of the numerous power supplies in the laboratory, were independently measured with a fluxgate magnetometer[2] to be in the order of $\Delta B_{\mathrm{pp}} = 0.13$ µT.

4.4.2 Spectroscopy on the clock transition

After the compensation of the magnetic field it is possible to optically pump the atoms into the $|F = 4, m_F = 0\rangle$ sublevel, and drive the $|F = 4, m_F = 0\rangle \rightarrow |F = 3, m_F = 0\rangle$ clock transition. Figure 4.9 shows the spectrum of a Fourier limited (square) pulse of 200 µs duration. To avoid power broadening, we used a moderate microwave power at the antenna of $P = +24$ dBm (0.25 W). The total span of the frequency scan is ± 15 kHz

---

[2]german: Saturationskern-Sonde, Förstersonde

around the exact resonance frequency $\omega_{\mathrm{hfs}} = 2\pi \times 9.192\,631\,77$ GHz, with a step size of 0.4 kHz. The spectrum was recorded in a trap of $U_0 = (0.09 \pm 0.02)$ mK, and each point is averaged over 10 shots with about 50 atoms each.

The peak shows the typical shape of a Fourier limited pulse. To compare its shape to the theoretical predictions, we used a fit function derived from the Rabi formula of Equation (4.21):

$$P_3(\delta) = C \cdot \frac{\Omega_{\mathrm{R}}^2}{\Omega^2} \sin^2\left(\frac{\Omega t}{2}\right) + D, \quad \text{with} \quad \Omega^2 = (\delta - \delta_{\mathrm{s}})^2 + \Omega_{\mathrm{R}}^2. \tag{4.47}$$

As a fit result, we obtain the following values

pulse duration	t	201 ± 2 µs
Rabi frequency	$\Omega_{\mathrm{R}}/2\pi$	2.85 ± 0.08 kHz
shift of peak position	$\delta_{\mathrm{s}}/2\pi$	294 ± 2 Hz
maximum population transfer	C	36.7 ± 0.9 %
offset	D	1.1 ± 0.2 %

The pulse duration and the Rabi frequency correspond well to the experimental values and previous observations. From Rabi oscillations, such as those presented in the next section, we inferred a maximum Rabi frequency of $\Omega_{\mathrm{R,max}}/2\pi = (9.49 \pm 0.04)$ kHz at $P_{\mathrm{max}} = 35.6$ dBm (3.6 W), thus we expect $\Omega_{\mathrm{R}} = \Omega_{\mathrm{R,max}}\sqrt{P/P_{\mathrm{max}}} = 2\pi \times 2.51$ kHz in this case.

The shift of the peak from the exact atomic resonance is due to contributions of the quadratic Zeeman shift in the applied guiding field of (71 ± 1) µT, of the maximum differential light shift, δ_{ls} (see Section 5.3.2), and of the clock shift δ_{clock} due to collisions.

quadratic Zeeman shift	$\delta_{\mathrm{B}}/2\pi$	217 ± 6 Hz
maximum differential light shift	$\delta_0/2\pi$	-270 ± 54 Hz
clock shift	$\delta_{\mathrm{clock}}/2\pi$	-7.9 ± 2.4 Hz
sum	$\delta_{\mathrm{s}}/2\pi$	-103 ± 55 Hz

The origin of the observed peak shift in this particular spectrum remains unclear at this point and would require a more systematic investigation. Note, that in Chapter 5 all shifts add to zero as expected.

Collisional shift

If more than one atom is trapped in a potential well, a frequency shift due to collisions can occur. This shift, also named "clock-shift", was observed in atomic clocks when operating them with large numbers of atoms. Since its understanding is crucial for the precision of these clocks, it has been extensively studied experimentally and theoretically [87, 88, 89]. Ground state collisions are governed by the short range Van-der-Waals interactions with

the characteristic interaction potential $V(R) = -C_6/R^6$, where R is the interatomic distance. A complete treatment of the elastic collisions is very complicated because the C_6 coefficients depend on the on the F- and m_F-quantum numbers of the colliding atoms. Moreover, the collision shift strongly depends on the temperature of the trapped atoms, since it determines which partial waves dominate the collision process. Thus it is obviously beyond the scope of this thesis to give a full treatment of the collision shifts. However, it is of interest to see if the theoretically predicted shifts (see Appendix A) are observable in our experiment.

It is necessary to approximate the volume of a trapped particle in the three-dimensional potential wells of the dipole trap. The wells are pancake-shaped because their size is given by twice the beam waist $2w_0$ radially and by half the optical wavelength axially. From the potential energy per degree of freedom, $k_B T/2$, we obtain for the oscillation amplitudes in the axial and radial direction, z_0 and r_0,

$$z_0 = \sqrt{\frac{k_B T}{m\Omega_z^2}} \qquad \text{and} \qquad r_0 = \sqrt{\frac{k_B T}{m\Omega_{\text{rad}}^2}}, \tag{4.48}$$

where Ω_z and Ω_{rad} are the axial and radial oscillation frequencies as defined in Equations (2.40a) and (2.40b). The volume, $V = 8r_0^2 z_0$, is assumed as a flat box with edge lengths $2r_0$ and $2z_0$. Using the trap laser wavelength, λ, and the beam waist w_0 the volume can be expressed as:

$$V = \frac{w_0^2 \lambda}{2\pi^3} \left(\frac{k_B T}{2U_0}\right)^{3/2} \tag{4.49}$$

For an atom at a temperature of $T = 0.1$ mK in a trap of $U_0 = 1.0 \pm 0.2$ mK with beam waist, $w_0 = 20$ µm, we obtain $V = (7.7 \pm 2.3) \times 10^{-14}$ cm^3. From Figure A.1 (see Appendix A) we infer for the collision shift at $T = 0.1$ mK, $\kappa = -1.9 \times 10^{-9}$ mHz cm^3/atom. Assuming on average 2 atoms per potential well (which is an upper limit), we obtain a shift of only (-7.9 ± 2.4) Hz, which cannot be observed within our experimental errors.

4.4.3 Rabi oscillations

In order to observe Rabi oscillations, we set the synthesizer to the atomic resonance frequency, measured by recording a frequency spectrum such as the one in Figure 4.9. Since for Ramsey spectroscopy we aim at pulses short compared to all other timescales, we apply the maximum RF power of $P = +36$ dBm ($= 4.0$ W). The trap depth is $U_0 = 1.0$ mK. Again, we optically pump the atoms into the $F = 3, m_F = 0$ sublevel, and drive the $F = 4, m_F = 0 \rightarrow F = 3, m_F = 0$ transition.

Varying the pulse length from 0 µs to 225 µs in steps of 5 µs, leads to the observation of Rabi oscillations (see Figure 4.10). Each point in the graph results from 100 shots with about 60 ± 10 atoms each. The corresponding statistical error is below 1% and is thus not shown in the graph. The error of the data points in Figure 4.10 is dominated
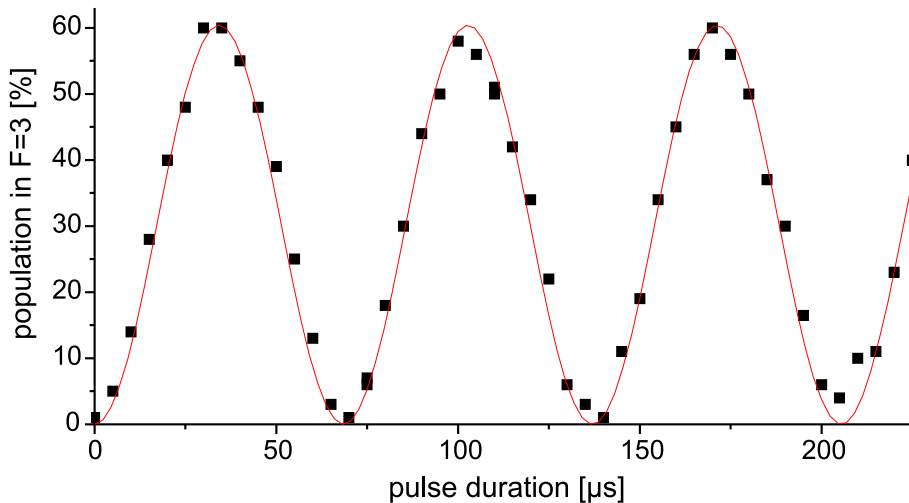
Figure 4.10: Rabi oscillations on the $|F = 4, m_F = 0\rangle \rightarrow |F = 3, m_F = 0\rangle$ clock transition recorded in a trap of depth $U_0 = 1.0$ mK. The line is a fit according to Equation (4.50).

by systematic drifts of the storage probability and efficiencies of the state preparation and detection. The observed Rabi oscillations are solutions of the Bloch equations in the resonant case, $w(t) = -\cos\Omega_R t$, see Equation (4.23). We thus obtain for the population

$$P_3(t) = \frac{C}{2}(1 - \cos\Omega_R t) \tag{4.50}$$

The constant C accounts for imperfections in the preparation and detection of the hyperfine state. Note that we neglected any decay of the Rabi oscillations due to inhomogeneous dephasing effects, which occurs typically within 1 ms. This experiment only serves to determine the Rabi frequency, whereas dephasing effects will be investigated later.

The Rabi oscillations of Figure 4.10 have an excellent fringe visibility. By fitting the data with Equation (4.50) we infer the Rabi frequency $\Omega_R/2\pi = (14.60 \pm 0.02)$ kHz. Note that the Rabi frequency is higher than the one quoted on page 66 because we changed the position of the antenna. The maximum population detected in $F = 3$ of only $C = (60.4 \pm 0.7)\%$ is caused by two effects. First, when we use many (> 40) atoms at a time, up to 20% of the atoms are lost during the transfer from the MOT into the dipole trap due to inelastic collisions, as verified in an independent measurement. The remaining losses arise due to a non-perfect optical pumping process, showing that only 80% of the population is pumped into the $m_F = 0$–state.

4.5 Conclusion and discussion

In this chapter we have demonstrated the possibility of coherently manipulating the ground state hyperfine levels using microwave radiation at 9.2 GHz. The Bloch vector

model served as a theoretical framework, which allowed us to visualize the dynamics of the two-level system. Our experimental techniques permit the manipulation of the internal atomic states at the single atom level. Detection of the hyperfine state at the end of each experimental sequence is accomplished by state-selectively pushing the atoms out of the trap using a resonant laser. This technique discriminates between the hyperfine states with better than 95% efficiency.

Using spectroscopic techniques, we have successfully recorded microwave spectra, which were e. g. used to compensate the earth's magnetic field. We achieved a passive compensation up to 0.4 µT. Finally, we observed Rabi oscillations with excellent fringe visibility and Rabi frequencies of about 10 kHz. This allows us to apply π- and $\pi/2$-pulses, which is an important prerequisite for the implementation of Ramsey spectroscopy, as described in the next chapter.

Chapter 5

Coherence times and quantum state transportation

5.1 Introduction

Information cannot be lost in a closed quantum system since its evolution is unitary and thus reversible. However, a quantum system can never be perfectly isolated from its environment. It is thus to some extent an open quantum system, characterized by the coupling to the environment [90]. This coupling causes decoherence, i. e. the evolution of a pure quantum state into a statistical mixture of states. Decoherence constitutes the boundary between quantum and classical physics [91], as demonstrated in the experiments in Paris and Boulder [92, 93, 94]. There, decoherence was observed as the decay of macroscopic superposition states (Schrödinger cats) to statistical mixtures.

The theoretical and experimental investigation of decoherence has received increased attention in the recent years, especially due to its importance in the field of quantum computing. A possible quantum computer relies on the coherent manipulation of quantum bits (qubits), in which information is encoded in the quantum phases. The coherence time of the quantum states is therefore a crucial parameter to judge the usefulness of a system for storage and manipulation of quantum information. Moreover, long coherence times are of outmost importance for applications in precision spectroscopy such as atomic clocks.

Decoherence of quantum states of trapped particles has recently been studied both with ions [95, 96] and neutral atoms in optical traps [97, 98]. To measure coherence times, Ramsey spectroscopy is a common technique which will also be used here. Our implementation is based on the results of the previous chapter, especially the state preparation and detection, and the observation of Rabi oscillations.

5.2　Classification of decoherence effects

In our experimental realization we observe quantum states in an ensemble average, and decoherence manifests itself in a decay or a dephasing of the macroscopic polarization. It is useful to distinguish between *homogeneous* and *inhomogeneous* effects. Whereas homogeneous dephasing mechanisms affect each atom in the same way, inhomogeneous dephasing only appears when observing an ensemble of many atoms possessing slightly different resonance frequencies. As we will see later, the most important difference between the two mechanisms is the fact that inhomogeneous dephasing can be reversed, in contrast to the irreversible homogeneous dephasing.

Bloch equations with damping - Homogeneous effects

It is straightforward to include the decay rates as damping terms into the Bloch equations. The notation of the different times for population and polarization decay is the same as for nuclear magnetic resonance phenomena or for the optical Bloch equations [78]. Considering the decay due to homogeneous effects, we obtain:

$$
\begin{aligned}
\dot{u} &= \delta v - \frac{u}{T_2{}'} \\
\dot{v} &= -\delta u + \Omega_{\mathrm{R}} w - \frac{v}{T_2{}'} \\
\dot{w} &= -\Omega_{\mathrm{R}} v - \frac{w - w_{\mathrm{st}}}{T_1}.
\end{aligned}
\tag{5.1}
$$

Here, the longitudinal relaxation time, T_1, describes the population decay to a stationary value w_{st}, whereas the transverse relaxation time, $T_2{}'$, is the decay time of the polarization. In the absence of any additional transverse decay mechanism the polarization decays due to the decay of population, $T_2{}' = 2\,T_1$. The factor of 2 arises from squaring, since $T_2{}'$ is the field decay rate, whereas T_1 is the corresponding energy decay rate. In our case, T_1 is governed by the scattering of photons from the dipole trap laser, which couples the two hyperfine ground states via a two-photon Raman transition. Fortunately, this effect is small due to a destructive interference effect, which is discussed in detail in Section 5.4.3. Typical T_1 relaxation times are larger than 1 s. Note that we did not include losses of atoms from the trap in the decay constants, which also occur on timescales of seconds.

The polarization decay time $T_2{}'$ is often governed by mechanisms other than the decay of population. Possible effects for the homogeneous dephasing are intensity fluctuations of the trapping laser, and fluctuating magnetic fields, which both cause a temporal variation of the atomic resonance frequency due to the light shift and Zeeman effect, respectively. Decoherence due to fluctuations prevails if data is obtained by averaging over many realizations of the same experiment. In our case this effect is inevitable because it is impossible to obtain enough information from a single repetition of the experiment.

Inhomogeneous effects

Depending on their environment the atoms may have different resonance frequencies. Thus the Bloch vectors of the individual atoms precess with different velocities and lose their phase relationship, they dephase. The corresponding so-called inhomogeneous decay- or dephasing time is denoted by T_2^*. The Bloch equations for an ensemble of atoms resemble those for the homogeneous case, except for a different transverse relaxation time:

$$
\begin{aligned}
\langle \dot{u} \rangle &= \delta \langle v \rangle - \frac{\langle u \rangle}{T_2} \\
\langle \dot{v} \rangle &= -\delta \langle u \rangle + \Omega_{\mathrm{R}} \langle w \rangle - \frac{\langle v \rangle}{T_2} \\
\langle \dot{w} \rangle &= -\Omega_{\mathrm{R}} \langle v \rangle - \frac{\langle w \rangle - w_{\mathrm{st}}}{T_1},
\end{aligned}
\tag{5.2}
$$

where $\langle \dots \rangle$ denotes the ensemble average. The total inhomogeneous transverse decay time T_2 is given by the polarization decay time T_2' and the reversible dephasing time T_2^*

$$
\frac{1}{T_2} = \frac{1}{T_2'} + \frac{1}{T_2^*}.
\tag{5.3}
$$

In our case, the inhomogeneous dephasing predominantly arises due to the energy distribution of the atoms in the trap. This results in a distribution of light shifts (see Section 5.3.2) because hot and cold atoms experience different average trapping laser intensities.

name	symbol	dominant effects
population decay time (= longitudinal decay time), *irreversible*	T_1	mixing of HFS-states (due to spontaneous Raman scattering from dipole trap laser)
homogeneous dephasing time (= transverse decay time), *irreversible*	T_2'	variations of differential light shift (due to pointing instability of the dipole trap laser)
inhomogeneous dephasing time, *reversible*	T_2^*	distribution of the atomic kinetic energy (causes distribution of the differential light shifts)
total transverse decay time	T_2	$\dfrac{1}{T_2} \equiv \dfrac{1}{T_2'} + \dfrac{1}{T_2^*}$

Table 5.1: Classification of decoherence times.

5.3   Ramsey spectroscopy

Ramsey spectroscopy is an ideal technique to investigate decoherence mechanisms. Being first performed on atomic or molecular beams, it was at that time referred to as the "magnetic resonance method with separate oscillating fields" [99, 100]. The general idea is to use two coherent microwave pulses separated in time, applied at two separate regions of an atomic beam. Since this method is very sensitive to phase shifts between the atomic resonance and the driving field, it became the key technique in the realization of atomic clocks [101, 102]. Ramsey spectroscopy results in the observation of Ramsey fringes, which are a beat signal of the atomic resonance frequency with the driving field. A reduced visibility of the Ramsey fringes is a measure of decoherence, since it occurs if the atoms lose their phase relationship.

5.3.1   Experiment

Illustration in Bloch vector model

The principle of Ramsey spectroscopy is illustrated in the Bloch vector model, as shown in Figure 5.1. It consists of the application of two coherent microwave pulses, separated by a time interval t. Initially, the Bloch vector points downwards, $\boldsymbol{u}_0 = (0, 0, -1)$, which corresponds to an atom prepared in the $F = 4$ state. A $\pi/2$-pulse rotates the Bloch vector around the u-axis into the state $(0, -1, 0)$, where the atom is in a superposition of both hyperfine states. After the pulse has been switched off, the Bloch vector freely precesses in the uv-plane with an angular frequency δ, where $\delta = \omega - \omega_0$ is the detuning of the microwave frequency ω from the atomic resonance ω_0. Note that δ has to be small compared to the Rabi frequency and the spectral pulse width, such that the pulse can be approximated as near resonant, and complete population transfer can occur. After a duration t of free precession, we apply a second $\pi/2$-pulse which rotates the Bloch vector once again around the u-axis. It exchanges the v and the w component of the Bloch vector. The projection of the Bloch vector onto the w axis is inferred by measuring the population in $F = 3$, $P_3 = (w+1)/2$. As a result we see the Ramsey fringes, an oscillation of P_3 as a function of t with frequency δ.
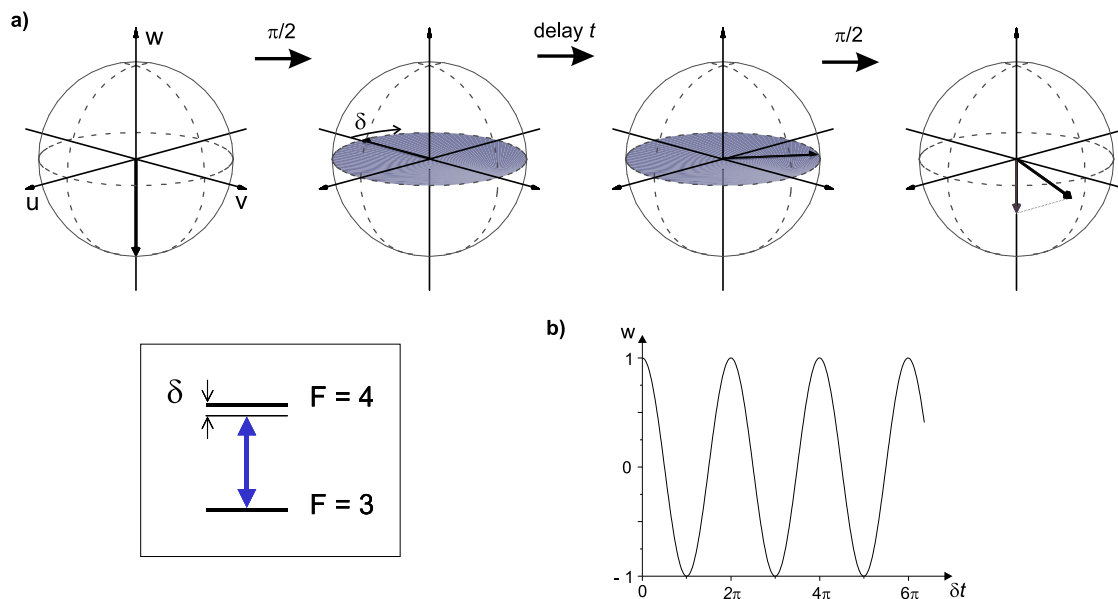
The Ramsey sequence is expressed using the matrix formalism developed in Section 4.2.3,

$$\boldsymbol{u}_{\text{Ramsey}}(t) = \Theta_{\pi/2} \cdot \Phi_{\text{free}}(t) \cdot \Theta_{\pi/2} \cdot \boldsymbol{u}_0, \tag{5.4}$$

where $\Theta_{\pi/2}$ and $\Phi_{\text{free}}(t)$ denote the rotation matrices defined in Equations (4.29) and (4.35), respectively. If the Bloch vector is initially in the state $\boldsymbol{u}_0 = (0, 0, -1)$, we obtain for the w component as a function of time:

$$w_{\text{Ramsey}}(t) = \cos \delta t, \tag{5.5}$$

where we assume δ to be constant.

Figure 5.1: Ramsey spectroscopy. (a) Following a $\pi/2$-pulse, the Bloch vector precesses during a delay time t with angular frequency δ, which is the detuning of the microwave radiation from the atomic resonance. After a second $\pi/2$-pulse we measure the w component of the Bloch vector. (b) Ramsey fringes. The measured w component oscillates with frequency δ as a function of the delay time.

Experimental parameters

For the experimental realization of Ramsey spectroscopy, the setup as well as the techniques of state preparation and detection are identical to those used for the recording of Rabi oscillations (see Section 4.4.3). In order to obtain long coherence times, it is essential to perform the experiments in a lowered dipole trap. We initially transfer the atoms from the MOT into a deeper trap ($U_0 > 1$ mK) to achieve a high transfer efficiency. When the MOT is switched off, we adiabatically lower the trap depth to the appropriate value. To avoid heating due to phase noise of the AOM drivers, we used the non-shifted beams (0th order) of the AOMs to form the dipole trap. To lower the trap, we increase the RF power driving the AOMs and dump the deflected beam.

We again use the $|F = 4, m_F = 0\rangle \rightarrow |F = 3, m_F = 0\rangle$ transition, since it is the most insensitive to magnetic stray fields. From the observed Rabi oscillations (see Figure 4.10, p. 68) we infer $t_{\pi/2} = 16$ µs as the duration of a $\pi/2$-pulse. The detuning of the microwave frequency from the exact atomic resonance is set such that we observe several fringes within the decay time. However, the detuning must be small compared to the Rabi frequency to remain in the limit of resonant pulses.
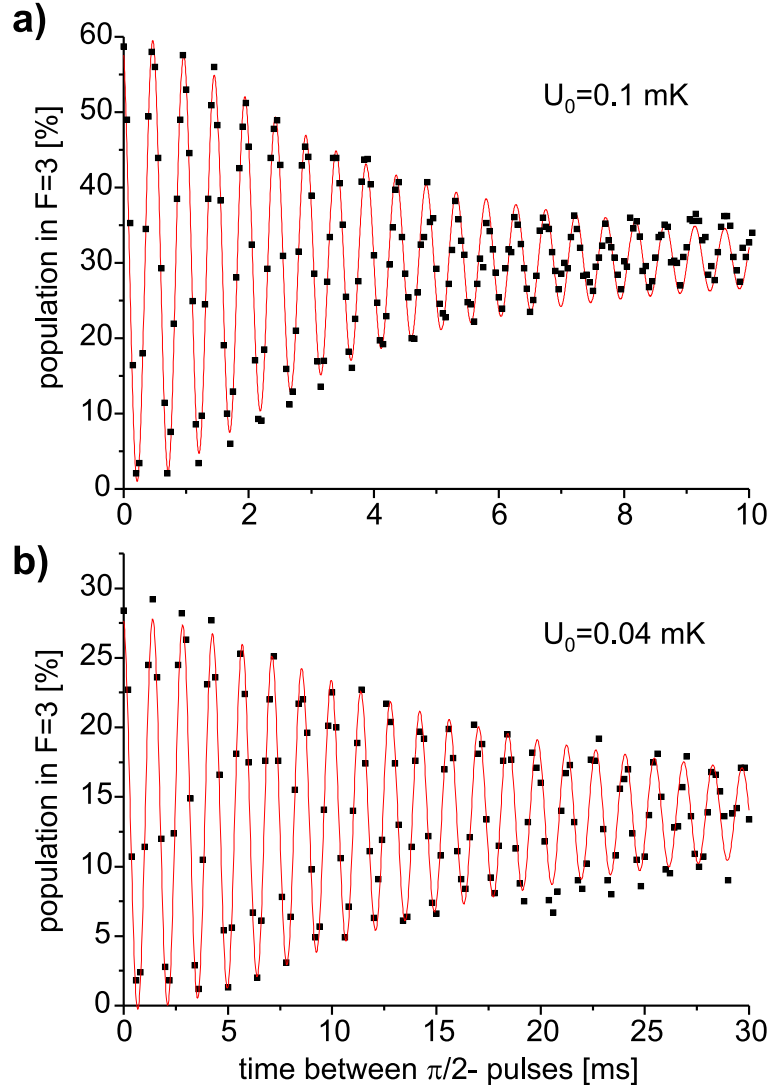
Figure 5.2: Ramsey fringes, recorded for two different trap depths. (a) $U_0 = 0.1$ mK and (b) 0.04 mK. Their decay with time constants $T_2^* = 4.4$ ms and 20.2 ms, respectively, is due to inhomogeneous dephasing caused by the energy distribution in the trap. Each datapoint results from 30 shots with about 50 initial atoms. The line is a fit according to Equation (5.20) (see page 80).

Observations

An experimental observation of Ramsey fringes is presented in Figure 5.2. The two curves were recorded for two different dipole trap depths, $U_0 = 0.1$ mK and 0.04 mK. Each point in the graph corresponds to 30 shots with about 60 trapped atoms per shot, yielding errors (not shown) of less than 1%. The corresponding detunings are listed in Table 5.2, p. 81.
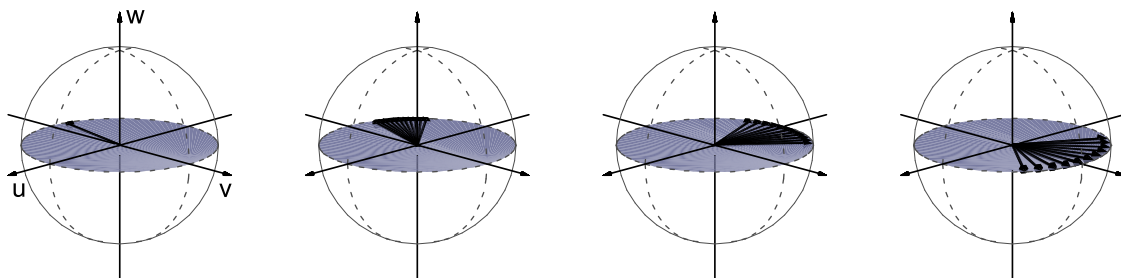
Figure 5.3: Inhomogeneous dephasing. The Bloch vectors precess with different angular frequencies.

The maximum population detected in $F = 3$ is only 60% and 30%, respectively. The reduction to 60% in Figure 5.2(a) is due to imperfections in the optical pumping process and due to losses by inelastic collisions, as discussed in the case of Rabi oscillations. The additional reduction in Figure 5.2(b) occurs during the lowering of the trap to $U_0 = 0.04$ mK, where 50% of the atoms are lost.

5.3.2 Inhomogeneous dephasing

The measured Ramsey fringes show a characteristic decay, which is not exponential. This decay mechanism is due to inhomogeneous dephasing, described by the characteristic decay time, T_2^*. Dephasing occurs because after the first $\pi/2$-pulse, the atomic Bloch vectors precess with different angular frequencies as illustrated in Figure 5.3. Since the precession frequency appears as the oscillation frequency in the Ramsey signal, the observed fringes are an average of many oscillations of slightly different frequencies, which therefore decay. In the following we will see that the dominant effect which causes this frequency spread is the energy distribution of the atoms in the trap leading to a corresponding distribution of light shifts.

It is the goal of this section to analyze this effect in detail by deriving analytic expressions for the Ramsey signal. It will be shown that its envelope is the Fourier transform of the atomic energy distribution, which allows us to infer the temperature of the atoms. Note, that for simplicity all other dephasing mechanisms are neglected here because they govern the decay on longer timescales. The proof of this interpretation is given by the observation of spin echoes in Section 5.4, demonstrating that the dephasing can almost fully be reversed.

Differential light shift

The light shift of the ground state due to the Nd:YAG laser is the trapping potential

$$U_0(\Delta) = \frac{\Gamma}{8} \frac{I}{I_0} \frac{\Gamma}{\Delta} \tag{5.6}$$

The detuning of the Nd:YAG-laser from the D-line of an atom in $F = 4$ is 9.2 GHz less than for an atom in $F = 3$. As a consequence, the $F = 4$ level experiences a slightly stronger light shift, resulting in a shift of the $F = 3 \rightarrow F = 4$ microwave transition towards smaller resonance frequencies. The difference between the frequency shifts of the two ground states is named *differential light shift*. It can be approximated as

$$\hbar\delta_0 = U_0(\Delta_{\text{eff}}) - U_0(\Delta_{\text{eff}} + \Delta_{\text{hfs}}), \tag{5.7}$$

where $\Delta_{\text{eff}} = -1.2 \times 10^7 \, \Gamma$ is the effective detuning of Equation (2.35), and $\Delta_{\text{hfs}} = 2.0 \times 10^3 \, \Gamma$ is the ground state hyperfine splitting. Since $\Delta_{\text{hfs}} \ll \Delta_{\text{eff}}$, we obtain the following expression for the differential light shift, δ_0,

$$\hbar\delta_0 = \frac{\Delta_{\text{hfs}}}{\Delta_{\text{eff}}} U_0. \tag{5.8}$$

Equation (5.8) shows that the differential light shift is proportional to the total light shift U_0 with a scaling factor $\Delta_{\text{hfs}}/\Delta_{\text{eff}} = 1.45 \times 10^{-4}$. For atoms trapped in a potential of $U_0 = 1$ mK, the differential light shift is $\delta_{\text{diff}} = -2\pi \times 3.0$ kHz.

Energy distribution

Until now I have only calculated the differential light shift for an atom at zero temperature, i.e. in the potential minimum, where it experiences the maximum laser intensity. In our case however, the atoms have a finite temperature, so that they have different oscillation amplitudes in the potential. On average, a hot atom sees a lower laser intensity than a cold one and thus experiences a smaller differential light shift, as illustrated in Figure 5.4(a).

We experimentally verified [64] that the energy distribution of the atoms in the dipole trap obeys a three-dimensional Maxwell-Boltzmann distribution with probability density

$$p(E) = \frac{2\sqrt{E}}{(k_{\text{B}}T)^{3/2}\sqrt{\pi}} \exp\left(-\frac{E}{k_{\text{B}}T}\right). \tag{5.9}$$

Here $E = E_{\text{kin}} + U$ is the sum of kinetic and potential energy. In a harmonic trap the virial theorem states that the average potential energy is half the total energy, $U = E/2$. Thus, the differential light shift for an atom of energy E is given by:

$$\delta_{\text{ls}}(E) = \delta_0 + \frac{E}{2\hbar}\frac{\Delta_{\text{hfs}}}{\Delta_{\text{eff}}}, \tag{5.10}$$

where $\delta_0 < 0$ is the maximum differential light shift. For an atom at the bottom of the trap, $E = 0$. As a consequence, the energy distribution $p(E)$ leads, except for a factor and an offset, to an identical distribution $\widetilde{\alpha}(\delta_{\text{ls}})$ of light shifts:

$$\widetilde{\alpha}(\delta_{\text{ls}}) = \frac{2K^{3/2}}{\sqrt{\pi}} \sqrt{\delta_{\text{ls}} - \delta_0} \exp\left[-K(\delta_{\text{ls}} - \delta_0)\right] \quad \text{with} \quad K(T) = \frac{2\hbar}{k_{\text{B}}T}\frac{\Delta_{\text{eff}}}{\Delta_{\text{hfs}}}. \tag{5.11}$$

Note that this distribution only holds in the regime $k_{\text{B}}T \ll U_0$, since the virial theorem was applied for the case of a harmonic potential.
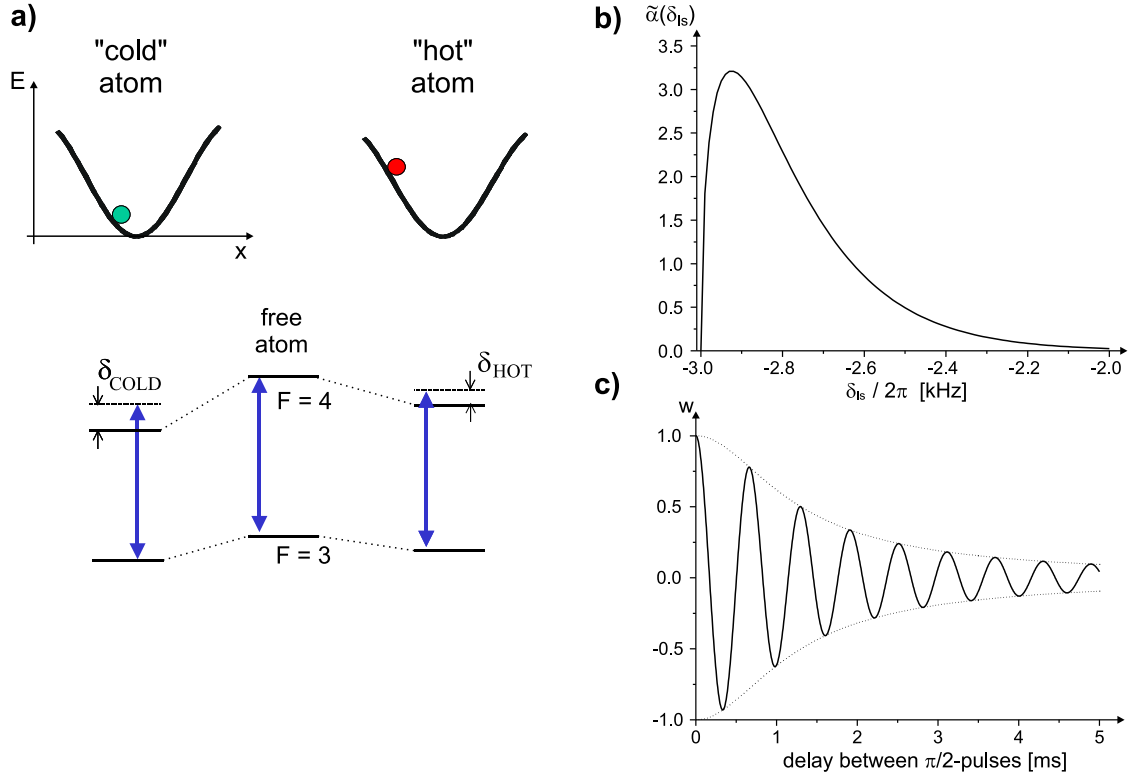
Figure 5.4: Differential light shift. (a) A cold atom experiences a stronger differential light shift than a hot one. (b) Distribution of the differential light shift, $\widetilde{\alpha}(\delta_{\mathrm{ls}})$, for an ensemble of atoms at $T = 100\,\mu\mathrm{K}$ in a trap of $U_0 = 1\,\mathrm{mK}$, according to Equation (5.11). (c) Calculated non-exponential dephasing of a Ramsey signal. The envelope is the fourier transform of $\widetilde{\alpha}(\delta_{\mathrm{ls}})$.

Shape of Ramsey fringes and T_2^* time

In the following I will calculate how this distribution of detunings affects the shape of the Ramsey fringes. Remember that the w component of the Bloch vector without broadening, i.e. without dephasing, is

$$w_{\mathrm{Ramsey}}(t) = \cos\delta t, \tag{5.12}$$

where $\delta = \omega - \omega_0$ is the detuning of the microwave radiation with frequency ω from the atomic resonance ω_0. In general, ω is purposely shifted with respect to the ground state hyperfine splitting, ω_{hfs}, by a small detuning δ_{synth},

$$\omega = \omega_{\mathrm{hfs}} + \delta_{\mathrm{synth}}. \tag{5.13}$$

The atomic resonance frequency ω_0 is modified according to

$$\omega_0 = \omega_{\mathrm{hfs}} + \delta_{\mathrm{ls}} + \delta_{\mathrm{B}} + \delta', \tag{5.14}$$

where δ_{ls} is the energy dependent differential light, δ_{B} is the quadratic Zeeman shift, and δ' summarizes all other unknown frequency shifts. We thus obtain for the detuning

$$\delta = \delta_{\mathrm{synth}} - \delta_{\mathrm{ls}} - \delta_{\mathrm{B}} - \delta'. \tag{5.15}$$

The inhomogeneously broadened Ramsey signal is obtained by averaging over all differential light shifts δ_{ls}:

$$w_{\mathrm{Ramsey,inh}}(t) = \int_{\delta_0}^{\infty} \widetilde{\alpha}(\delta_{\mathrm{ls}}) \, \cos\left[(\delta_{\mathrm{synth}} - \delta_{\mathrm{ls}} - \delta_{\mathrm{B}} - \delta')t\right] d\delta_{\mathrm{ls}}. \tag{5.16}$$

Thus, the shape of the Ramsey fringes is the Fourier(-Cosine)-Transform of the atomic energy distribution. Note that in the integral (5.16) we have set the upper integration limit to "∞", instead of the maximum physically reasonable value, $\delta_0/2$, to guarantee the analytic solution[1]:

$$w_{\mathrm{Ramsey,inh}}(t) = \alpha(t) \, \cos\left[(\delta_{\mathrm{synth}} - \delta_0 - \delta_{\mathrm{B}} - \delta')t + \kappa(t)\right], \tag{5.17}$$

with a time- dependent amplitude $\alpha(t)$ and phase shift $\kappa(t)$:

$$\alpha(t) = \left(1 + \frac{t^2}{K^2}\right)^{-3/4} \qquad \text{and} \qquad \kappa(t) = -\frac{3}{2} \arctan\left(\frac{t}{K}\right). \tag{5.18}$$

This phase shift arises due to the asymmetry of the probability distribution $\widetilde{\alpha}(\delta_{\mathrm{ls}})$. The hot atoms in the tail of the Maxwell-Boltzmann distribution dephase faster than the cold atoms, due to their larger spread. The fact that the hot atoms no longer contribute to the Ramsey signal, results in a shift of the mean δ_{ls} towards larger negative values.

Finally, despite its non-exponential decay, we define the inhomogeneous or reversible dephasing time T_2^* as the $1/e$-time of the amplitude $\alpha(t)$:

$$\alpha(T_2^*) \stackrel{!}{=} e^{-1} \quad \Rightarrow \quad T_2^* = \sqrt{e^{4/3} - 1}\, K = 1.67 \frac{2\hbar}{k_{\mathrm{B}}T} \frac{\Delta_{\mathrm{eff}}}{\Delta_{\mathrm{hfs}}}. \tag{5.19}$$

Thus, the reversible dephasing time T_2^* is inversely proportional to the temperature of the atoms and does not depend on any other parameters.

5.3.3   Discussion

Our detection scheme only allows us to measure the population P_3 in the hyperfine state $F = 3$ (see Section 4.3.3). As a fit function to the experimental data, we thus obtain from Equations (5.17) and (5.19)

$$
\begin{aligned}
P_{3,\mathrm{Ramsey}}(t) &= A \cdot w_{\mathrm{Ramsey,inh}}(t) + B \\
&= A \cdot \left[1 + 2.79 \left(\frac{t}{T_2^*}\right)^2\right]^{-3/4} \cos\left[\delta_{\mathrm{sum}}t + \kappa(t) + \varphi\right] + B. \tag{5.20}
\end{aligned}
$$

---

[1]We have used the following relation:

$$\int_0^{\infty} \tfrac{2}{\sqrt{\pi}} A^{3/2} \sqrt{x}\, e^{(-Ax)} \cos[C(-x + x_0)]\, dx = \left(1 + \tfrac{C^2}{A^2}\right)^{-3/4} \cos\left[Cx_0 - \tfrac{3}{2}\arctan(\tfrac{C}{A})\right]$$

We have introduced the constant A and the offset B to account for the imperfections of state preparation and detection. The only other fit parameters are the sum of all detunings, $\delta_{sum} = \delta_{synth} - \delta_0 - \delta_B - \delta'$, and the decay time T_2^*. A phase offset φ occurs because during the application of the $\pi/2$-pulses, the Bloch vector already starts to precess around the w-axis, while our model assumes that the free precession starts after the application of the second $\pi/2$-pulse.

The corresponding fits are shown in Figure 5.2 (p. 76) and the resulting fit parameters are summarized in Table 5.2. The temperatures, T, have been calculated from T_2^* using Equation (5.19). We can compare them to an independent measurement of the energy distribution in the trap [64]. There, we adiabatically reduced the potential depth and observed whether the atoms are lost. In a trap of depth $U' = 1.3 \pm 0.3$ mK we obtained a temperature of $T' = 80 \pm 20$ µK, with parameters comparable to the present measurement. The temperature can be scaled to our trap depths using the fact that in a harmonic potential, E/Ω is invariant under adiabatic variation of the potential, where E is the sum of potential and kinetic energy and Ω is the oscillation frequency. Since

		Fig. 5.2(a)	Fig. 5.2(b)
Experimental settings			
trap depth	U	0.1 mK	0.04 mK
detuning	$\delta_{synth}/2\pi$	2250 Hz	1050 Hz
Fit results			
fringe amplitude	A	29.7 $\pm$ 0.3 %	14.1 $\pm$ 0.4 %
fringe offset	B	30.5 $\pm$ 0.1 %	13.8 $\pm$ 0.1 %
detuning	$\delta_{sum}/2\pi$	2106.5 $\pm$ 0.8 Hz	716.4 $\pm$ 0.4 Hz
phase offset	φ	0.396 $\pm$ 0.015	0.184 $\pm$ 0.033
dephasing time	T_2^*	4.4 $\pm$ 0.1 ms	20.2 $\pm$ 0.8 ms
Calculated parameters			
temperature (calculated from T_2^*)	T	40.0 $\pm$ 0.9 µK	8.7 $\pm$ 0.3 µK
temperature (calculated from adiabatic lowering [64])	$T(U)$	22 $\pm$ 6 µK	14 $\pm$ 4 µK
phase offset	φ	0.42	0.14
quadratic Zeeman shift	$\delta_B/2\pi$	412 $\pm$ 13 Hz	412 $\pm$ 13 Hz
max. diff. light shift	$\delta_0/2\pi$	-300 $\pm$ 60 Hz	-120 $\pm$ 24 Hz
remaining detuning ($\delta' = \delta_{synth} - \delta_0 - \delta_B - \delta_{sum}$)	$\delta'/2\pi$	32 $\pm$ 61 Hz	42 $\pm$ 27 Hz

Table 5.2: Parameters extracted from the Ramsey fringes of Figure 5.2.

$\Omega \propto \sqrt{U}$, we can infer the temperature for other trap depths, $T(U) = T'\sqrt{U/U'}$. For the case of our data the corresponding temperatures are $T(0.1 \text{ mK}) = 22 \pm 6 \text{ μK}$, and $T(0.04 \text{ mK}) = 14 \pm 4 \text{ μK}$, where we have included a 20% error of our trap depths.

For the case of $U_0 = 0.1$ mK, we indeed expect a higher temperature than $T(U)$ since, in contrast to the reference measurement [64], we optically pumped the atoms within the dipole trap, which heated them. In the case of $U_0 = 0.04$ mK, the obtained temperatures do not match because the approximations of a harmonic trap and of $k_B T \ll U_0$, which were used for the derivation of $\widetilde{\alpha}_{ls}$ (see Equation (5.11)), are no longer valid. First, the virial theorem can no longer be applied due to the anharmonicity, since the atoms spend more time at the top of the potential, which results in a relation $\delta_{ls}(E)$ different from Equation (5.10). Second, since we have lost the hottest atoms, $\widetilde{\alpha}_{ls}$ is cut off at higher energies.

It is also interesting to see if the fitted detuning δ_{sum} corresponds to the experimental settings. All known shifts are inserted into the above table. The quadratic Zeeman shift in the externally applied guiding field of $B = 97.9 \pm 1.5 \text{ μT}$ is $\delta_B/2\pi = 412 \pm 13$ Hz, where the error is due to the uncertainty of the calibration. We also calculate the expected maximum differential light shifts, δ_0, from the trap depth U_0 which is known with an estimated uncertainty of 20%. We can thus calculate the remaining detuning $\delta' = \delta_{synth} - \delta_0 - \delta_B - \delta_{sum}$. In the absence of any other shifts, δ' should add to zero, which is approximately the case here. The discrepancy might arise due to a misalignment of the dipole trap, which could further reduce δ_0. According to the treatment in Section 4.4.2, the collision shift is too small to be observable and is neglected here.

The phase offset φ occurs because the Bloch vector precesses around the w-axis even during the application of the two $\pi/2$-pulses, resulting in $\varphi = 2\, t_{\pi/2}\, \delta_{sum}$. For our parameters, we obtain $\varphi = 0.42$ for the case of $U_0 = 0.1$ mK and $\varphi = 0.14$ for $U_0 = 0.04$ mK, which matches the observed values reasonably well.

5.4 Spin echo

In the following section we will see that the dephasing can be reversed, since each atom approximately keeps its own resonance frequency, as long as its energy in the trap is not changed. In order to rephase the magnetic dipole moments, we use a spin echo technique, i.e. we apply an additional π-pulse between the two Ramsey $\pi/2$-pulses. Being first invented by E. Hahn in 1950 for nuclear magnetic resonance [103], this technique was also recently employed in optical dipole traps [104], independently of this work.
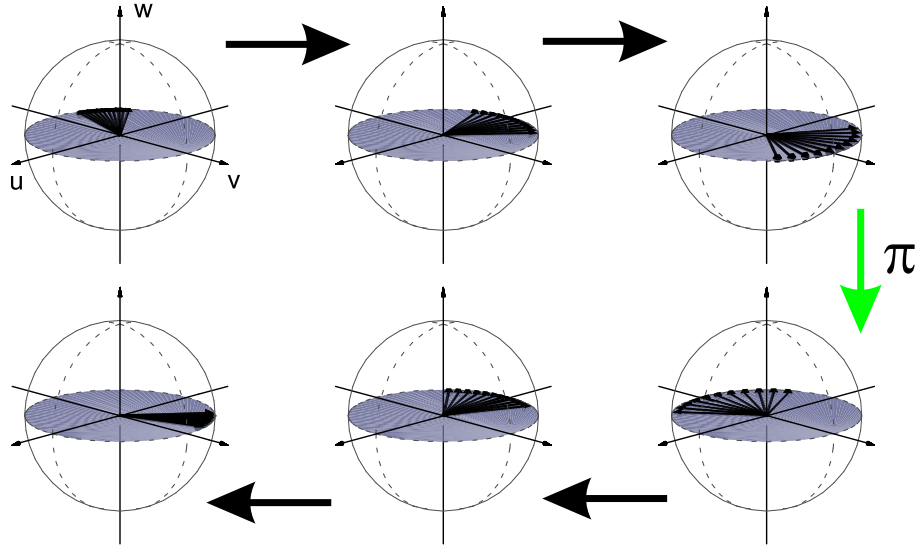
Figure 5.5: Spin echo. A π-pulse between the two Ramsey pulses leads to a rephasing of the Bloch vectors.

5.4.1 Experiment

Illustration in Bloch vector model

The effect of the π pulse is visualized in Figure 5.5. After the first $\pi/2$-pulse at $t = 0$, all Bloch vectors start at $\boldsymbol{u}(0) = (0, -1, 0)$. As discussed in the case of Ramsey spectroscopy, they dephase due to their thermal distribution of resonance frequencies. Now, a π-pulse, applied at time $t = \tau_\pi$, rotates the ensemble of Bloch vectors around the u axis by 180°. The following temporal evolution reverses the initial dephasing such that at $t = 2\tau_\pi$, the Bloch vectors are completely rephased in the state $\boldsymbol{u}(2\tau_\pi) = (0, 1, 0)$.

Similarly to the Ramsey sequence, we describe the evolution of the Bloch vector by the established matrix formalism,

$$\boldsymbol{u}_{\text{echo}}(t) = \Theta_{\pi/2} \cdot \Phi_{\text{free}}(t - \tau_\pi) \cdot \Theta_\pi \cdot \Phi_{\text{free}}(\tau_\pi) \cdot \Theta_{\pi/2} \cdot \boldsymbol{u}_0, \tag{5.21}$$

where $\Theta_{\pi/2}$, Θ_π and Φ_{free} denote the rotation matrices defined in equations (4.29), (4.32) and (4.35), respectively, and $\boldsymbol{u}_0 = (0, 0, -1)$ is the initial state of the Bloch vector. Here, τ_π is the time between $\pi/2$- and π-pulse, and $t > \tau_\pi$ is the time of the second $\pi/2$ pulse. As a result of Equation (5.21), the w component of the Bloch vector in the absence of inhomogeneous broadening is given by

$$w_{\text{echo}}(t) = -\cos \delta(t - 2\tau_\pi), \tag{5.22}$$

where δ is the detuning of the microwave from the atomic resonance. We obtain the shape of the inhomogeneously broadened echo signal, $w_{\text{echo,inh}}(t)$, by integrating over all
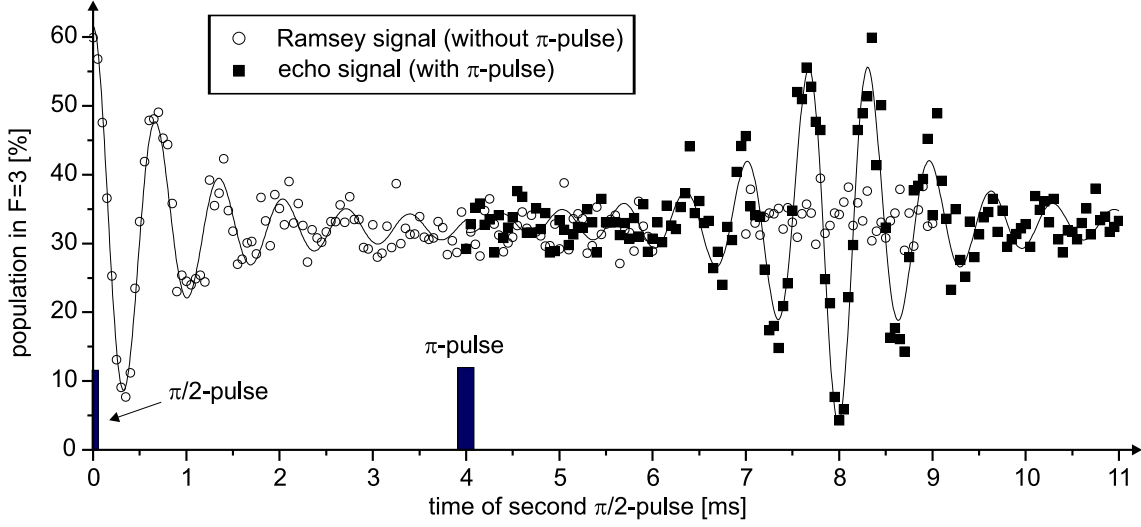
Figure 5.6: Experimental observation of a spin echo in a trap of $U_0 = 1.0$ mK. The application of a π-pulse at $t = 4$ ms leads to a rephasing of the magnetic dipole moments around $t = 8$ ms (squares). The open circles show a Ramsey signal, obtained without a π-pulse, but with otherwise identical parameters. Each point results from 30 shots with about 50 atoms each. The lines are fits according to Equations (5.20) and (5.25).

differential light shifts δ_{ls}

$$w_{\mathrm{echo,inh}}(t) = \int_{\delta_0}^{\infty} -\widetilde{\alpha}(\delta_{\mathrm{ls}}) \, \cos\left[(\delta_{\mathrm{synth}} - \delta_{\mathrm{ls}} - -\delta_{\mathrm{B}} - \delta')(t - 2\tau_\pi)\right] d\delta_{\mathrm{ls}}, \qquad (5.23)$$

where we have replaced δ by a sum of different detunings (see Equation (5.15)). The integration leads to the known result of the previous section,

$$w_{\mathrm{echo,inh}}(t) = -\alpha(t - 2\tau_\pi) \cos\left[(\delta_{\mathrm{synth}} - \delta_0 - \delta_{\mathrm{B}} - \delta')(t - 2\tau_\pi) + \kappa(t - 2\tau_\pi)\right], \qquad (5.24)$$

with amplitude $\alpha(t)$ and phase shift $\kappa(t)$ as defined in Equation (5.18). The shape of the echo signal is obviously the same as for the Ramsey fringes, apart from the global minus sign. Equation (5.24) shows that the maximum of the amplitude of the echo signal is at $t = 2\tau_\pi$. Note that in this treatment an irreversible dephasing is not yet included, i.e. $T_1 = \infty$ and $T_2' = \infty$. Possible mechanisms leading to a decay of the maximum amplitude of the echo signal will be analyzed later in this section.

Observations

A typical spin echo signal is presented in Figure 5.6, recorded in a trap of $U_0 = 1.0$ mK. The π-pulse, applied at $\tau_\pi = 4$ ms, leads to a spin echo that appears symmetrically around $2\tau_\pi = 8$ ms, as expected. For comparison, we recorded a Ramsey signal, without a π-pulse, but with otherwise identical parameters. As expected, the amplitude of the
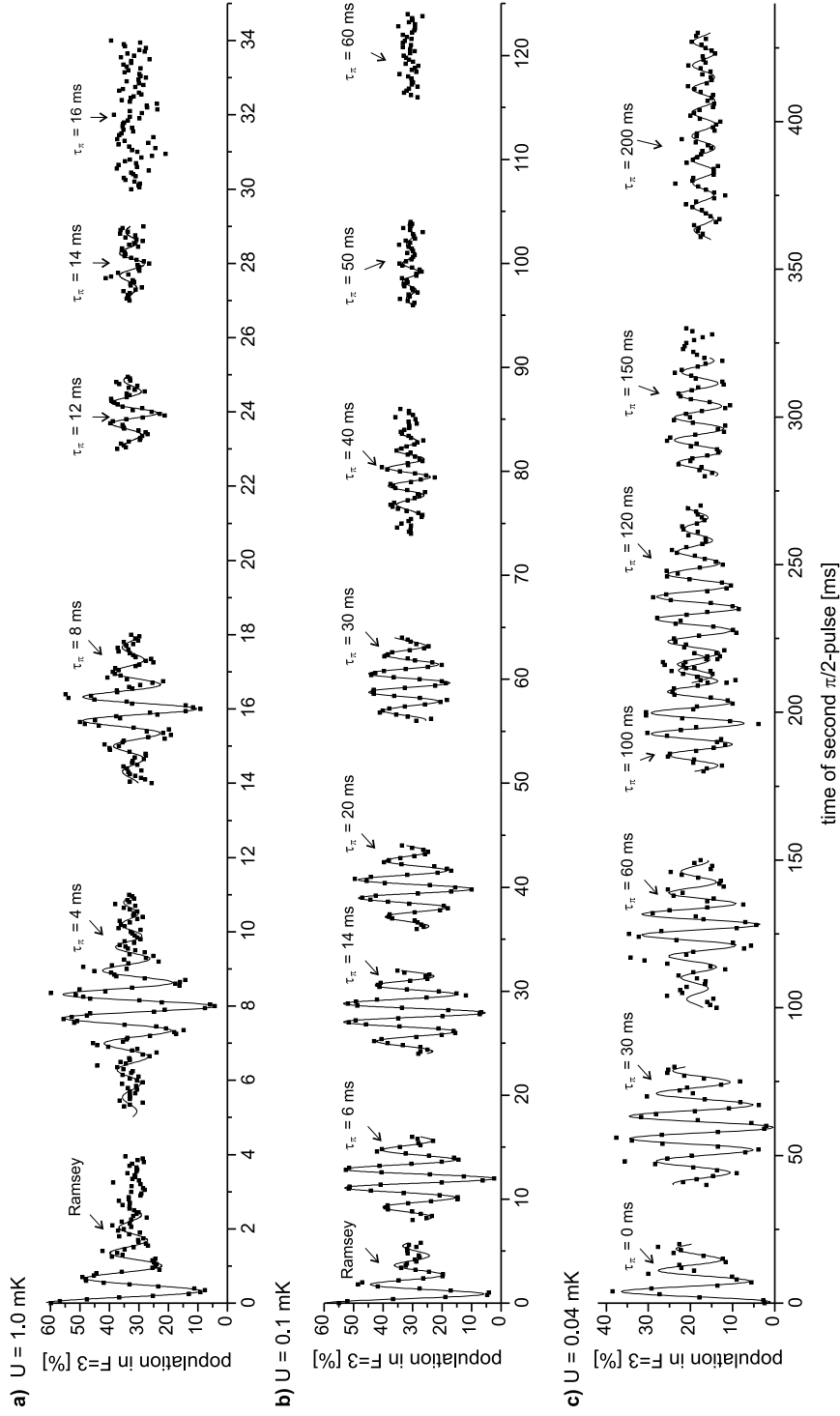
Figure 5.7: Spin echoes. Shown are spin echoes recorded for three different trap depths, (a) $U_0 = 1.0$ mK, (b) 0.1 mK and (c) 0.04 mK. We observe a decrease of the maximum spin echo amplitude with increasing time of the π-pulse, with longer decay times in lower trap depths. All spin echoes are fitted using Equation (5.25), and the resulting fringe visibilities are plotted in Figure 5.8. In (a) and (b), the first curve is a Ramsey signal, recorded with otherwise identical parameters.

		Fig. 5.8(a)	Fig. 5.8(b)	Fig. 5.8(c)
Exp. settings				
trap depth	U	1.0 mK	0.1 mK	0.04 mK
detuning	$\delta_{\text{synth}}/2\pi$	-1630 Hz	550 Hz	450 Hz
Fit results				
reversible deph. time	T_2^*	0.86 ± 0.05 ms	2.9 ± 0.1 ms	18.9 ± 1.7 ms
mean detuning	$\delta_{\text{sum}}/2\pi$	1494 ± 72 Hz	548 ± 11 Hz	130 ± 4 Hz
Calc. parameters				
temperature	T	205 ± 12 µK	61 ± 2 µK	9.8 ± 1.7 µK
quadratic Zeeman shift	$\delta_{\text{B}}/2\pi$	412 ± 13 Hz	412 ± 13 Hz	412 ± 13 Hz
max. diff. light shift $(\delta_0 = \delta_{\text{synth}} - \delta_{\text{B}} - \delta_{\text{sum}})$	$\delta_0/2\pi$	-3536 ± 73 Hz	-410 ± 17 Hz	-92 ± 14 Hz

Table 5.3: Parameters of the spin echoes of Figure 5.7.

Ramsey signal has completely decayed at the position of the spin echo.

To model the experimental data, we use a fit function which is similar to $P_{3,\text{Ramsey}}(t)$ of Equation (5.20) except for the shift by $2\tau_\pi$ and the minus sign:

$$
\begin{aligned}
P_{3,\text{echo}}(t) &= A \cdot w_{\text{echo,inh}}(t) + B \\
&= -A \left[1 + 2.79 \left(\frac{t - 2\tau_\pi}{T_2^*} \right)^2 \right]^{-3/4} \cos\left[\delta_{\text{sum}}(t - 2\tau_\pi) + \kappa(t - 2\tau_\pi) + \varphi \right] + B. \ (5.25)
\end{aligned}
$$

with constants A and B for amplitude and offset. The corresponding fit is shown as a line in Figure 5.6. The fact that for Ramsey and spin echo signals the mechanisms of dephasing and rephasing are the same, leads to, within experimental errors, identical reversible decay constants, $T_{2,\text{Ramsey}}^* = 0.98 \pm 0.09$ ms and $T_{2,\text{echo}}^* = 0.86 \pm 0.08$ ms. In the experimental data we also see the effect of the minus sign in front of Equation (5.25) resulting in a minimum of $P_{3,\text{echo}}$ at $t = 2\tau_\pi$. The minimum occurs because the Bloch vectors rephase in $\boldsymbol{u} = (0,1,0)$ which is projected onto $\boldsymbol{u} = (0,0,-1)$, i.e. $F = 4$, by the second $\pi/2$-pulse. The excellent agreement of this model with the experimental data is also apparent in the spin echo signals recorded for the demonstration of "quantum state transportation" (see Section 5.5), where we used better statistics.

We recorded numerous echo signals for three different trap depths, $U_0 = 1.0$ mK, 0.1 mK and 0.04 mK (see Figure 5.7). We observe that the visibility of the echo signals decreases with increasing waiting time τ_π. A slower decrease of the visibility is obtained in lower traps. For $U_0 = 0.04$ mK, we even observed oscillations around $t = 400$ ms. For a systematic analysis, we first fitted the function of Equation (5.25) to all recorded spin

echoes. The resulting fit parameters, T_2^* and δ_{sum}, averaged over the respective datasets, are shown in Table 5.3. From the amplitude, A, and offset, B, of each signal we calculate the visibility V of the spin echoes according to

$$V = \frac{B - A}{B + A}. \tag{5.26}$$

The resulting visibility as a function of the time of the π-pulse is presented in Figure 5.8.

5.4.2 Irreversible or homogeneous dephasing

The decay of the spin echo visibility (see Figures 5.7 and 5.8) is caused by irreversible dephasing mechanisms, which can again be treated analytically. We denote the corresponding irreversible or homogeneous decay time by $T_2{}'$, as defined in the beginning of this chapter. The population decay time, T_1, can be neglected in our case. It is governed by the scattering of photons from the dipole trap laser, which couples the two hyperfine ground states via a two-photon Raman transition. This effect is suppressed due to a destructive interference effect [41, 105] causing a relaxation on a timescale of 10 s (see Section 5.4.3). As a consequence, the various decay/dephasing mechanisms can be treated independently because of their different time scales ($T_2^* \ll T_2{}' \ll T_1$).

So far, I considered the detuning as constant during the experimental sequence. A time-varying detuning, $\delta(t)$, may result in a variation of the precession angle of the Bloch vector. This precession angle in a time interval from t_1 to t_2 is expressed as the time integral of the detuning:

$$\phi(t_1, t_2) = \int_{t_1}^{t_2} \delta(t')dt'. \tag{5.27}$$

If the accumulated phases before and after the π-pulse are not equal, $\phi(0, \tau_\pi) \neq \phi(\tau_\pi, 2\tau_\pi)$, the fringes of the spin echo signal are shifted. These phase fluctuations, i.e. fluctuations of the detuning, arise e.g. due to changes of the differential light shift, caused by intensity fluctuations or pointing instabilities, or due to magnetic field fluctuations.

The phase difference $\phi(\tau_\pi, 2\tau_\pi) - \phi(0, \tau_\pi)$ is expressed as a difference of the detuning, $\Delta\delta$, averaged over τ_π. We aim to calculate the Bloch vector at $t = 2\tau_\pi$, when the inhomogeneous dephasing has been fully reversed. The corresponding matrix equation (5.21) for the Bloch vector then reads:

$$\boldsymbol{u}_{\text{echo}}(\Delta\delta, 2\tau_\pi) = \Theta_{\pi/2} \cdot \Phi_{\text{free}}(\delta + \Delta\delta, \tau_\pi) \cdot \Theta_\pi \cdot \Phi_{\text{free}}(\delta, \tau_\pi) \cdot \Theta_{\pi/2} \cdot \boldsymbol{u}_0, \tag{5.28}$$

which results in

$$w_{\text{echo}}(\Delta\delta, 2\tau_\pi) = -\cos(\Delta\delta\,\tau_\pi). \tag{5.29}$$

Note that in the following considerations, we assume that all atoms experience almost the same fluctuation $\Delta\delta$, regardless of their energy in the trap, i.e. we consider a *homogeneous* broadening effect. We obtain the experimental signal from many repetitions of the
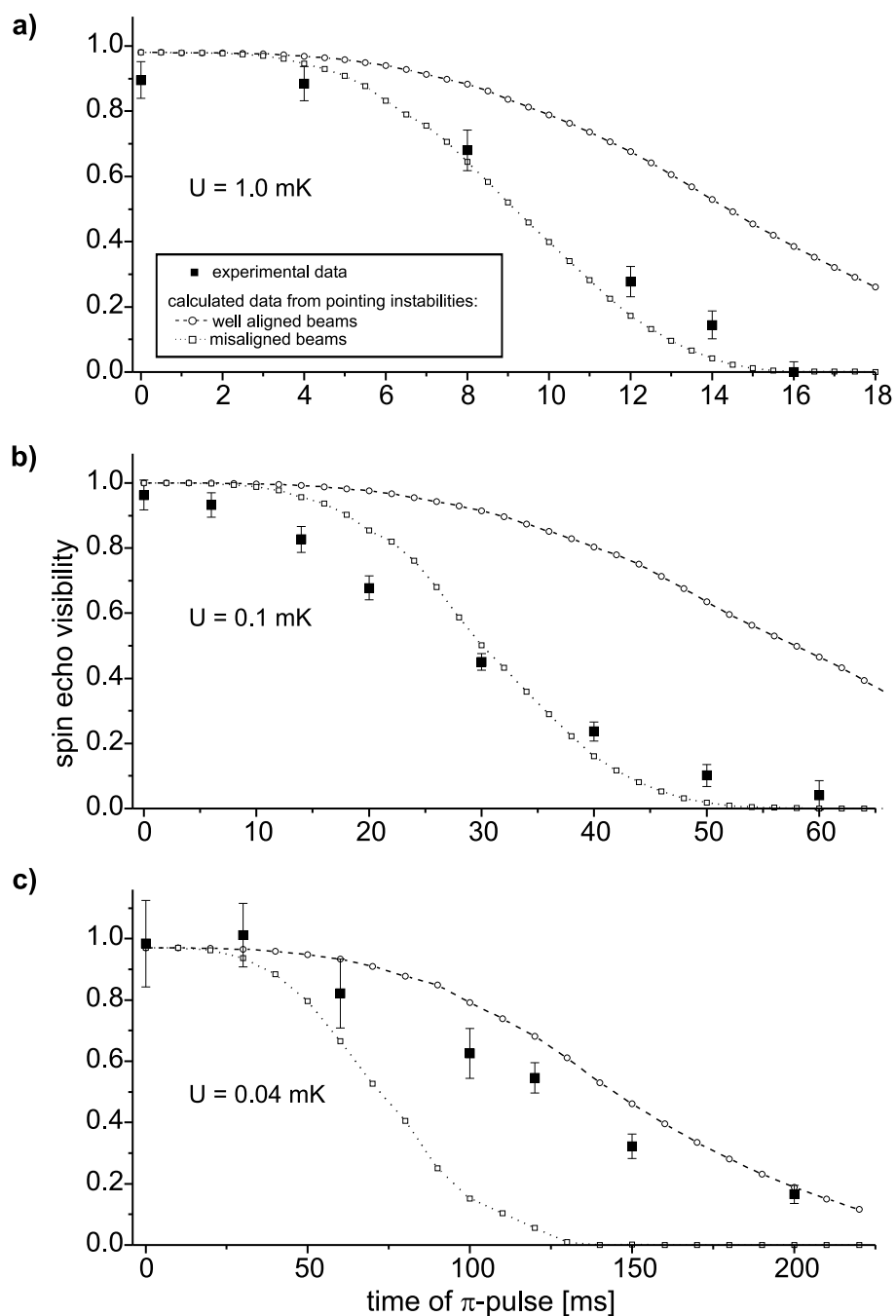
Figure 5.8: Decay of the spin echo visibility, extracted from the signals of Figure 5.7. Shown are the contributions of the dephasing due to the pointing instability of the trapping laser for the case of well aligned and of misaligned beams.

same experiment by integrating Equation (5.29) over all fluctuation amplitudes obeying a probability distribution $p(\Delta\delta, \tau_\pi)$, which depends on the averaging time τ_π:

$$w_{\text{echo,hom}}(2\tau_\pi) = \int_{-\infty}^{\infty} - \cos(\Delta\delta\,\tau_\pi)\, p(\Delta\delta, \tau_\pi)\, d\Delta\delta. \qquad (5.30)$$

Thus, the decay of the maximum amplitude of the spin echo signal is given by the Fourier-(Cosine-)transform of the distribution of fluctuations. $p(\Delta\delta, \tau)$ is assumed to be a Gaussian probability distribution,

$$p(\Delta\delta, \tau_\pi) = \frac{1}{\sigma(\tau_\pi)\sqrt{2\pi}}\, e^{-\frac{(\Delta\delta)^2}{2\sigma(\tau_\pi)^2}}, \qquad (5.31)$$

with mean $\overline{\Delta\delta} = 0$ and variance $\sigma(\tau)^2$, where the fluctuation amplitude $\sigma(\tau)$ is measured in Hz. Inserting Equation (5.31) into (5.30) and performing the integration yields

$$w_{\text{echo,hom}}(2\tau_\pi) = e^{-\frac{1}{2}\tau_\pi^2 \sigma(\tau_\pi)^2}. \qquad (5.32)$$

Therefore we obtain the visibility, V, of the echo signal in dependence of τ_π:

$$V(\tau_\pi) = C_0\, e^{-\frac{1}{2}\tau_\pi^2\, \sigma(\tau_\pi)^2}. \qquad (5.33)$$

5.4.3 Analysis of dephasing mechanisms

In the following section I will present an analysis of the possible dephasing mechanisms, most of which can be characterized by a fluctuation amplitude $\sigma(\tau)$. I will study the effects of intensity fluctuations and pointing instabilities of the dipole trap, fluctuating magnetic fields, elastic collisions, heating, fluctuations of the microwave power and the pulse duration, and spin relaxation due to spontaneous Raman scattering from the dipole trap laser.
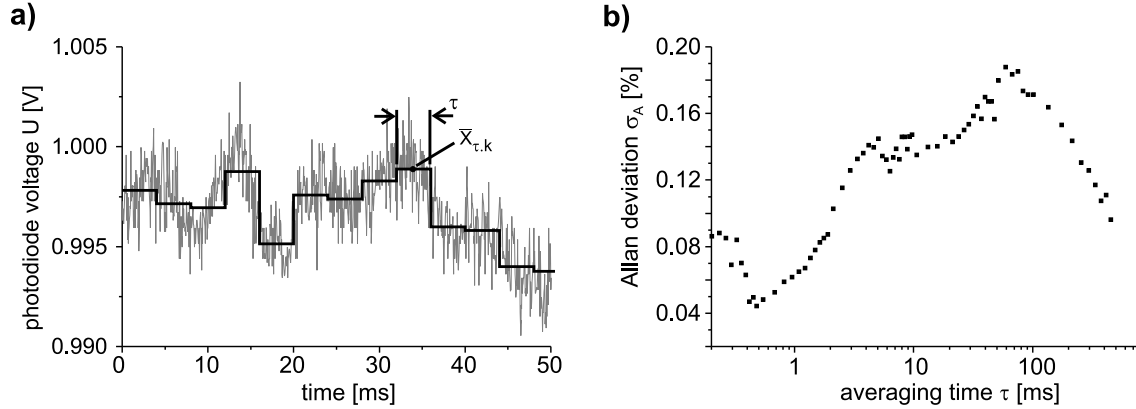
Intensity fluctuations

A mechanism which may cause a time-varying detuning are intensity fluctuations of the trapping laser. They can easily be measured by shining the laser onto a photodiode and recording the resulting voltage as a function of time.

The variance $\sigma(\tau)^2$ depends on the "integration time", τ, of the fluctuations, i.e. on the time between the $\pi/2$ pulses and the π pulse. For this reason, an ideal tool for the analysis is the *Allan variance*, defined as [106]:

$$\sigma_{\text{A}}^2(\tau) = \frac{1}{m} \sum_{k=1}^{m} \frac{(\overline{x}_{\tau,k+1} - \overline{x}_{\tau,k})^2}{2}. \qquad (5.34)$$

Here $\overline{x}_{\tau,k}$ denotes the average of the photodiode voltages over the k-th time interval τ (see Figure 5.9(a)), normalized to the mean voltage of the entire dataset. The resulting Allan

Figure 5.9: Measurement of the intensity fluctuations using the Allan deviation. (a) Output power of the Nd:YAG laser. (b) Corresponding Allan deviation, according to Equation (5.34).

deviation σ_A is a dimensionless number which expresses the relative fluctuations. They directly translate into fluctuations $\sigma(\tau)$ of the detuning,

$$\sigma(\tau) = \sqrt{2}\,\delta_0\sigma_A(\tau), \tag{5.35}$$

where the factor of $\sqrt{2}$ arises because σ_A only measures one half of the mean square of the difference of successive averages. The maximum differential light shift δ_0 is calculated from the spin echoes (see Table 5.3).

The experimental data yield relative fluctuations of the intensity of $\sigma_A(\tau) < 0.2\%$ (see Figure 5.9(a)). We evaluated the Allan deviation at $\tau = T_2'$, which is the relevant time scale here. However, the resulting detuning fluctuations, summarized in Table 5.5 (p. 95), are too weak to account for the observed decay of the spin echo visibility.

Pointing instability of the dipole trap laser

We found that pointing instabilities of the trapping laser beams cause variations of the trap depth, which are one order of magnitude greater than the variations caused by intensity fluctuations. Any change of the relative position of the two interfering laser beams also changes the interference contrast, and thus the light intensity experienced by the atoms. These position shifts can arise due to shifts of the laser beam itself, due to variations of the optical paths e. g. from acoustic vibrations of the mirrors or from air flows.

In order to measure the pointing instabilities we mutually detune the two dipole trap beams by $\Delta\nu = 10$ MHz using the AOMs and overlap them on a fast photodiode (see Figure 5.10(a)). The amplitude of the resulting beat signal directly measures the interference contrast of the two beams and is thus proportional to the depth of the potential wells of the standing wave dipole trap. We used a network analyzer (HP 3589A) operated in "zero span" mode to record the temporal variation of the beat signal amplitude within
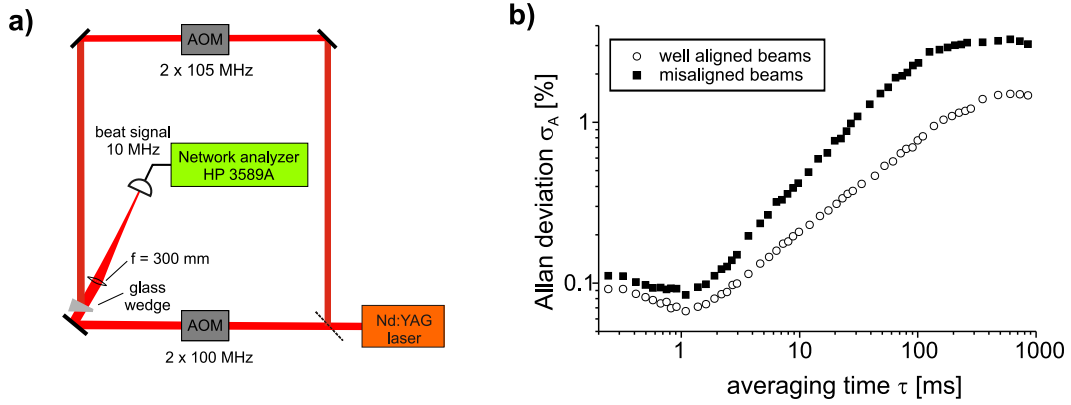
Figure 5.10: Measuring the pointing instability. (a) The dipole trap beams having a frequency difference of $\Delta\nu = 10$ MHz are overlapped on a fast photodiode. (b) Allan deviation of the amplitude of the resulting beat signal.

a filter bandwidth of 10 kHz.

The resulting Allan deviation of the beat signal amplitudes is shown in Figure 5.10(b). The lower curve shows the signal in the case of well overlapped beams, whereas for the upper curve, we purposely misaligned the beams so that the beat signal amplitude is reduced by a factor of 2 (-6 dB). In the latter case variations of the relative beam position cause a larger variation of the beat signal amplitude, since the beams overlap on the slopes of the Gaussian profile.

These two curves measure the best and the worst cases of the fluctuations. We found that the relative fluctuations for long time scales of $t > 100$ ms reach up to 3% in the worst case. The frequency fluctuations $\sigma(\tau)$ are again calculated using Equation (5.35), which result in a spin echo visibility:

$$V(\tau) = e^{-\delta_0^2 \sigma_A^2 \tau^2}. \tag{5.36}$$

The result is plotted together with the observed visibility in Figure 5.8 and the $\sigma(T_2')$ are shown in Table 5.5 (p. 95). We found that the effect of pointing instability is indeed in the range of the observed detuning fluctuations.

Fluctuating magnetic fields

In addition to the intensity fluctuations, magnetic field fluctuations could also lead to a dephasing. Using a fluxgate magnetometer we measured magnetic fields of $\Delta B_{pp} = 0.13$ µT, dominated by components at $\nu = 50$ Hz. The resulting frequency shift on the clock transition is:

$$\Delta\omega = 2\,\Delta\omega_{0\to0}\,B_0\,\Delta B_{pp}, \tag{5.37}$$

where $B_0 = 97.9$ µT is the offset field and $\Delta\omega_{0\to0}/2\pi = 43$ mHz/(µT)^2 is the quadratic Zeeman shift. For our case, we obtain $\Delta\omega = 1.1$ Hz.

The effect of the magnetic fluctuations also depends on the time interval between the microwave pulses. If this time is large compared to $1/\nu$, all fluctuations cancel except for those of the last oscillation period. As a consequence, the effect on the detuning fluctuations σ also decreases. We calculate this effect by computing the Allan variance $\sigma_A(\tau)$ of a 50 Hz sine signal. The resulting detuning fluctuations then read $\sigma(\tau) = \sqrt{2}\,\Delta\omega\,\sigma_A(\tau)$, which are again evaluated at $\tau = T_2'$. The resulting $\sigma(T_2')$, shown in Table 5.5, are too small to account for the decay of the spin echo amplitude.

Elastic collisions

Elastic ground state collisions could also lead to a dephasing, which should be reversible in our case, and which would thus leave the spin echo amplitude unaffected. The collision itself is a coherent process, whose effect depends on the density of the atoms. When the average time between the collision events is much smaller than the time between the microwave pulses, the collisions result in a frequency shift, δ_{coll}. In our case of about 60 atoms distributed over about 40 potential wells, the probability of having more than two atoms in the same well is very small. We therefore have potential wells containing either one or two atoms, thus two classes of atoms whose resonance frequencies differ by δ_{coll}. Since the number of atoms in the potential wells does not change, the effect of the frequency shift should be completely reversed by the π-pulse.

Note that the collisional shift is much smaller than all other frequency shifts (see also Section 4.4.2), such that its effect cannot be observed in our experiment. From the trap depth U_0 and the temperature T (see Table 5.3) we calculate the trap volume (see Equation (4.49)) and infer the corresponding collision shift from the curves in Appendix A. Assuming a 20% uncertainty in the trap depths, we obtain the following values:

trap depth	U_0	1.0 mK	0.1 mK	0.04 mK
trap volume	$V/10^{-13}$	2.3 ± 0.7 cm^3	11.5 ± 3.5 cm^3	13.2 ± 4.0 cm^3
collision shift	$\delta_{coll}/2\pi$	-2.6 $\pm$ 0.8 Hz	-1.1 $\pm$ 0.3 Hz	-1.2 $\pm$ 0.4 Hz

Table 5.4: Trap volumes and collisional shifts.

Note that at $U_0 = 0.04$ mK we assumed $3/2 k_B T = U_0$, since we already lost 50% of the trapped atoms. The remaining atoms do not thermalize, and thus their energy distribution no longer obeys the Maxwell-Boltzmann statistics. In any case, collisions do not play a role at $U_0 = 0.04$ mK, since the probability of having two or more atoms in one potential well is very small.

Heating effects

Heating of the atoms can also cause a variation of the resonance frequency within the microwave pulse sequence. Since a complete qualitative treatment would require numerical simulations, I will only give an order-of-magnitude estimation of the expected effects here,

regardless of the exact distribution of the energy in the trap. An energy gain of ΔE will lead to a change of the differential light shift, which directly yields the detuning fluctuations $\sigma = \delta_{ls}(E + \Delta E) - \delta_{ls}(E)$. Using the definition of δ_{ls} of Equation (5.10), we obtain:

$$\sigma = \frac{\Delta E}{2\hbar} \frac{\Delta_{hfs}}{\Delta_{eff}}. \tag{5.38}$$

Heating effects in our trap have been investigated and classified in [64]. It was found that in the case of this experiment the dominant heating effect is given by intensity fluctuations, which cause a heating rate of $\langle \dot{E} \rangle = 6 \times 10^{-2}$ mK/s in a trap of depth 1.3 mK. This value has to be scaled to our trap depths and multiplied by the average time between the microwave pulses. Again, we use T_2' as a typical timescale. With

$$\Delta E = T_2' \langle \dot{E} \rangle \tag{5.39}$$

we obtain detuning fluctuations which are more than one order of magnitude too small to account for the observed fluctuation amplitudes (see Table 5.5).

Fluctuation of microwave power and pulse duration

Another possible dephasing effect are fluctuations of the microwave power and the pulse duration. The application of two $\pi/2$-pulses and one π-pulses results in $w_{echo}(2\tau_\pi) = -1$. Any fluctuations of the amplitude $(\Delta\Omega_R/\Omega_R)$ or pulse duration $(\Delta t/t)$ result in fluctuations of the amplitude of the spin echo signal, i. e. $w_{echo}(2\tau_\pi) = -\cos\Delta\phi$ according to:

$$\left(\frac{\Delta\phi}{2\pi}\right)^2 = \left(\frac{\Delta\Omega_R}{\Omega_R}\right)^2 + \left(\frac{\Delta t}{t}\right)^2 \tag{5.40}$$

With $\Delta t/t < 10^{-3}$ (measured) and $\Delta\Omega_R/\Omega_R < 10^{-2}$ (specifications of the synthesizer) we obtain $\Delta\phi/2\pi < 10^{-2}$, which is too small to be observed. Moreover, this effect neither depends on the dipole trap power nor on the time between the microwave pulses.

However, the time intervals between the microwave pulses would be affected by a clock inaccuracy of the D/A-board of the computer control system. The specified accuracy $\Delta\tau/\tau = 10^{-4}$, results in a phase fluctuation $\delta_{sum}\tau_\pi \Delta\tau/\tau < 0.01$ for all parameters δ_{sum} and τ_π used in our experiment. Thus, the fluctuations of microwave power and pulse duration do not account for the observed reduction of the spin echo visibility.

Spin relaxation due to light scattering

Population relaxation of the two ground states, characterized by the decay time T_1, is caused by scattering of photons from the dipole trap laser. However, for the case of far detuning, atoms coherently scatter photons and mostly decay back to the same hyperfine state. This is due to a destructive interference of the transition amplitudes for state-changing Raman scattering processes, which results in a spin relaxation rate much longer than the spontaneous scattering rate. This effect was first observed on

optically trapped Rubidium atoms in the group of D. Heinzen [105] and was also verified in experiments in our group [41].

The corresponding transition rate is calculated by means of the Kramers-Heisenberg formula [107], which is a result from second order perturbation theory. We obtain for the rate of spontaneous transitions, $\Gamma_{\mathrm{F,m} \to \mathrm{F''},m''}$, from the ground state $|F,m\rangle$ to the ground state $|F'',m''\rangle$:

$$\Gamma_{\mathrm{F,m} \to \mathrm{F''},m''} = \frac{3c^2\omega_{\mathrm{L}}^3 I}{4\hbar\, d^4} \left| \frac{a^{(1/2)}_{\mathrm{F,m} \to \mathrm{F''},m''}}{\Delta_{1/2}} + \frac{a^{(3/2)}_{\mathrm{F,m} \to \mathrm{F''},m''}}{\Delta_{3/2}} \right|^2, \tag{5.41}$$

where $\Delta_{\mathrm{J'}} = \omega_{\mathrm{L}} - \omega_{\mathrm{J'}}$ is the detuning of the dipole trap laser from the $^6P_{\mathrm{J'}}$-state and $d = \langle 4,4\,|\,\mu_{+1}\,|\,5,5\rangle$ (for numbers see Appendix A). The transition amplitudes $a^{(\mathrm{J'})}$ are obtained by summing over all possible intermediate states $|F',m'\rangle$ of the relevant $^6P_{\mathrm{J'}}$ manifold:

$$a^{(\mathrm{J'})}_{\mathrm{F,m} \to \mathrm{F''},m''} = \frac{\Gamma_{\mathrm{J'}}}{\omega_{\mathrm{J'}}^3} \sum_{q,F',m'} \langle F'',m''\,|\,\mu_{\mathrm{q}}\,|\,F',m'\rangle \langle F',m'\,|\,\mu_0\,|\,F,m\rangle. \tag{5.42}$$

Here, the matrix element $\langle F',m'\,|\,\mu_0\,|\,F,m\rangle$ describes the coupling by the π-polarized ($q=0$) dipole trap laser, whereas $\langle F'',m''\,|\,\mu_{\mathrm{q}}\,|\,F',m'\rangle$ describes the spontaneous decay, where we have to sum over all possible polarizations, $q = -1,0,1$. $\Gamma_{\mathrm{J'}}$ are the linewidths of the excited states.

For Rayleigh scattering processes, which do not change the hyperfine state ($F,M = F'',M''$), the amplitudes add up, $a^{(3/2)} = 2a^{(1/2)}$. However, for state changing Raman processes ($F,M \neq F'',M''$), the two transition amplitudes are equal but have opposite sign, $a^{(3/2)} = -a^{(1/2)}$. Then the two terms in Equation (5.41) almost cancel in the case of far detuning, ($\Delta_{1/2} \approx \Delta_{3/2}$). As a result the spontaneous Raman scattering rate scales as $1/\Delta^4$ whereas the Rayleigh scattering rate scales as $1/\Delta^2$. The suppression factor can be expressed using the fine structure splitting $\Delta_{\mathrm{fs}} = \Delta_{3/2} - \Delta_{1/2}$ as

$$\Gamma_{\mathrm{Raman}} = \beta\,\Gamma_{\mathrm{Rayleigh}} \qquad \text{with} \quad \beta = \left| \frac{\Delta_{\mathrm{fs}}}{3\Delta_{1/2}} \right|^2. \tag{5.43}$$

For the case of cesium, we obtain a suppression factor of $\beta = 0.011$. The Rayleigh scattering rate for an atom trapped in a potential of $U_0 = 1.0$ mK is $\Gamma_{\mathrm{Rayleigh}} = 11$ s^{-1}. Then, the corresponding spontaneous Raman scattering rate is 0.12 s^{-1}. Note that for the above calculations we have assumed equally populated m_F-levels, which results in a population decay time of $T_1 = 8.6$ s in a trap of depth 1.0 mK. Since in most of our experiments, the trap depth is significantly lower, T_1 will be even larger. As a consequence, we neglect the population decay due to spontaneous scattering.

The experiments performed in the group of D. Heinzen [105] and in our group [41] were only sensitive to changes of the hyperfine F-state, since the atoms were in a mixture of m_F-sublevels. However, the theoretical treatment above predicts similarly long relaxation times for any particular m_F-sublevel.

5.4.4 Discussion

In the above analysis we have investigated various dephasing mechanisms and character-ized them by the corresponding amplitude of the detuning fluctuations, $\sigma(\tau)$. We have found that the fluctuations of the trap depth and thus the differential light shift due to the pointing instability of the dipole trap lasers is the dominant irreversible dephasing mechanism. The resulting theoretical curves agree with the experimentally observed decay of the spin echo visibility (see Figure 5.8). All other dephasing mechanisms are too small to account for the observed dephasing.

We have summarized in Table 5.5 the contributions of the dephasing mechanisms. For comparison with the experimental values, we fit the spin echo visibility of Figure 5.8 with a Gaussian,

$$V(\tau_\pi) = e^{-\frac{1}{2}\tau_\pi^2\sigma_{\mathrm{exp}}^2}, \tag{5.44}$$

with a time-independent detuning fluctuation σ_{exp}. In correspondence to the definition of T_2^*, we define the homogeneous dephasing time T_2' when the visibility of the spin echo has decayed to $1/e$, despite its non-exponential decay:

$$V(T_2') = C_0 e^{-1} \quad \Rightarrow \quad T_2' = \frac{\sqrt{2}}{\sigma}. \tag{5.45}$$

In Table 5.5, all time-dependent detuning fluctuations are evaluated at T_2', which is the

trap depth	U_0	1.0 mK	0.1 mK	0.04 mK
observed fluctuation amplitude (fit with a Gaussian)	$\dfrac{\sigma_{\mathrm{exp}}}{2\pi}$	22.0 ± 0.9 Hz	6.6 ± 0.2 Hz	1.54 ± 0.07 Hz
irreversible dephasing time	T_2'	10.2 ± 0.4 ms	33.9 ± 1.0 ms	146.2 ± 6.6 ms
intensity fluctuations	$\dfrac{\sigma(T_2')}{2\pi}$	5.9 Hz	0.67 Hz	0.17 Hz
pointing instability (well aligned beams)	$\dfrac{\sigma(T_2')}{2\pi}$	10.6 Hz	2.4 Hz	1.3 Hz
pointing instability (misaligned beams)	$\dfrac{\sigma(T_2')}{2\pi}$	21.6 Hz	6.7 Hz	3.7 Hz
magnetic field fluctuations	$\dfrac{\sigma(T_2')}{2\pi}$	1.7 Hz	0.35 Hz	0.17 Hz
heating	$\dfrac{\sigma(T_2')}{2\pi}$	0.7 Hz	0.2 Hz	0.08 Hz

Table 5.5: Summary of dephasing mechanisms.

relevant timescale.

The following table shows a summary of the relevant decay times. Their different timescales justify the assumption $T_2^* \ll T_2' \ll T_1$, made at the beginning of this chapter.

trap depth	U_0	1.0 mK	0.1 mK	0.04 mK
reversible dephasing time	T_2^*	0.86 ± 0.05 ms	2.9 ± 0.1 ms	18.9 ± 1.7 ms
irreversible dephasing time	T_2'	10.2 ± 0.4 ms	33.9 ± 1.0 ms	146.2 ± 6.6 ms
population relaxation time	T_1	8.6 s	86 s	220 s

Table 5.6: Overview of relaxation times.

5.5 Quantum state transportation

The control of both position and internal states of the atom opens the route to the realization of more complex experiments, such as the transport of two atoms into a high finesse resonator. There, they interact via the exchange of a photon, with the goal of entangling two particles or to operate a quantum gate. In all these experiments, state preparation and detection will take place outside the cavity. Therefore, it is of great importance to investigate if coherent superposition states can be maintained during transportation of the atoms.

Comparable experiments have already been performed with ions, which were successfully transported between distinct locations while maintaining internal-state coherence [108]. Using neutral atoms, controlled coherent transport and splitting of atomic wave packets in spin-dependent optical lattice potentials have recently been demonstrated [109].

5.5.1 Experiment

Our experiment is essentially the spin echo measurement of the previous section, with the addition that the atoms are transported between the microwave pulses. The sequence is visualized in Figure 5.11. After the $\pi/2$-pulse the atom is displaced by 1 mm before the π-pulse is applied. Then, the atom is transported back to its initial position, where we apply the second $\pi/2$-pulse.

We set the dipole trap parameters such that we obtain long coherence times along with high transportation efficiencies. As in the previous experiments, we transfer the atoms from the MOT into a deep trap ($U_0 = 1.3$ mK) before we adiabatically lower it to $U_0 = 0.1$ mK. The atoms were transported over a distance of 1 mm within 2 ms, resulting in an acceleration of $a = 1.0 \times 10^3$ m/s^2.
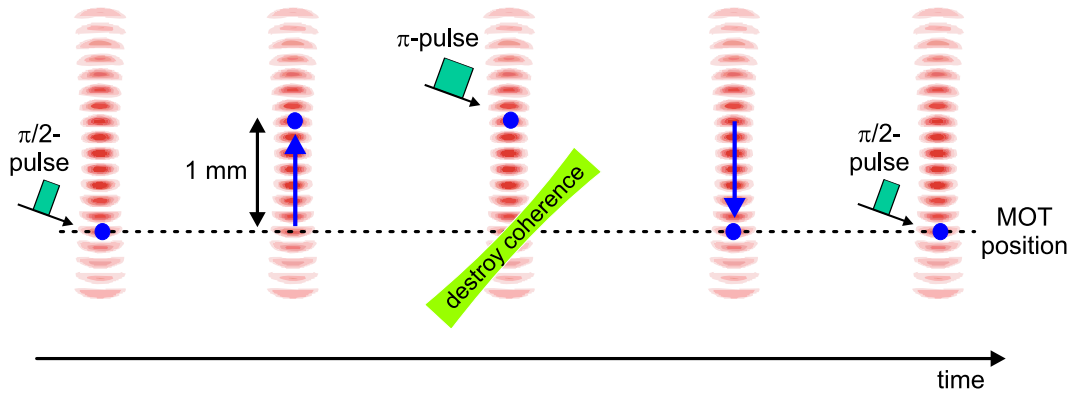
Figure 5.11: Quantum state transportation. An atom prepared in a superposition of hyperfine states is displaced by 1 mm. Synchronously to the π-pulse, we shine in an off-resonant state mixing laser into the initial position. After transporting the atom back to its initial position, the state superposition is analyzed by means of a second $\pi/2$-pulse.

In order to make sure that any coherence is destroyed if the atom is not transported, we shine in an off-resonant "state mixing laser" into the initial position simultaneously with the π-pulse. The parameters of the state mixing laser are chosen such that it incoherently mixes the two hyperfine states with an equilibrium of nearly 50% of the population in each of the levels. The scattering rate is chosen to be sufficiently high to just mix the hyperfine states but at the same time to minimize the influence on the transported atoms. We employ a beam with a power of 500 µW, focused to a waist of < 50 µm, which is one order of magnitude smaller than the transportation distance of 1 mm. Due to the large detuning of $\Delta = +30$ GHz, we obtain a scattering rate of 2 photons/ms which is almost independent of the hyperfine state. The beam is switched on for a period of 3 ms.

5.5.2 Results

To prove the coherent transport, we recorded spin echoes with and without transportation between the microwave pulses. In Figure 5.12(a) we show a spin echo obtained without transportation and without application of the mixing laser as a reference signal. The spin echo is still there if we transport the atom between the microwave pulses, however with slightly reduced visibility (see Figure 5.12(b)). Here, we have also illuminated the position of the MOT with the mixing laser after the atoms have been transported away. To demonstrate the effect of the mixing laser, we repeated the same experiment without transportation. As expected, the coherence is completely destroyed, resulting in the disappearance of the spin echo (see Figure 5.12(c)).

Decay of the spin echo visibility

We measured the visibility of the spin echo as a function of the time of the π-pulse, with and without transportation. We find that the visibility decays faster when we transport
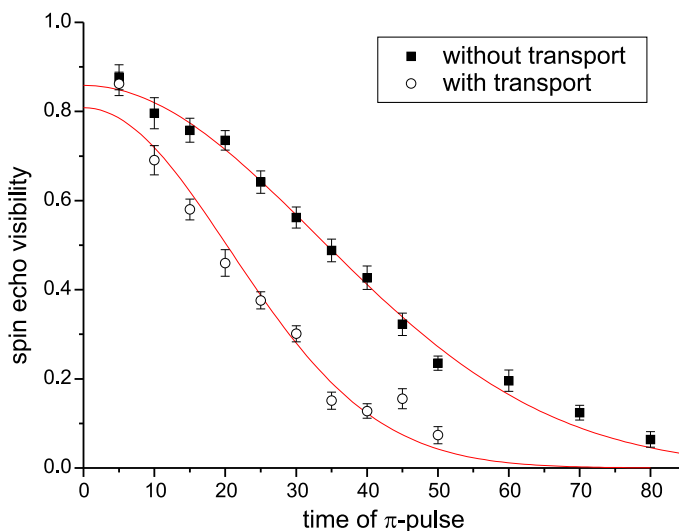
the atom between the microwave pulses (see Figure 5.13). For a quantitative analysis, we again fit the Gaussian of Equation (5.44), which yield the following values:

		without transport	with transport
detuning fluctuation	$\sigma/2\pi$	4.8 ± 0.1 Hz	7.7 ± 0.2 Hz
irreversible dephasing time	T_2'	46.9 ± 1.0 ms	29.2 ± 0.8 ms

Note, that we have assumed the detuning fluctuations σ to be time-independent. The obtained values of σ are in good agreement with those of the previous section. Thus, the decay of the spin echo visibility without transportation is also governed by the pointing
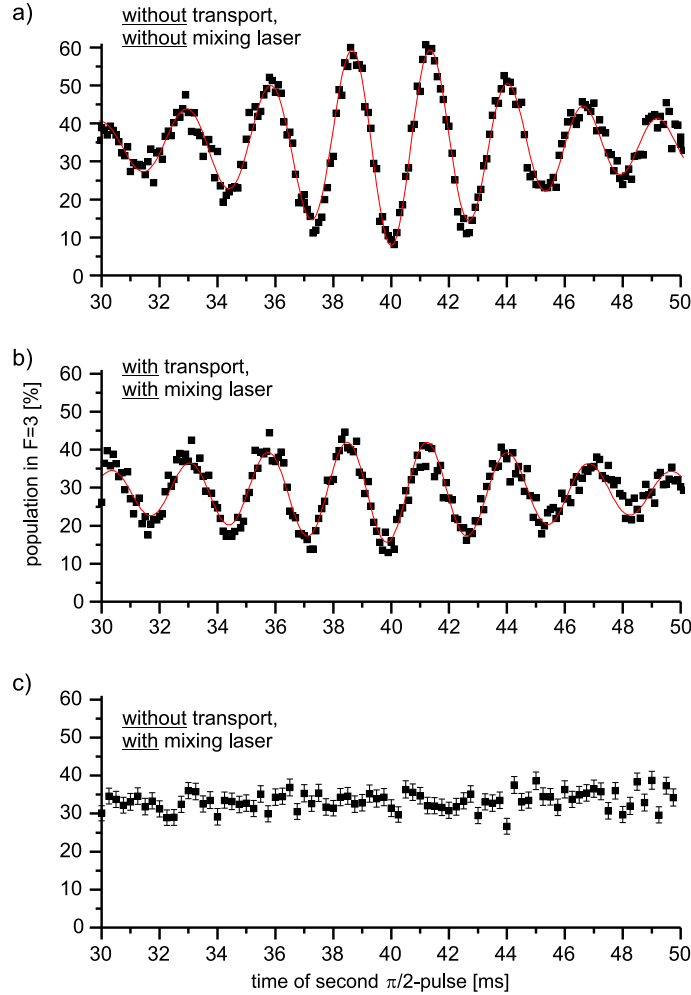
Figure 5.12: Spin echo with and without transport, according to the scheme in Figure 5.11. (a) without transportation, without mixing laser; (b) Atoms are transported by 1 mm, with mixing laser applied at $z = 0$ mm; (c) same but without transportation. The lines in (a) and (b) are fits according to Equation (5.25).

Figure 5.13: Visibility of the spin echo with and without transportation between the microwave pulses. The lines are fits according to Equation (5.44). The faster decay of the visibility is caused by heating of the atoms during the transportation procedure.

instabilities of the trapping laser. The spin echo visibility of the transported atoms shows a faster decay, however. Thus, we observe a new dephasing mechanism, other than those discussed in the previous section, which will be discussed in the following. We estimate the reduction of the spin echo amplitude by two heating effects, first due to the abrupt acceleration of the potential, and second due to the reflections of the trapping laser beam off the glass cell.

The heating effect due to abrupt acceleration has been discussed in detail in Section 3.4.1. For each of the two transports of the atom, the acceleration is first abruptly changed from 0 to a, from a to $-a$ after half the transportation distance, and back to 0 at the end. We thus have to deal with 6 changes of the acceleration, each of which may increase the energy of the atom. In our case, $a = 0.03\,a_0$, with $a_0 = 3.7 \times 10^4$ m/s^2.

To calculate the heating effect due to abrupt acceleration, we assume an initial energy of $E = 0.3\,U_0$, calculated from the T_2^*-times of the signals of Figure 5.12. The numerical calculations reveal that the maximum energy gain caused by the 6 changes of the acceleration amounts to $\Delta E = 0.15\,U_0 = 150$ µK. This would cause a maximum change of the fluctuation of $\sigma = 22$ Hz. Note that this value overestimates the real effect, since our calculation holds for the worst case of 6 changes of the acceleration with maximum energy gain. But it demonstrates that the abrupt acceleration may cause a change of the average detuning, large enough to account for the observed faster decay of the spin echo visibility. The existence of a heating effect is supported by the measurement of a survival probability with transportation of 70%, compared to 80% without transportation.

The second heating effect causes parametric and resonant heating of the atoms due to the reflections from the dipole trap laser off the glass cell and can be neglected, as will be shown in the following. This effect, discussed in detail in [64, 76], was observed in Section 3.4.1, where we found a decreased transportation efficiency for certain accelerations (see Figure 3.9, p. 39). Heating due to the reflections of the dipole trap laser occurs when the detuning of the laser beams matches the axial vibration frequency $\Omega_z = 2\pi \times 75$ kHz. The resulting heating rate is $\langle \dot{E} \rangle = 0.5\,\beta\,\Omega_z\,E$, with $\beta = 0.0067$ in our case. It yields $\langle \dot{E} \rangle = 47$ mK/s for $E = 0.3\,U_0$. The time interval, $\Delta t = 1/\sqrt{\dot{\Omega}}$ during which the resonance condition is fulfilled was calculated using the uncertainty relation $\Delta\Omega\,\Delta t = 1$ and $\Delta\Omega = \dot{\Omega}\,\Delta t$, where $\Delta\Omega$ is the width of the resonance. In our case we mutually detuned the laser beams from zero to 1.9 MHz and back within 2 ms, yielding $\dot{\Omega} = 2\pi \times 1.9$ kHz/µs and $\Delta t = 6.8$ µs. From these parameters, we estimate the maximum energy gain, $\Delta E = 4\,\langle \dot{E} \rangle\,\Delta t$. We obtain $\Delta E = 1.2$ µK, which is much smaller than the heating rates obtained from the abrupt acceleration of the potential.

5.6   Conclusion and discussion

Using Ramsey and spin echo microwave spectroscopy, we investigated the coherence times of the electronic hyperfine ground states of cesium atoms trapped in our standing wave optical dipole trap. Various decoherence mechanisms have been observed and classified. From the decay of the Ramsey fringes we infer the reversible dephasing (T_2^*) caused by the inhomogeneous energy distribution in the trap leading to a distribution of differential light shifts. We demonstrated that this dephasing can be reversed resulting in the observation of spin echoes. The irreversible dephasing (T_2') manifests itself in a decay of the visibility of the spin echo. We observed coherence times $T_2' > 100$ ms for the lowest trap depths. Population relaxation (T_1) can be neglected in our experiment.

The different time scales of the decay mechanisms ($T_2^* \ll T_2' \ll T_1$) allow us to develop an analytical model which treats the various decay mechanisms independently. The model perfectly reproduces the observed shapes of Ramsey and spin echo signals, whose envelope is the Fourier transform of the energy distribution in the trap. The irreversible decoherence rates manifest themselves in the decay of the spin echo visibility and are caused by fluctuations of the atomic resonance frequency in between the microwave pulses. A significant part of this chapter was devoted to the analysis of mechanisms causing this decoherence mechanism. We found that the dominant decoherence effect is the pointing instability of the dipole trap laser beams.

Compared to our experiment, significantly longer coherence times ($T_2^* = 4$ s) were observed by N. Davidson and S. Chu in blue detuned traps in which the atoms are trapped in the minimum of electric fields [97]. In this paper, $T_2^* = 15$ ms obtained with sodium atoms in a Nd:YAG dipole trap ($U_0 = 0.4$ mK) was reported, which is comparable to our observation. In other experiments, the inhomogeneous broadening has been

reduced by the addition of a weak light field, spatially overlapped with the trapping laser field and whose frequency is tuned in between the two hyperfine levels [110]. Of course, cooling the atoms to the lowest vibrational level by using e. g. Raman sideband cooling techniques [111, 112], would also reduce inhomogeneous broadening. Finally, magnetic field fluctuations could be suppressed by triggering the experiment to the 50 Hz of the power line.

Last but not least, we demonstrated that the coherence even persists while moving the atoms back and forth over macroscopic distances by shifting the standing wave dipole trap. The fringe visibility of the spin echo is only reduced by less than a factor of 2 if we transport the atoms between the application of the microwave pulses, showing that the evolution of the external states is decoupled from the internal states.

Chapter 6

Conclusion and outlook

I have presented novel techniques to realize controllable quantum systems of neutral atoms. Besides the preparation of the exact number of atoms, we manipulate all physical degrees of freedom of the trapped particles. While the "optical conveyor belt" manipulates the external degrees of freedom of the atom by precisely controlling its position, we use microwave radiation to coherently couple its ground state hyperfine levels, which represent the internal degrees of freedom.

One of the major achievements of this work is the first transportation of a single trapped atom over macroscopic distances in the order of a centimeter with micrometer precision. This offers the possibility of providing a given number of atoms for further experiments at a time set by the experimentalist. Together with the automatic loading of atoms from the MOT, we have realized a deterministic source of cold atoms.

A significant part of this thesis was devoted to developing methods for the coherent manipulation of the atomic internal states at the level of a single atom. In particular, we studied decoherence effects of the hyperfine ground states of trapped atoms using Ramsey spectroscopy. The coherence times exceeded 100 ms and are currently limited by pointing instabilities of the dipole trap laser. Finally, we proved that the coherence even persists during transportation of the atoms.

We have demonstrated that a trapped atom can be well isolated from its environment and that its hyperfine ground states are possible candidates to represent qubits in quantum information processing. In this context, we demonstrated techniques for preparation and readout of the qubits. Compared to ions, however, the use of neutral atoms is a relatively novel technique. Thus, more advanced implementations such as individual addressing or controlled interaction between the atoms are still being developed.

Our system may have the potential to master these challenges. Imaging the atoms with high resolution combined with a spatially dependent resonance frequency should permit the simultaneous preparation and readout of quantum states of many atoms. Moreover, we plan to transport two neutral atoms into the fundamental mode of a high-finesse optical
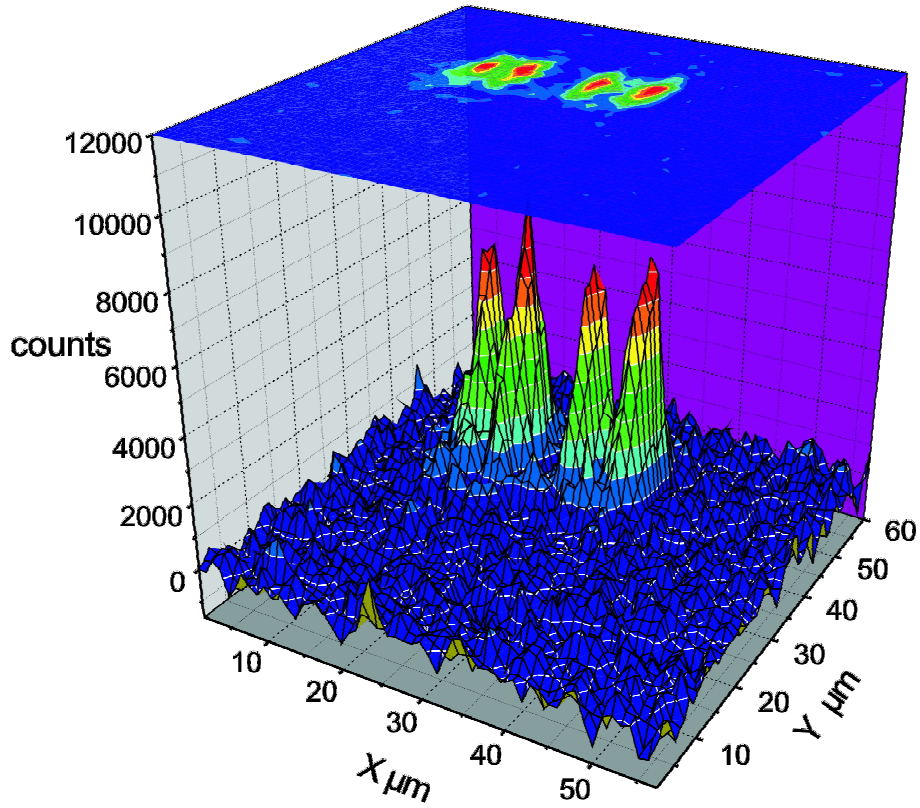
Figure 6.1: Image of four atoms in the dipole trap, which was operated together with the MOT. The image was taken by an intensified CCD camera with an integration time of 1 s.

cavity, where they can interact via the exchange of a virtual photon.

6.1   Individual addressing

Most recently, we have installed an intensified CCD camera (Princeton Instruments, PI-MAX 1KHQ) which permits a spatially resolved imaging of the atoms in the dipole trap. The imaging system consists of the objective used for collecting fluorescence of the MOT together with a lens ($f = 500$ mm). This results in a magnification by a factor of 14, such that 1 µm is imaged onto one CCD pixel. One of the very first pictures of trapped atoms is shown in Figure 6.1, where we can see four atoms trapped in different potential wells of the standing wave separated by $7 - 10$ µm in this case. During the exposure time of 1 s both MOT and dipole trap were simultaneously operated. We observed that the atoms remain in their potential wells during simultaneous operation of dipole trap and MOT. Note that the resolution of the imaging system does not allow us to resolve neighboring potential wells of the standing wave. Nonetheless, we are able to determine the position of the trapped particles with a precision of up to 0.1 µm by fitting methods.

For the use of atoms as quantum memories, it is desirable to address and to read out the quantum state of the trapped atoms individually. Due to the small separation it is rather difficult to realize direct addressing by a tightly focussed laser beam as employed in linear ion traps [113]. Based on the techniques developed within this thesis, a more promising method could be to use a magnetic field gradient, such that each atom along the standing wave possesses a different resonance frequency. The strong field gradient produced by the MOT coils yields a spatially dependent shift of the $|F = 4, m_\mathrm{F} = 4\rangle \rightarrow |F = 3, m_\mathrm{F} = 3\rangle$ hyperfine transition of 37 kHz/µm. As a consequence, a monochromatic microwave is resonant with only one of the atoms along the standing wave, allowing us to change its hyperfine state independently of the other trapped atoms. For an experimental implementation, one would rather employ adiabatic passages to transfer population between the hyperfine states, since this technique is more robust against frequency mismatches and jitters.

As a test of individual addressing, we could record an image of the chain of atoms at the beginning of a possible experimental sequence, before we apply microwave pulses and state selectively remove the atoms from the trap. Finally, a second image is recorded showing absence or presence of the remaining atoms.

Although it is not yet possible to deterministically place the atoms into particular wells of the standing wave, our method allows us at least to determine their position with high spatial resolution. One could employ a feedback mechanism by using a computer program which automatically determines the position of the atom and then sets the microwave frequency to the appropriate value. A similar feedback mechanism could be employed to position the atoms with a sub-wavelength absolute accuracy.

6.2 Transport of atoms into a high finesse resonator

The possibility of coherently transporting quantum states should allow us to let atoms interact at a location different from the preparation and read out. More specifically, our experiments aim at the deterministic transport of two or more atoms into an optical high finesse resonator, where they could controllably interact via photon exchange. Numerous proposals exist which require two or more neutral atoms simultaneously coupled to the electromagnetic field of the resonator. This should enable us to entangle neutral atoms via the exchange of virtual photons [23] or to realize a quantum gate [22, 114]. In contrast to microwave resonators, the use of an optical cavity allows us to use the system as a source of individual photons [115, 116, 117] or of a stream of entangled single-photon wave packets [118]. Ambitious proposals even suggest mapping the quantum state of a trapped atom onto a photon and sending it to another atom [119].

Most of the above proposals require a coherent energy exchange of the atomic excitation
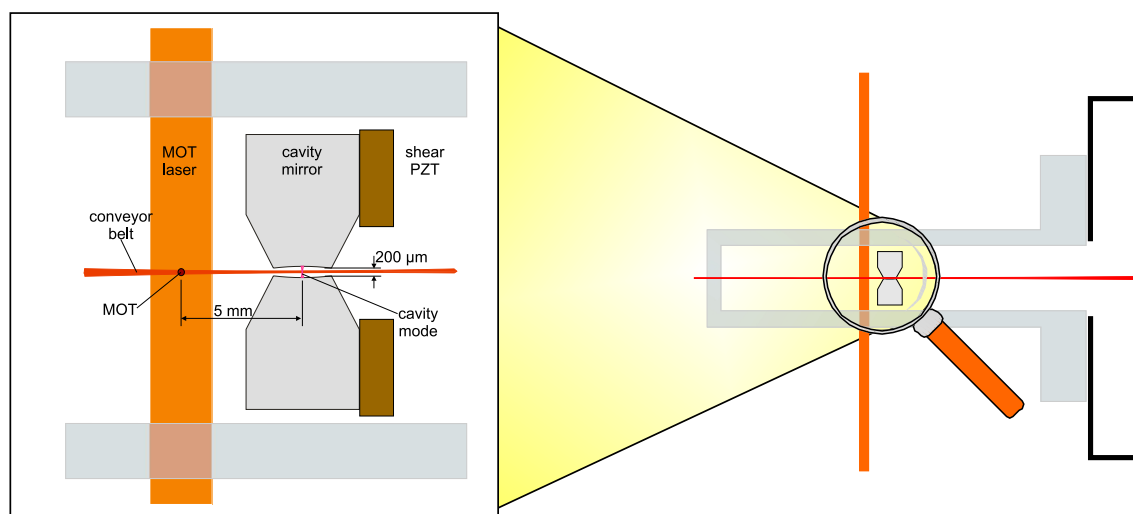
Figure 6.2: Scheme of the planned experiment. The optical conveyor belt will transport atoms from the MOT into the cavity mode.

with the cavity mode. This can only be accomplished in the "strong coupling regime", when the atom-cavity coupling is larger than all loss rates. Within the recent months, a suitable optical cavity system has already been designed and assembled in a second vacuum chamber, with the goal of being compatible with the current setup [120]. Our plan is to place the cavity about 5 mm away from the MOT (see Figure 6.2) and to transport the atoms into the cavity using the conveyor belt.

Appendix A

Atomic data for ^{133}Cs

In this appendix I summarize the most important properties of ^{133}Cs relevant for this work. Most of the data is extracted from the data collection of D. Steck [85].

general properties		
mass	m	2.21×10^{-25} kg
^{2}S$_{1/2}$ ground state HFS	ω_{hfs}	$2\pi \times 9.192\,631\,770$ GHz (def.)
Zeeman shift (^{2}S$_{1/2}$)	$\Delta\omega_{m_3 \to m_4}$	$2\pi \times 3.51$ kHz/µT $(m_3 + m_4)$
quadratic Zeeman shift	$\Delta\omega_{0 \to 0}$	$2\pi \times 43$ mHz/(µT)^2

Table A.1: General properties of ^{133}Cs.

D$_1$-line		
wavelength	λ	894.35 nm
transition frequency	ν	335.12 THz
natural linewidth	Γ	$2\pi \times 4.68$ MHz
detuning from $\lambda = 1064$ nm	Δ_1	$-2\pi \times 53.6$ THz

D$_2$-line		
wavelength	λ	852.11 nm
transition frequency	ν	351.73 THz
natural linewidth	Γ	$2\pi \times 5.22$ MHz
Doppler temperature	$\dfrac{\hbar\Gamma}{2k_{\text{B}}}$	125 µK
saturation intensity	I_0	1.1 mW/cm^2
recoil energy	$E_{\text{r}}/\hbar$	$2\pi \times 2.0$ kHz
detuning from $\lambda = 1064$ nm	Δ_2	$-2\pi \times 70.1$ THz

Table A.2: Parameters of the D-lines.

Cs atoms in a standing wave dipole trap

The following values are calculated for a Cs atom in a standing wave dipole trap ($U_0 = 1.0$ mK) made of two Nd:YAG laser beams ($\lambda = 1064$ nm):

effective detuning	Δ_{eff}	1.2×10^7 Γ	Eq. (2.35),	p. 12
axial oscillation frequency	Ω_z	$2\pi \times 235$ kHz	Eq. (2.40a),	p. 13
radial osc. frequency ($w_0 = 30$ µm)	Ω_r	$2\pi \times 2.7$ kHz	Eq. (2.40b),	p. 13
scattering rate	Γ_{sc}	11 s^{-1}	Eq. (2.34),	p. 12
differential light shift	δ_{ls}	$2\pi \times 3.0$ kHz	Eq. (5.8),	p. 78

Table A.3: Parameters of Cs atoms in a standing wave dipole trap.

Collisional shift of the clock transition

Figure A.1 shows the collisional shift of the $|F = 4, m_F = 0\rangle \to |F = 3, m_F = 0\rangle$ transition. The calculations were done in the group of P. Julienne and C. Williams (NIST, Gaithersburg). Part of these results have been published in [89].
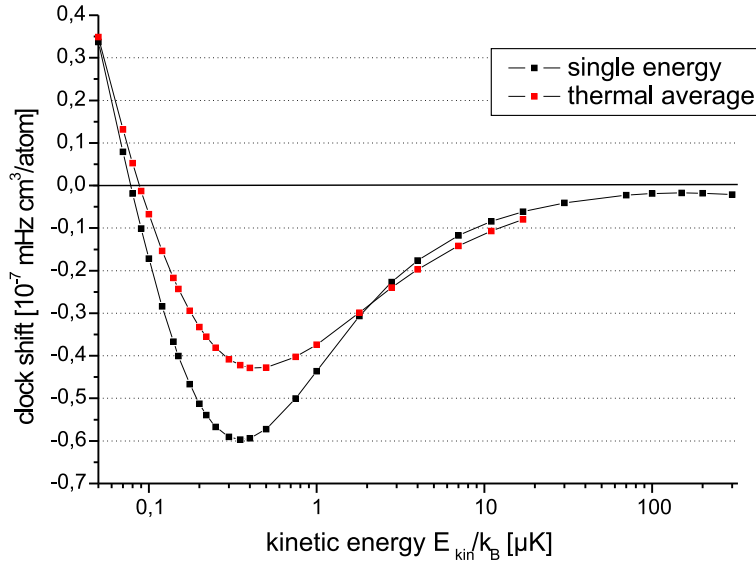
Figure A.1: Collision shift of the clock transition. (Courtesy of V. Venturi and C. Williams, NIST, Gaithersburg),

Appendix B

Computer control system

A part of my thesis was devoted to the development of a computer control system for the experiment. Its heart is a software permitting the rapid design of rather complex sequences of digital and analog signals, which are used to switch on and off laser beams, to trigger microwave pulses, or to alter magnetic fields, detunings or intensities.

Hardware

The hardware consists of three PC boards, mounted in a standard personal computer. A digital-IO board (National Instruments, PCI DIO32-HS) has 32 TTL outputs being either "low" (0 V) or "high" (5 V). Two 12-bit D/A boards (National Instruments, PCI 6733) each provide 8 channels producing analog output voltages in the range of -10 V to $+10$ V. Arrays of the computer memory containing bit patterns of TTL signals or digitized analog voltages can be assigned to the boards. These signals are subsequently sent to the outputs with a maximum possible rate of 500 kSamples/s for the analog board. This yields a time resolution of 2 µs, limited by bus transfer rates from the PC memory to the board. The digital board permits a maximum output rate of 20 MSamples/s which corresponds to a time resolution of 50 ns, but we restrict ourselves to a time resolution of 2 µs for the digital board as well to simplify synchronization with the analog signals.

Synchronization of the boards is achieved via a special databus (RTSI) connecting the devices. A 20 MHz clock signal is routed from one analog board to the other two boards. This is done to avoid time shifts between the output signals of the different boards, since without synchronization all clocks run at slightly different frequencies. Signals for starting and stopping the pattern generation are transmitted via the RTSI bus as well to guarantee that all boards simultaneously start the data output. The sequence can be started automatically or triggered externally, for example by a signal derived from the 50 Hz of the power line.
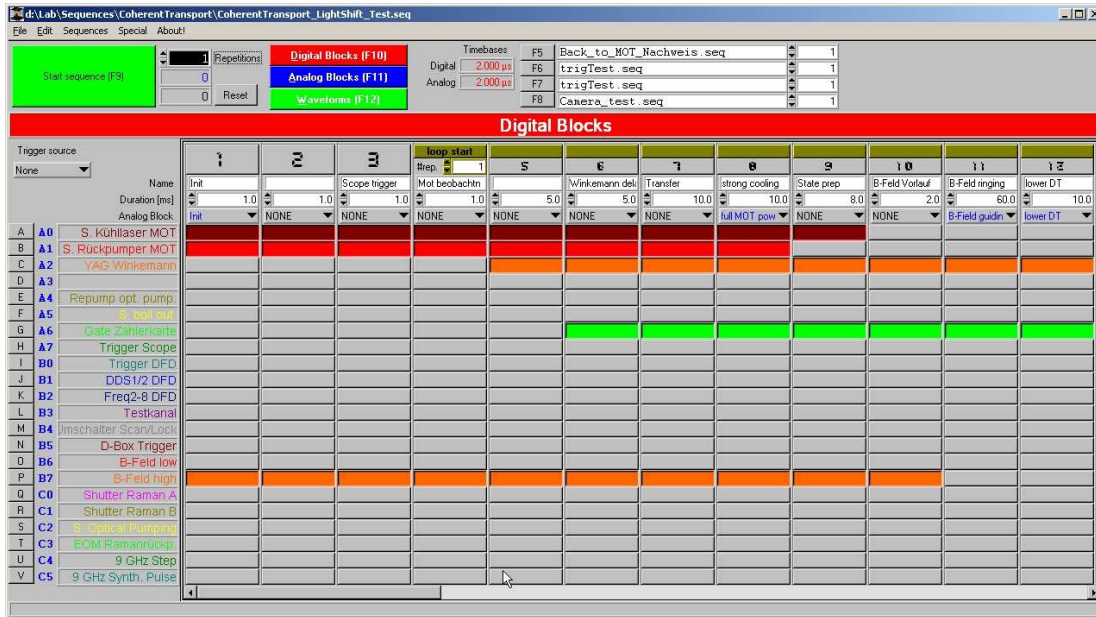
Figure B.1: Computer control system. The graphical user interface permits the rapid design of complex experimental operating sequences. The digital blocks define the sequence of the 32 TTL output channels.

Software

The software provides a graphical user interface which enables the rapid design of complex "sequences" to realize a specific experimental procedure (see the screen shot in Figure B.1). A sequence defines a complete set of digital and analog signals. The skeleton of a sequence is formed by a series of "digital blocks", containing the patterns for the digital-IO board, which are played back from left to right. For each digital block the user can specify the duration and an "analog block" to be started. An analog block is composed of "waveforms", which define arbitrary analog output signals. The sequences can be loaded and saved to the hard disk. Several of them are kept in memory simultaneously, and the user can also specify the number of repetitions of each sequence.

In the following I describe in detail the features of the various constituents of a sequence.

Digital blocks The digital blocks define the 32 TTL output signals (A0−D7) of the digital-IO board (see Figure B.1). They are used for controlling mechanical shutters for the lasers, or for triggering electronic devices such as the "timer card" to record photon counts, oscilloscopes, the 9.2 GHz synthesizer or the frequency generator which controls the motion of the conveyor-belt. A digital block can be of fixed or variable duration, being increased or decreased automatically by a specified amount after each repetition. This is useful for the automatic recording of e. g. Rabi oscillations or Ramsey fringes, where the pulse length or the time between pulses has to be varied, respectively. "Loops" permit several repetitions of selected digital blocks

a)
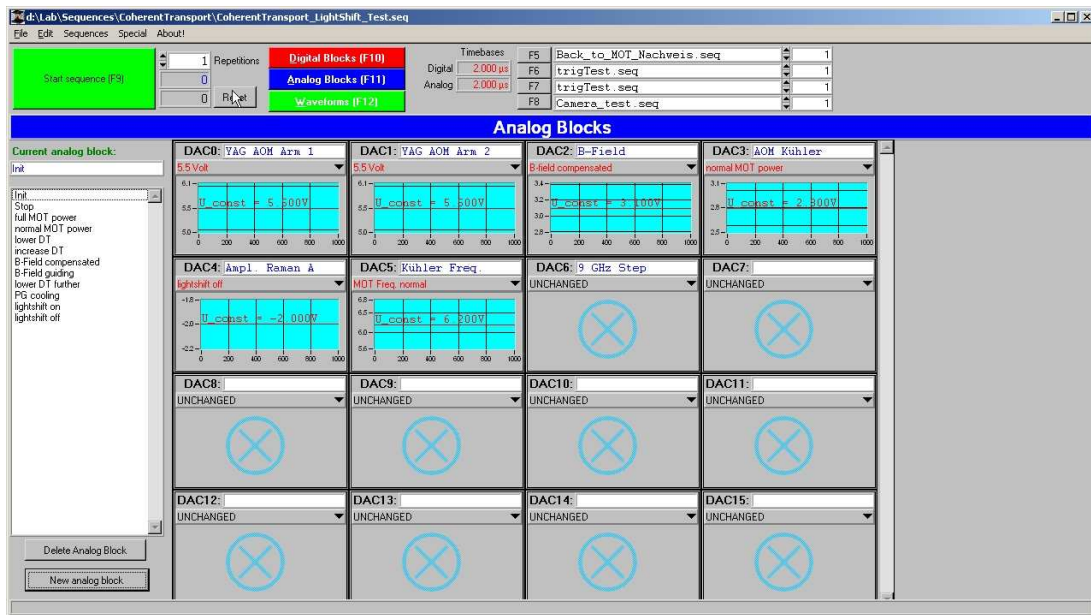
b)
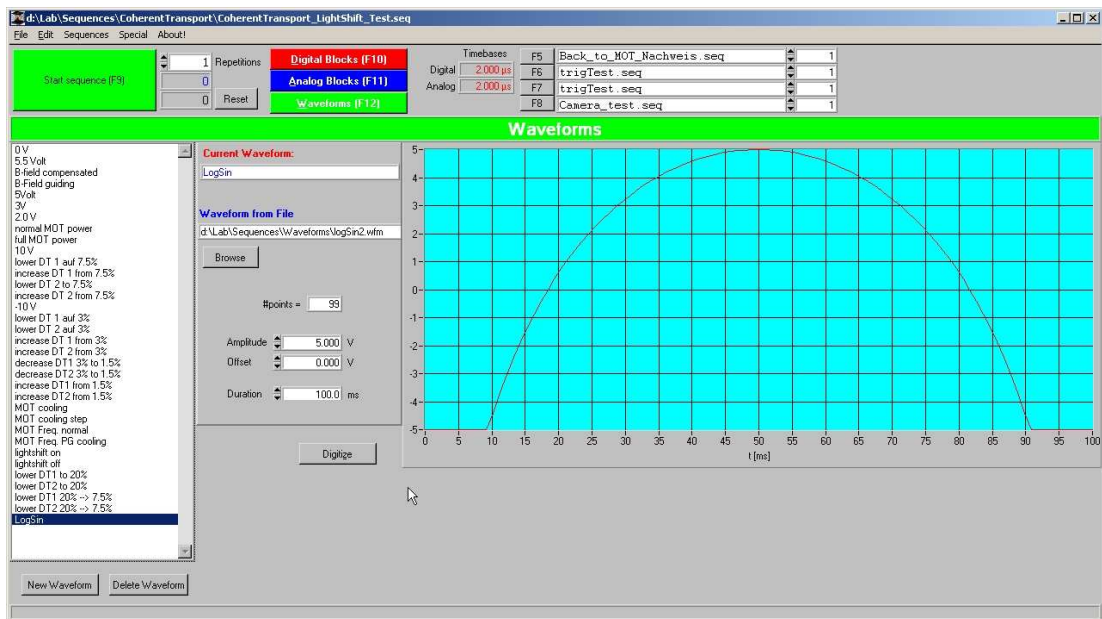
Figure B.2: Computer control system. (a) The "analog blocks" control the output of the 16 analog channels and are composed of "waveforms". (b) Waveforms contain arbitrary sequences of voltages which may be loaded from an external file.

within a sequence.

Analog block In each digital block an analog block can be started which controls the output of the 16 analog channels (DAC0−DAC15) of the D/A-boards, see Figure B.2(a). For each of these channels the user can determine an arbitrary waveform to be generated or set the output channel to "unchanged". This way the duration of the waveforms of an analog block does not need to coincide with the duration of the digital block from which it is started. All waveforms in an analog block are generated for their specified duration or until a different analog bock containing a different waveform is started in a subsequent block. A waveform in an analog block can be also set to "hold" which freezes the current voltage.

Waveforms A waveform consists of a series of voltages and corresponding durations serving for example for the programming of arbitrary linear ramps. More complicated waveforms, such as a sine wave or a pulse with gaussian envelope, are loaded from external files. Moreover, the waveform can be set such that the output voltage is increased by a specified amount after each repetition.

The software is written in LabWindows CVI 5.5 (National Instruments), an integrated development environment (IDE), consisting of a C compiler and an editor for graphical user interfaces. Special libraries are provided which contain routines for the communication with the hardware.

List of Figures

List of Tables

115

Bibliography

[1] E. Schrödinger, *Are there quantum jumps?*, Br. J. Philos. Sci. **3**, 109–123 and 233–242 (1952)

[2] P. Pinkse, T. Fischer, P. Maunz and G. Rempe, *Trapping an atom with single photons*, Nature **404**, 365 (2000)

[3] C. Hood, T. Lynn, A. Doherty, A. Parkins and H. Kimble, *The Atom-Cavity Microscope: Single Atoms Bound in Orbit by Single Photons*, Science **287**, 1447 (2000)

[4] M. Brune, P. Nussenzveig, F. Schmidt-Kaler, F. Bernardot, A. Maali, J. M. Raimond and S. Haroche, *From Lamb shift to light shifts: Vacuum and subphoton cavity fields measured by atomic phase sensitive detection*, Phys. Rev. Lett. **72**, 3339 (1994)

[5] S. Kuhr, W. Alt, D. Schrader, M. Müller, V. Gomer and D. Meschede, *Deterministic delivery of a single atom*, Science **293**, 278, [published online June 14, 2001; 10.1126/science.1062725] (2001)

[6] D. Schrader, S. Kuhr, W. Alt, M. Müller, V. Gomer and D. Meschede, *An optical conveyor belt for single neutral atoms*, Appl. Phys. B **73**, 819 (2001)

[7] P. Shor, *Polynomial-time algorithms for prime factorization and discrete logarithms on a quantum computer*, SIAM J. Comp. **26**, 1484 (1997)

[8] L. Grover, *Quantum mechanics helps in searching for a needle in a haystack*, Phys. Rev. Lett. **97**, 325 (1997)

[9] D. P. DiVincenzo, G. Burkard, D. Loss and E. V. Sukhorukov, *Quantum Computation and Spin Electronics*, in: I. O. Kulik and R. Ellialtioglu (ed.), *Quantum Mesoscopic Phenomena and Mesoscopic Devices in Microelectronics*, p. 399, NATO Advanced Study Institute, Turkey, (preprint: cond-mat/9911245) (1999)

[10] I. L. Chuang, L. M. K. Vandersypen, X. Zhou, D. W. Leung and S. Lloyd, *Experimental realization of a quantum algorithm*, Nature **393**, 143 (1998)

[11] B. E. Kane, *A silicon-based nuclear spin quantum computer*, Nature **393**, 133 (1998)

[12] Y. Maklin, G. Schön and A. Shnirman, *Quantum-state engineering with Josephson-junction devices*, Rev. Mod. Phys. **73**, 357 (2001)

[13] N. Gisin, G. Ribordy, W. Tittel and H. Zbinden, *Quantum cryptography*, Rev. Mod. Phys. **74**, 145 (2002)

[14] Q. A. Turchette, C. S. Wood, B. E. King, C. J. Myatt, D. Leibfried, W. M. Itano, C. Monroe and D. J. Wineland, *Deterministic entanglement of two trapped ions*, Phys. Rev. Lett. **81**, 3631 (1998)

[15] C. A. SACKETT, D. KIELPINSKI, B. E. KING, C. LANGER, V. MEYER, C. J. MYATT, M. ROWE, Q. A. TURCHETTE, W. M. ITANO, D. J. WINELAND AND C. MONROE, *Experimental entanglement of four trapped ions*, Nature **404**, 256 (2000)

[16] C. MONROE, D. M. MEEKHOF, B. E. KING, W. M. ITANO AND D. J. WINELAND, *Demonstration of a Fundamental Quantum Logic Gate*, Phys. Rev. Lett. **75**, 4714 (1995)

[17] S. GULDE, M. RIEBE, G. P. T. LANCASTER, C. BECHER, J. ESCHNER, H. HÄFFNER, F. SCHMIDT-KALER, I. L. CHUANG AND R. BLATT, *Implementing the Deutsch-Jozsa algorithm on an ion-trap quantum computer*, Nature **421**, 48 (2003)

[18] D. JAKSCH, H.-J. BRIEGEL, J. CIRAC, C. GARDINER AND P. ZOLLER, *Entanglement of atoms via cold controlled collisions*, Phys. Rev. Lett. **82**, 1975 (1999)

[19] G. BRENNEN, C. CAVES, P. JESSEN AND I. DEUTSCH, *Quantum Logic Gates in Optical Lattices*, Phys. Rev. Lett. **82**, 1060 (1999)

[20] D. JAKSCH, J. I. CIRAC, P. ZOLLER, S. L. ROLSTON, R. CÔTÉ AND M. D. LUKIN, *Fast quantum gates for neutral atoms*, Phys. Rev. Lett. **85**, 2208 (2000)

[21] L. YOU AND M. CHAPMAN, *Quantum entanglement using trapped atomic spins*, Phys. Rev. A **62**, 052302 (2000)

[22] T. PELLIZZARI, S. A. GARDINER, J. I. CIRAC AND P. ZOLLER, *Decoherence, Continous Observation and Quantum Computing: A Cavity QED Model*, Phys. Rev. Lett **75**, 3788 (1995)

[23] S.-B. ZHENG AND G.-C. GUO, *Efficient Scheme for Two-Atom Entanglement and Quantum Information Processing in Cavity QED*, Phys. Rev. Lett. **85**, 2392 (2000)

[24] A. RAUSCHENBEUTEL, G. NOGUES, S. OSNAGHI, P. BERTET, M. BRUNE, J. M. RAIMOND AND S. HAROCHE, *Coherent Operation of a Tunable Quantum Phase Gate in Cavity QED*, Phys. Rev. Lett. **83**, 5166 (1999)

[25] A. RAUSCHENBEUTEL, G. NOGUES, S. OSNAGHI, P. BERTET, M. BRUNE AND S. HAROCHE, *Step-by-Step engineered multiparticle entanglement*, Science **288**, 2024 (2000)

[26] V. S. LETOKHOV, Pis. Zh. Eksp. Teor. Fiz. **7**, 348, engl. translation JTEP Lett. **7**, 272 (1968)

[27] A. ASHKIN, *Acceleration and Trapping of Particles by Radiation Pressure*, Phys. Rev. Lett. **24**, 156 (1970)

[28] T. W. HÄNSCH AND A. SCHAWLOW, *Cooling of Gases by Laser Radiation*, Opt. Commun. **13**(1), 68 (1975)

[29] D. WINELAND AND H. DEHMELT, *Proposed $10^{14}\Delta\nu < \nu$ Laser Fluorescence Spectroscopy on Tl^+ Mono-Ion Oscillator III (side band cooling)*, Bull. Am. Phys. Soc. **20**, 637 (1975)

[30] S. CHU, L. HOLLBERG, J. E. BJORKHOLM, A. CABLE AND A. ASHKIN, *Three-dimensional Viscous Confinement and Cooling of Atoms by Resonance Radiation Pressure*, Phys. Rev. Lett. **55**, 48 (1985)

[31] S. CHU, J. E. BJORKHOLM, A. ASHKIN AND A. CABLE, *Experimental observation of optically trapped atoms*, Phys. Rev. Lett. **57**, 314 (1986)

[32] E. L. RAAB, M. PRENTISS, A. CABLE, S. CHU AND D. E. PRITCHARD, *Trapping of Neutral Sodium Atoms with Radiation Pressure*, Phys. Rev. Lett. **59**, 2631 (1987)

[33] Z. HU AND H. J. KIMBLE, *Observation of a single atom in a magnetooptical trap*, Opt. Lett. **19**, 1888 (1994)

[34] F. RUSCHEWITZ, D. BETTERMANN, J. L. FENG AND W. ERTMER, *Statistical investigations on single trapped neutral atoms*, Europhys. Lett. **34**, 651 (1996)

[35] D. HAUBRICH, H. SCHADWINKEL, F. STRAUCH, B. UEBERHOLZ, R. WYNANDS AND D. MESCHEDE, *Observation of individual neutral atoms in magnetic and magnetooptical traps*, Europhys. Lett. **34**, 663 (1996)

[36] V. GOMER, F. STRAUCH, B. UEBERHOLZ, S. KNAPPE AND D. MESCHEDE, *Single-atom dynamics revealed by photon correlations*, Phys. Rev. A **58**(3), 1657 (1998)

[37] V. GOMER, B. UEBERHOLZ, S. KNAPPE, F. STRAUCH, D. FRESE AND D. MESCHEDE, *Decoding the dynamics of a single trapped atom from photon correlations*, Appl. Phys. B **67**, 689 (1998)

[38] B. UEBERHOLZ, S. KUHR, D. FRESE, V. GOMER AND D. MESCHEDE, *Counting cold collisions*, J. Phys. B: At. Mol. Opt. Phys. **33**, L135 (2000)

[39] B. UEBERHOLZ, S. KUHR, D. FRESE, V. GOMER AND D. MESCHEDE, *Cold collisions in a high-gradient magneto-optical trap*, J. Phys. B: At. Mol. Opt. Phys. **35**, 4899 (2002)

[40] D. FRESE, *Einzelne Atome in einer optischen Dipolfalle*, Diploma thesis, Universität Bonn (1999)

[41] D. FRESE, B. UEBERHOLZ, S. KUHR, W. ALT, D. SCHRADER, V. GOMER AND D. MESCHEDE, *Single Atoms in an Optical Dipole Trap: Towards a Deterministic Source of Cold Atoms*, Phys. Rev. Lett. **85**, 3777 (2000)

[42] H. J. METCALF AND P. VAN DER STRATEN, *Laser Cooling and Trapping*, Springer, 1st edition (1999)

[43] D. WINELAND AND W. ITANO, *Laser cooling of atoms*, Phys. Rev. A **20**, 1521 (1979)

[44] P. D. LETT, R. N. WATT, C. I. WESTBROOK, W. D. PHILLIPS, P. L. GOULD AND H. J. METCALF, *Observation of Atoms Laser Cooled below the Doppler Limit*, Phys. Rev. Lett. **61**(2), 169 (1988)

[45] J. DALIBARD AND C. COHEN-TANNOUDJI, *Laser cooling below the Doppler limit by polarization gradients: simple theoretical models*, J. Opt. Soc. Amer. B **6**, 2023 (1989)

[46] R. GRIMM, M. WEIDEMÜLLER AND Y. B. OVCHINNIKOV, *Optical dipole traps for neutral atoms*, Adv. At. Mol. Opt. Phys. **42**, 95 (2000)

[47] J. D. JACKSON, *Classical Electrodynamics*, Wiley, New York, 2nd edition (1962)

[48] C. COHEN-TANNOUDJI, J. DUPONT-ROC AND G. GRYNBERG, *Atom-Photon Interactions*, Wiley, New York (1992)

[49] J. J. SAKURAI, *Modern Quantum Mechanics*, Addison Wesley, 2nd edition (1994)

[50] I. I. SOBELMAN, *Atomic Spectra and Radiative Transitions*, Springer, Berlin (1996)

[51] A. R. EDMONDS, *Angular momentum in quantum mechanics*, Princeton University Press, Princeton, 3rd edition (1974)

[52] N. SCHLOSSER, *Étude et réalisation de micro-pièges dipolaires optiques pour atoms neutres*, Ph.D. thesis, Université Paris XI (2001)

[53] D. SCHRADER, *AC Stark shift*, personal communication (2001)

[54] J. MCKEEVER, J. R. BUCK, A. D. BOOZER, A. KUZMICH, H.-C. NÄGERL, D. M. STAMPER-KURN AND H. J. KIMBLE, *State-Insensitive Trapping of Single Atoms in an Optical Cavity*, Phys. Rev. Lett **90**, 133602 (2003)

[55] D. SCHRADER, *Ein Förderband für einzelne Atome*, Diploma thesis, Universität Bonn (2000)

[56] W. ALT, *An objective lens for efficient fluoresence detection of single atoms*, Optik **113**, 142 (2002)

[57] C. WIEMAN AND T. W. HÄNSCH, *Doppler-Free Laser Polarization Spectroscopy*, Phys. Rev. Lett. **36**, 1170 (1976)

[58] W. DEMTRÖDER, *Laserspektroskopie*, Springer, Berlin, 2nd edition (1991)

[59] K. DÄSTNER, *Korrelationsmessungen an einzelnen neutralen Atomen*, Diploma thesis, Universität Bonn (1996)

[60] D. HAUBRICH, A. HÖPE AND D. MESCHEDE, *A simple model for optical capture of atoms in strong magnetic quadrupole fields*, Opt. Comm. **102**, 225 (1993)

[61] H. SCHADWINKEL, *Die Magnetooptische Falle als lichtgebundenes Atomgitter*, Ph.D. thesis, Universität Bonn (1998)

[62] S. KUHR, B. UEBERHOLZ, D. FRESE, V. GOMER AND D. MESCHEDE, *Counting Cold Collisions*, in: R. BLATT, J. ESCHNER, D. LEIBFRIED AND F. SCHMIDT-KALER (ed.), *Laser Spectroscapy, XIV International Conference*, 334, World Scientific, Singapore (1999)

[63] B. UEBERHOLZ, *Kalte Stöße in einer magnetooptischen Falle mit hohem Magnetfeldgradienten*, Ph.D. thesis, Universität Bonn (2001)

[64] W. ALT, D. SCHRADER, S. KUHR, M. MÜLLER, V. GOMER AND D. MESCHEDE, *Properties of single atoms in an optical dipole trap*, Phys. Rev. A **67**, 033403 (2003)

[65] R. BARLOW, *Statistics*, Wiley, New York (1989)

[66] S. B. HILL AND J. J. MCCLELLAND, *Atoms on demand: Fast, deterministic production of single Cr atoms*, Appl. Phys. Lett. **82**, 3128 (2003)

[67] N. SCHLOSSER, G. REYMOND, I. PROTSENKO AND P. GRANGIER, *Sub-poissonian loading of single atoms in a microscopic dipole trap*, Nature **411**, 1024 (2001)

[68] N. SCHLOSSER, G. REYMOND AND P. GRANGIER, *Collisional Blockade in Microscopic Optical Dipole Traps*, Phys. Rev. Lett. **89**, 023005 (2002)

[69] P. ROSENBUSCH, B. V. HALL, I. G. HUGHES, C. V. SABA AND E. A. HINDS, *Manipulation of cold atoms using a corrugated magnetic reflector*, Phys. Rev. A **61**, 031404 (2000)

[70] J. DENSCHLAG, D. CASSETTARI AND J. SCHMIEDMAYER, *Guiding Neutral Atoms with a Wire*, Phys. Rev. Lett. **82**, 2014 (1999)

[71] M. GREINER, I. BLOCH, T. HÄNSCH AND T. ESSLINGER, *Magnetic transport of trapped cold atoms over a large distance*, Phys. Rev. A **63**, 031404(R) (2001)

[72] W. HÄNSEL, J. REICHEL, P. HOMMELHOFF AND T. W. HÄNSCH, *Magnetic Conveyor Belt for Transporting and Merging Trapped Atoms Clouds*, Phys. Rev. Lett. **86**, 608 (2001)

[73] T. L. GUSTAVSON, A. P. CHIKKATUR, A. E. LEANHARDT, A. GÖRLITZ, S. GUPTA, D. E. PRITCHARD AND W. KETTERLE, *Transport of Bose-Einstein Condensates with Optical Tweezers*, Phys. Rev. Lett. **88**, 020401 (2002)

[74] M. B. DAHAN, E. PEIK, J. REICHEL, Y. CASTIN AND C. SALOMON, *Bloch Oscillations of Atoms in an Optical Potential*, Phys. Rev. Lett. **76**, 4508 (1996)

[75] S. R. WILKINSON, C. F. BHARUCHA, K. W. MADISON, Q. NIU AND M. G. RAIZEN, *Observation of Atomic Wannier-Stark Ladders in an Accelerating Optical Potential*, Phys. Rev. Lett. **76**, 4512 (1996)

[76] W. ALT, *Dreistrahlinterferenz: Ein Heizmechanismus in der Stehwellenfalle*, personal communication (2001)

[77] F. BLOCH, *Nuclear Induction*, Phys. Rev. **70**, 460 (1946)

[78] L. ALLEN AND J. H. EBERLY, *Optical resonance and two-level atoms*, Wiley, New York (1975)

[79] C. COHEN-TANNOUDJI, B. DIU AND F. LALOË, *Quantum Mechanics*, Wiley, New York (1977)

[80] A. RAUSCHENBEUTEL, *Atomes et cavité: Préparation et manipulation d'états intriqués complexes*, Ph.D. thesis, Université Paris VI, Paris (2001)

[81] V. VULETIĆ, C. CHIN, A. J. KERMAN AND S. CHU, *Degenerate Raman Sideband Cooling of Trapped Cesium Atoms at Very High Atomic Densities*, Phys. Rev. Lett. **81**, 5768 (1998)

[82] I. BOUCHOULE, *Refroidissement par bandes latérales d'atomes de Césium et quelques applications*, Ph.D. thesis, Université Paris VI, Paris (2000)

[83] A. J. KERMAN, *Raman sideband cooling and cold atomic collisions in optical lattices*, Ph.D. thesis, Stanford University (2002)

[84] G. BREIT AND I. I. RABI, *Measurement of Nuclear Spin*, Phys. Rev. **7**, 2082 (1931)

[85] D. A. STECK, *Cesium D Line Data*, http://steck.us/alkalidata/ (23 January 1998, Revision 1.4, 14 March 2002)

[86] I. DOTSENKO, *Raman spectroscopy of single atoms*, Diploma thesis, Universität Bonn (2002)

[87] E. TIESINGA, B. J. VERHAAR, H. T. C. STOOF AND D. VAN BRAGT, *Spin-exchange frequency shift in a cesium atomic fountain*, Phys. Rev. A **45**, 2671 (1992)

[88] K. GIBBLE AND S. CHU, *Laser-Cooled Cs Frequency Standard and a Measurement of the Frequency Shift due to Ultracold Collisions*, Phys. Rev. Lett. **70**, 1771 (1993)

[89] P. J. LEO, P. S. JULIENNE, F. H. MIES AND C. J. WILLIAMS, *Collisional Frequency Shifts in ^{133}Cs Fountain Clocks*, Phys. Rev. Lett. **86**, 3473 (2001)

[90] W. H. ZUREK, *Environment-induced superselection rules*, Phys. Rev. D **26**, 1862 (1982)

[91] W. H. ZUREK, *Decoherence and the transition from quantum to classical*, Physics Today **44**, 36 (October 1991)

[92] M. BRUNE, E. HAGLEY, J. DREYER, X. MAÎTRE, A. MAALI, C. WUNDERLICH, J. M. RAIMOND AND S. HAROCHE, *Observing the progressive decoherence of the "meter" in a quantum measurement*, Phys. Rev. Lett. **77**, 4887 (1996)

[93] S. Haroche, *Entanglement, decoherence and the quantum/classical boundary*, Physics Today **51**, 36 (July 1998)

[94] C. Monroe, D. M. Meekhof, B. E. King and D. J. Wineland, *A "Schrödinger cat" superposition state of an atom*, Science **272**, 1131 (1996)

[95] Q. A. Turchette, C. J. Myatt, B. E. King, C. A. Sackett, D. Kielpinski, W. M. Itano, C. Monroe and D. J. Wineland, *Decoherence and decay of motional quantum states of a trapped atom coupled to engineered reservoirs*, Phys. Rev. A **62**, 053807 (2000)

[96] F. Schmidt-Kaler, S. Gulde, M. Riebe, T. Deuschle, A. Kreuter, G. Lancaster, C. Becher, J. Eschner, H. Häffner and R. Blatt, *Coherence of qubits based on single Ca^+ ions*, J. Phys. B: At. Mol. Opt. Phys. **36**, 623 (2003)

[97] N. Davidson, H. J. Lee, C. S. Adams, M. Kasevich and S. Chu, *Long Atomic Coherence Times in an Optical Dipole Trap*, Phys. Rev. Lett. **74**, 1311 (1995)

[98] R. Ozeri, L. Khaykovich and N. Davidson, *Long spin relaxation times in a single-beam blue-detuned optical trap*, Phys. Rev. A **59**, R1750 (1999)

[99] N. Ramsey, *Molecular Beams*, Oxford University Press, London (1956)

[100] N. Ramsey, *The method of successive oscillatory fields*, Physics Today **33**, 25 (July 1980)

[101] J. Vanier and C. Audoin, *The Quantum Physics of Atomic Frequency Standards*, Adam Hilger, Bristol (1989)

[102] M. Kasevich, E. Riis, S. Chu and R. G. DeVoe, *RF Spectroscopy in an Atomic Fountain*, Phys. Rev. Lett. **63**, 612 (1989)

[103] E. Hahn, *Spin Echoes*, Phys. Rev. **80**, 580 (1950)

[104] M. F. Andersen, A. Kaplan and N. Davidson, *Echo spectroscopy and quantum stability for trapped atoms*, Phys. Rev. Lett **90**, 023001 (2003)

[105] R. A. Cline, J. D. Miller, M. R. Matthews and D. J. Heinzen, *Spin relaxation of optically trapped atoms by light scattering*, Opt. Lett. **19**, 207 (1994)

[106] D. W. Allan, *Statistics of atomic frequency standards*, Proc. IEEE **54**, 221 (1966)

[107] R. Loudon, *The Quantum Theory of Light*, Clarendon, Oxford (1983)

[108] M. A. Rowe, A. Ben-Kish, B. DeMarco, D. Leibfried, V. Meyer, J. Beall, J. Britton, J. Hughes, W. M. Itano, B. Jelenković, C. Langer, T. Rosenband and D. J. Wineland, *Transport of quantum states and separation of ions in a dual RF ion trap*, Quantum Information and Computation **2**, 257 (2002)

[109] O. Mandel, M. Greiner, A. Widera, T. Rom, T. W. Hänsch and I. Bloch, *Coherent transport of neutral atoms in spin-dependent optical lattice potentials*, cond-mat/0301169

[110] A. Kaplan, M. F. Andersen and N. Davidson, *Suppression of inhomogeneous broadening in rf spectroscopy of optically trapped atoms*, Phys. Rev. A **66**, 045401 (2002)

[111] S. E. Hamann, D. L. Haycock, G. Klose, P. H. Pax, I. H. Deutsch and P. S. Jessen, *Resolved Sideband Raman Cooling to the Ground State of an Optical Lattice*, Phys. Rev. Lett. **80**, 4149 (1998)

[112] H. Perrin, A. Kuhn, I. Bouchoule and C. Salomon, *Sideband cooling of neutral atoms in a far-detuned optical lattice*, Europhys. Lett. **42**, 395 (1998)

[113] H. C. Nägerl, D. Leibfried, H. Rohde, G. Thalhammer, J. Eschner, F. Schmidt-Kaler and R. Blatt, *Laser addressing of individual ions in a linear ion trap*, Phys. Rev. A **60**, 145 (1999)

[114] L. You, X. X. Yi and X. H. Su, *Quantum logic between atoms inside a high Q optical cavity*, quant-ph/0209096

[115] C. Law and H. J. Kimble, *Deterministic generation of a bit-stream of single-photon pulses*, J. Mod. Opt. **44**, 2067 (1997)

[116] A. Kuhn, M. Hennrich, T. Bondo and G. Rempe, *Controlled generation of single photons from a strongly coupled atom-cavity system*, Appl. Phys. B. **69**, 373 (1999)

[117] M. Hennrich, T. Legero, A. Kuhn and G. Rempe, *Vacuum-Stimulated Raman Scattering Based on Adiabatic Passage in a High-Finesse Optical Cavity*, Phys. Rev. Lett. **85**, 4872 (2000)

[118] K. M. Gheri, C. Saavedra, P. Törmä, J. I. Cirac and P. Zoller, *Entanglement engineering of one-photon wave packets using a single-atom source*, Phys. Rev. A **58**, R2627 (1998)

[119] J. I. Cirac, P. Zoller, H. J. Kimble and H. Mabuchi, *Quantum state transfer and entanglement distribution among distant nodes in a quantum network*, Phys. Rev. Lett. **78**, 3221 (1997)

[120] Y. Miroshnychenko, *Design and test of a high finesse resonator for single atom experiments*, Diploma thesis, Universität Bonn (2002)

Danksagung

Drei Jahre und ein wenig mehr sind im Fluge vergangen. Die vielseitige Arbeit an einem faszinierenden Experiment hat mir viel Freude bereitet. Prof. Dieter Meschede danke ich für die angenehme Arbeitsatmosphäre. Besonders geschätzt habe ich die Freiheit, die uns bei der experimentellen Umsetzung der Ideen im Labor gegeben war. Für unsere Projekte hatten wir immer seine volle Unterstützung, und das, obwohl wir bis heute weder blaue Laser eingesetzt noch "back-to-back"-Korrelationen gemessen haben. Prof. Norbert Wermes danke ich, daß er sich trotz seines vollen Terminkalenders bereiterklärt hat, das Korreferat zu übernehmen.

Nicht ein einziges Atom hätten wir gefangen und transportiert ohne Wolfgang Alt und Dominik Schrader, die das Experiment von der ersten Stunde an begleitet haben. Wolfgang brillierte mit seinem unglaublichen Spürsinn für physikalische Phänomene und seinem schier unendlichen Wissensschatz. Sein Zweckpessimismus hat mich – oft unsanft, aber meist gerechtfertigt – immer wieder auf den Boden der Tatsachen zurückgeholt. Dominik, der jede noch so komplizierte Rechnung mit beneidenswerter Präzision ausführen kann und alle Fragen und Probleme auf den Punkt bringt, verstand es nebenbei vortrefflich, uns alle anzutreiben – vor allem zu seiner Zeit als Diplomand. Abgesehen von dem Spaß, den wir bei der gemeinsamen Arbeit im Labor hatten, konnte ich ihn zum Glück schnell davon überzeugen, daß Bier ein wahrhaft köstliches Getränk ist. Unsere zahlreichen USA-Touren werden wir wohl auch nicht so schnell vergessen.

Zu uns kamen im Laufe der letzten Jahre die Diplomanden Martin Müller, Yevhen Miroshnychenko, Igor Dotsenko, Wenjamin Rosenfeld und Mika Khudaverdyan, die immer mit vollem Einsatz mitgewirkt haben und für die keine Meßnacht zu lang war. Unseren Post-Docs, Dr. Victor Gomer und Dr. Arno Rauschenbeutel, danke ich sehr für ihre Unterstützung. In ihrem Wissensfundus war immer die richtige Antwort auf unsere Fragen vorhanden.

Was wäre eine experimentelle Arbeit ohne unsere Werkstätten, die es verstanden, aus wirren Konstruktionsplänen wahre Kunstwerke zu zaubern oder auch die x-te Lockbock und das hundertste Kabel zusammenzulöten. Ihnen möchte ich an dieser Stelle ausdrücklich für die gute Zusammenarbeit danken. Unseren "Institutsseelen" Annelise Miglo, Ilona Jaschke, Fien Latumahina, und Dietmar Haubrich ist es zu verdanken, daß alles immer so reibungslos funktioniert hat, was unsere Arbeit erheblich entlastet.

Für das kritische Korrekturlesen dieser Arbeit oder Teilen davon danke ich Wolfgang Alt, Dominik Schrader, Arno Rauschenbeutel, Victor Gomer, Igor Dotsenko, Vanessa Leung, Ruby de la Torre, Yevhen Miroshnychenko und Wenjamin Rosenfeld. At this point, I thank Vanessa Venturi, Carl Williams, Eite Tiesinga and Daniel Steck for valuble discussions. I am also very grateful to Prof. Luis Orozco and his group for accommodating me in Stony Brook for six months.

Schießlich danke ich meinen Eltern für ihre Unterstützung in jeder Situation, was mein Studium und insbesondere diese Arbeit letztlich erst ermöglicht hat.